FEASIBILITY STUDIES FOR THE DETECTION OF EXOTIC PARTICLES USING ICAL AT INO

By

Nitali Dash

PHYS01200804028

Nuclear physics Division

Bhabha Atomic Research Centre, Mumbai.

A thesis submitted to the
Board of Studies in Physical Sciences

In partial fulfillment of the requirements

For the Degree of

DOCTOR OF PHILOSOPHY

of

HOMI BHABHA NATIONAL INSTITUTE

July 2015

Homi Bhabha National Institute

Recommendations of the Viva Voce Board

As members of the Viva Voce Board, we recommend that the dissertation prepared by **Nitali Dash** entitled **"Feasibility studies for the detection of exotic particles using ICAL at INO"** may be accepted as fulfilling the dissertation requirement for the Degree of Doctor of Philosophy.

---------- **Date :**
Chairman : Prof. A.K. Mohanty

---------- **Date :**
Guide,Convener : Prof. V.M. Datar

---------- **Date :**
Member : Prof. M.S. Bhatia

---------- **Date :**
Member : Prof. P. Shukla

---------- **Date :**
Member : Prof. N.K. Mondal

---------- **Date :**
External Examiner :

Final approval and acceptance of this dissertation is contingent upon the candidate's submission of the final copies of the dissertation to HBNI.

I hereby certify that I have read this dissertation prepared under my direction and recommend that it may be accepted as fulfilling the dissertation requirement.

---------- **Date :**
Guide : Prof. V.M. Datar

STATEMENT BY AUTHOR

This dissertation has been submitted in partial fulfillment of requirements for an advanced degree at Homi Bhabha National Institute (HBNI) and is deposited in the library to be made available to borrowers under rules of the HBNI.

Brief quotations from this dissertation are allowable without special permission, provided that accurate acknowledgement of source is made. Requests for permission for extended quotation from or reproduction of this manuscript in whole or in part may be granted by the Competent Authority of HBNI when in his or her judgment the proposed use of the material is in the interests of scholarship. In all other instances, however, permission must be obtained from the author.

Nitali Dash

DECLARATION

I, hereby declare that the investigation presented in the thesis has been carried out by me. The work is original and the work has not been submitted earlier as a whole or in part for a degree/diploma at this or any other Institution or University.

Nitali Dash

To
my parents,
my teachers
and
my sister & brother

ACKNOWLEDGEMENTS

I would like to thank people who have contributed fully and partially for making my life more complete.

First of all, I would like to cordially thank my supervisor Prof. Vivek M Datar, for teaching, guidance, and encouragement. He always encouraged me to do some different and unique work, which made the thesis complete. He is the most pertinent person in my research career from whom I have learned physics. The journey was quite lengthy, but it was a joyful and tireless journey. I am really grateful to him for making me appreciate and like research. I want to thank Prof. Gobinda Majumder who also supervised my work and helped me a lot in my studies.

I would like to thank my doctoral committee members: Prof. Naba K. Mondal, Prof. Ajit K. Mohanty, Prof. Prashant Shukla and Prof. M.S. Bhatia for their valuable comments and suggestions for completion of the thesis work. I would like to express my heartfelt gratitude to Prof. M.V.N. Murthy and Prof. G. Rajasekaran from IMSC, Chennai, for giving me an opportunity to work on their proposed explanation of Kolar events which became a part of my thesis work and for their quick response and useful suggestions on the work carried out by me.

My special thanks to Prof. Vandana S. Nanal, Prof. Sreerup Raychaudhuri, Prof. Amol S. Dighe, Prof. D. Indumathi, Dr. B. Satyanarayana, Dr. Prafulla K. Behera, Dr. R.G. Thomas and Dr. L.M. Pant for their guidance and encouragement during the Ph. D. period.

I will always be obliged to my M.Sc. (Utkal University) teachers Prof. Lambodar P. Singh and Prof. Pushpa Khare who motivated me and encouraged me to walk in this path. It was a great pleasure to start this research career with them.

I would also like to express my greetings to few of my colleagues and friends: Dr. Prakash C. Rout, Ravindra R. Shinde, Asmita, Dr. Sudhanwa Patra, Ali, Varchaswi, Lakshmi, Daljit, Kanishka and Neha Dokania for their help, support and encouragement during this period.

Last, but not the least, my deepest gratitude to my mother and father for their love, support and blessings throughout my life. My heartiest thanks to my sister for her understanding, support and love. She will always be ideal and unique for me and I would like to emulate her. Cheers to my brother for being a friend.

LIST OF PUBLICATIONS:

1. *Sensitivity for detection of decay of dark matter particle using ICAL at INO,
N. Dash, V.M. Datar and G. Majumder,
Accepted for publication in Pramana - journal of physics (19 March 2015); arXiv:1410.5182 (2014).

2. *Sensitivity of the INO-ICAL detector to magnetic monopoles,
N. Dash, V.M. Datar and G. Majumder,
Astropart. Phys. **70**, 33 (2015).

3. *A Study on the time resolution of Glass RPC,
N. Dash, V.M. Datar and G. Majumder,
arXiv:1410.5532 (2014).

*This thesis work is based on these papers

Contents

List of Figures

List of Tables

SYNOPSIS

The standard model (SM) is a well established model in Particle Physics. It incorporates the fundamental building blocks of matter such as quarks and leptons, carriers of the fundamental interactions and the Higgs boson (*which gives mass to the all elementary particles except neutrinos*). Although it has been spectacularly successful, there are some phenomena which are not explained yet, for example the unification of the strong and electro-weak interactions, neutrino mass, dark matter, dark energy, matter-antimatter asymmetry, existence of magnetic monopole and gravitational interaction. These belong to the physics beyond the SM.

The Grand Unified Theories (GUTs), which unify the three interactions except gravity, are an important milestone in the search for physics beyond the SM. In these theories all three forces have the same strength at a very high energy ($\sim 10^{15}$ GeV), which is out of reach of foreseeable accelerators. But a characteristic of GUTs is the interaction between leptons and quarks, which eventually results in the decay of the proton and bound neutron. In another context it also explained the existence of the primordial magnetic monopole [1, 2], which may catalyse proton decay. In GUT the mass of a monopole depends on the mass of the carrier of the unified interaction and the unified coupling constant. But till now there is no experimental evidence of magnetic monopole.

In the SM, neutrinos are *massless*. However experiments measuring atmospheric neutrinos show that neutrino oscillate. The oscillations occur because of the mixing of neutrino mass and flavour eigenstates. A neutrino could change its flavour state to another as it propagates in space. The first evidence of oscillation was observed by Super Kamiokande [3] in 1998. There are still some issues which are yet to be resolved, viz. absolute neutrinos masses, mass ordering (*mass hierar-*

chy), whether or not it is its own anti-particle (*Majorana or Dirac*), Charge-Parity violation, precise knowledge of mixing angles and amplitudes, and the possible existence of fourth or higher generation neutrinos. These will be addressed by the ongoing or next generation of experiments.

Some of these issues can be addressed through the search of neutrino oscillation in disappearance mode by the upcoming atmospheric neutrino ($\nu_\mu, \bar{\nu}_\mu$) based experiment i.e. Iron Calorimeter (ICAL) at India-based Neutrino Observatory (INO). The proposed underground laboratory is to be built at Pottipuram in Bodi West hills of Theni District of Tamil Nadu, in India, at longitude 77^0 $16'$ $22''$ E and latitude 9^0 $57'$ $47''$ N. The observatory will be under a rock cover of $\sim$1 km all around, which provides an overburden of about approximately 3.8 km water equivalent in order to reduce the cosmic ray muons flux millionfold to about 3×10^3 (m^2 sr y)$^{-1}$.

The ICAL [4] detector is rectangular in shape and segmented into three modules with overall dimensions of the order of 48 m $\times$ 16 m $\times$ 15 m. Each module consists of 151 layers of horizontally placed low carbon steel as an absorber with an average magnetic field of 1.3 T. The dimensions of each module are $\sim$16 m $\times$ 16 m $\times$ 15 m with a mass of $\sim$ 17 kton per module. Each layer is subdivided into 8 "roads" column wise consisting of 4 iron plates, each of dimensions 2 m $\times$ 4 m $\times$ 0.056 m. The stack of iron absorbers are interleaved with a 4 cm air gap housing 2 m $\times$ 2 m Resistive Plate Chambers (RPCs) as active detectors. The RPC has a pick-up panel based read out system placed orthogonally on either side of the RPC in order to give the X, Y co-ordinate information of an interaction in the detector.

The ν'_μs either interact through the charged current (CC) or neutral current (NC) interaction with nucleons in the ICAL detector. The detection of $\nu_\mu(\bar{\nu}_\mu)$ in the ICAL is obtained by detecting the $\mu^-(\mu^+)$ resulting from the CC interaction

of neutrino with the iron. As ICAL is a magnetized calorimeter, it will be able to identify the charge of the muon. The momentum and direction of the incoming neutrino can then be obtained by combining the momenta of the final state lepton and hadrons. The ICAL will be able to address the issue of neutrino mass hierarchy [5] because of the matter effect which affects ν_μ and $\bar{\nu}_\mu$ differently. In addition to this it is also capable of measuring the neutrino oscillation parameter θ_{23} [6], sterile neutrino mixing, and spontaneous neutrino decay. The ICAL detector in conjunction with accelerator based experiments could addressed the CP-violation [7] in neutrino sector.

While atmospheric neutrinos are the main focus of study at ICAL, such a large magnetised detector can also be put to other uses. Two such studies have been carried out and are the subject of the thesis. The first pertains to the sensitivity of ICAL to the much sought after primordial magnetic monopoles and the other to heavy dark matter particle decays.

It is widely accepted that dark matter constitutes $\sim$24% of the known matter-energy in the present Universe. The best evidence for dark matter (DM) comes about from the kinematical study of the galaxies using rotation curves [8]. The properties of DM are not known except for their gravitational effect. The dark matter particles that make up DM could possibly be unstable. If they are unstable their life time could be of the order of or longer than the age of the Universe. Although the energy density of the dark matter particles in the Universe is reasonably well known from experiments, the composition of such particles is not known. Various astrophysical evidences claimed that, they are relatively slowly moving. As the dark matter particles are present everywhere, they could be detected by detectors such as ICAL at INO, if they are sufficiently massive and decay in an

appropriate window of life time.

Apart from the detection capability and the physics studies of the exotic particles like *magnetic monopole* and *dark matter particle* using the ICAL detector at INO, the thesis also covers the studies of the optimization of RPC detector parameters in order to improve the measurements in the neutrino sector.

Sensitivity for detection of decay of dark matter particle using ICAL at INO

It has been recently speculated that the observed "Kolar events" [9, 10] recorded at a depth of 2.3 km in the underground laboratory at Kolar Gold Fields (KGF) in India, may be due to the decay of unstable dark matter particles (DMPs) [11] whose masses are in the range of several GeV. These anomalous events have evaded any conventional interpretation until now. It is believed that DMPs are present everywhere, so the stability of DMP can be probed by future neutrino detectors, like the ICAL at INO assuming the above re-interpretation. The sensitivity to dark matter decays may be enhanced by further placing sensitive detector elements on the walls and ceiling of the large cavern housing ICAL. In the thesis, we report [12] results of simulation studies targeting the decay of dark matter particles specifically into $\mu^+\mu^-$. For the purposes of simulation we assume that this channel saturates the decay width with the DMP mass ranging from $1 - 50$ GeV/c^2. The aim is not only to investigate the conjecture but, also more generally, to determine the lower limits on the lifetime of DMP in this range of mass.

Sensitivity of the INO-ICAL detector to magnetic monopoles

In the thesis, we have presented the sensitivity of ICAL alone and augmented with

large scintillator detectors for a particle carrying magnetic charge (g=68.5e) in the mass range from $10^7 - 10^{17}$ GeV with β $(= v/c)$ ranging from $10^{-3} - 0.7$ for ICAL at INO [13]. A tracking detector like ICAL, can discriminate such type of massive and slowly moving particles from high energy muons by the time of flight method. The upper limit on the flux of magnetic monopoles is $\sim 1.6 \times 10^{-16}$ $(\mathrm{cm}^2\ \mathrm{sr}\ \mathrm{s})^{-1}$ for 500 kton-y of ICAL detector operation. A similar study has also been carried out for the ICAL engineering module located at the surface. Due to the rock cover of approximately 1.3 km, ICAL at INO will not be able to detect or put limits on a possible flux for magnetic monopole of a lower mass and, some portion of this mass window can be addressed by the ICAL engineering module.

A Study of relative time resolution of glass RPC

The muons produced in CC interactions of neutrinos are tracked by the RPC detectors. In the avalanche mode the RPC signal rise time is $\sim$1 ns. While the muon track is derived from the X and Y hit information of the RPCs and its layer number (Z), the direction is obtained by using the time information from the detector. Such a capability can be examined by analysing the timing information from 1 m $\times$ 1 m glass RPCs, with 3 cm wide X- and Y- pick-up strips, in a 12 layer RPC stack that measures cosmic muon events by the TIFR group. The study is carried out for the pixel-wise time response [14] of these RPCs in order to see the uniformity of the relative time distribution over a RPC detector area of 1 m^2 and the variation of time resolution with distance travelled by the signal along the length ($\sim$1 m) of the pick-up strip of the RPC.

Study of correlated noise using TIFR prototype data

The hadrons generated in both CC and NC interactions will produce a certain number of hits in the RPCs in the ICAL type detector. Their energy and direction can be estimated from the hit patterns in the detector. If the patterns are noise free, then the extracted information is relevant to the incident particle. Noise does not seriously affect the muon sector due to the clean penetrating track in ICAL. The objective of the analysis is to identify the noise pattern in the TIFR detector stack in the presence of muon tracks. Our inference for the data is that the correlated noise is due to the present electronics and trigger logic.

Simulation studies with varying strip width in the RPCs in ICAL

As mentioned above, the magnetized iron tracking calorimeter will be able to discriminate between ν_μ and $\bar{\nu}_\mu$ by measuring the muon charge in CC interaction. The measurement of the hadronic energy and the momentum of the muons will allow a reasonably good reconstruction of the neutrino energy and as well as direction of neutrino. A study has been carried out to see the influence of strip width on the physics studies for ICAL through its effect on momentum resolution, angle resolution, reconstruction efficiency, charge identification efficiency and shift in the mean of reconstructed energy of the muon and neutrinos. The study has been carried out for single muons and pions considering strip width dimensions of 1.6 cm, 2 cm, 2.8 cm and 4 cm using GEANT4.

The thesis is organized as follows: Chapter 1 gives a brief outline of the Standard Model and physics beyond the Standard Model. The ICAL detector along with its physics motivation, the RPC detector stack at TIFR and the planned engineering ICAL module are described in Chapter 2.

Chapter 3, begins with historical overview and properties of the dark matter.

The different detection methods to detect DMPs, constituting DM, are described. Assuming finite lifetime of DMPs, the detection method using ICAL at INO followed by detecting them through their decay products. The motivation for detection of dark matter particles by this method has been described. It also covers the "Kolar events" observed at KGF, their interpretation, reinterpretation, and the feasibility study for the detection of such events using ICAL detector at INO.

Chapter 4 focuses on the sensitivity of the ICAL detector at INO and the proposed prototype detector overground for the detection of sub-relativistic GUT magnetic monopoles. After a brief introduction including earlier searches the interaction of the heavy MM with matter is described. The sensitivity of ICAL, along with the augmented plastic scintillator walls, to magnetic monopoles is quantified through simulation studies.

Chapters 5 and 6 are based on the analysis of TIFR prototype data using cosmic ray muons. Chapter 5 describes results of a study of the time resolution of glass RPC detectors used in the prototype stack. Chapter 6 presents the expected noise hits in addition to muon hits using the same data set. Chapter 7 describes the GEANT4 based simulation studies and the effect of varying the strip width in the readout panel of the Resistive Plate Chamber using a Monte-Carlo simulation of single muon and pion events. Chapter 8 presents the summary of the thesis.

Bibliography

[1] G. 't Hooft, Nucl. Phys. **B79**, (1974) 276.

[2] A.M. Polyakov, JETP Lett. **20**, (1974) 194.

[3] Y. Fukuda et al., Phys. Rev. Lett. **81**, (1998) 1562.

[4] M.S. Athar et al., "Physics Potential of the ICAL detector at the India-based Neutrino Observatory (INO)", arXiv:1505.07380 (2015).

[5] A. Ghosh et al., JHEP **1304**, (2013) 009.

[6] T. Thakore et al., JHEP **1305**, (2013) 058.

[7] M. Ghosh et al., Nucl. Phys. **B884**, (2014) 274.

[8] V.C. Rubin et al., Astrophys. J. **159**, (1970) 379.

[9] M.R. Krishnaswamy et al., Pramana **5**, (1975) 59.

[10] M.R. Krishnaswamy et al., Proc. XXIII Int. Conf. on High Energy Physics, Berkeley (ed. S. Loken, World Scientific, 1986).

[11] M.V.N. Murthy et al., Pramana **82**, (2014) 609.

[12] N. Dash et al., accepted for publication in Pramana - journal of physics (19 March 2015); arXiv:1410.5182 (2014).

[13] N. Dash et al., Astropart. Phys. **70**, (2015) 33.

[14] N. Dash et al., arXiv:1410.5532 (2014).

1 Introduction

The Standard Model of particle physics has been very successful in explaining a very large number of phenomena and observations. In spite of this there is a growing body of data that can not be understood within its ambit. In this chapter some of the lacunae of the Standard Model that point to physics beyond the Standard Model are discussed as also a few experiments that point in that direction. This chapter also mentions possible future directions in the area of high energy experimental physics in India and discusses the motivation of the proposed experiments.

1.1 Standard Model

All the matter in the Universe is composed of spin-1/2 (fermion) particles such as *quarks* and *leptons*. The dynamics of all these sub-atomic particles are characterized by the four fundamental interactions : *strong*, *electromagnetic*, *weak* and *gravitational* interactions. All these interactions are characterised by strength parameters and a particular set of conservation principles. In Quantum Mechanics, inter particle interactions are mediated by exchange of *quanta*. These quanta are spin-1 (boson) particles like *gluons*, *photon* (γ), $W^{\pm}$ *boson* and Z^0 *boson*. However the range of the force is inversely proportional to the mass of the quantum that is exchanged. So accordingly the weak forces are of *finite* range due to the finite mass of the mediator, whereas electromagnetic and gravitational forces are of *infinite* range due to the massless photon and graviton. Gravity is the dominant force at large length scales, because of its infinite range and being attractive, whereas

the electromagnetic force is both attractive and repulsive in nature. While the gravitational interaction is the dominant one for celestial bodies like planets, stars etc., its strength of interaction between sub-atomic particles is very small in comparison to the other three forces. Table (1.1) represents the characteristics of the fundamental forces.

Force	**Strength**	**Range**	**Quantum**
Strong	$\sim$1	1 fm[1]	gluons
Electromagnetic	$\sim 10^{-2}$	∞	γ
Weak	$\sim 10^{-7}$	10^{-3} fm	$W^{\pm}$, Z^0
Gravitation	$\sim 10^{-40}$	∞	graviton (?)

Table 1.1: The characteristics of four fundamental forces.

The coupling constants of the first three interactions vary with energy. At energies above 100 GeV, the electromagnetic and weak interactions unify to give the *electroweak* interaction with the coupling constants of these two interactions related to each other through the weak mixing angle (θ_W). The general expression is given by Eq. (1.1,1.2,1.3), where α_1 ($\frac{{g_1}^2}{4\pi} \equiv \frac{e^2}{4\pi}$, e is the charge of the electron) is the electromagnetic coupling strength and α_2 ($\frac{{g_2}^2}{4\pi}$) is the weak interaction coupling strength. The predictions of the electroweak theory, due to Glashow, Weinberg and Salam [1, 2], especially those pertaining to the neutral current in heavy atoms and neutrino interactions, have been verified experimentally [3].

$$\alpha_i = \frac{{g_i}^2}{4\pi} \qquad (i = 1, 2, 3). \tag{1.1}$$

$$g_1 \equiv e = g_2 \; sin \; \theta_W. \tag{1.2}$$

$$sin^2 \; \theta_W = \frac{{g_1}^2}{{g_1}^2 + {g_2}^2} \tag{1.3}$$

One of the problems with this theory is that the carrier of the electromagnetic interaction is massless, whereas the weak interaction carriers are massive. So in order to do unification the existence of *Higgs* particle was proposed by Peter Higgs [4], Francois Englert and R. Brout [5]. Recently the Higgs boson has been observed

[1]Hadron-hadron interactions, between colour neutral objects, have a finite range because that is governed by the exchange of the pion. However the gluon is massless and so the q-q interaction has a strong Coulombic part $\sim 1/r$, and a part which grows with r.

by the CMS [6] and ATLAS [7] experiments at CERN's Large Hadron Collider. It gives mass to the W and Z bosons and all the leptons except neutrinos. All these sub-atomic particles, their interactions, mediators and Higgs boson constitute the Standard Model (SM) [8] of particle physics. It must be said, that while the SM is very successful, explaining microscopic phenomena in the sub-atomic world up to length scales of $\sim 10^{-18}$ cm, it is after all a model and has its limitations. Figure (1.1) gives a schematic picture of the SM. Mathematically all these interactions

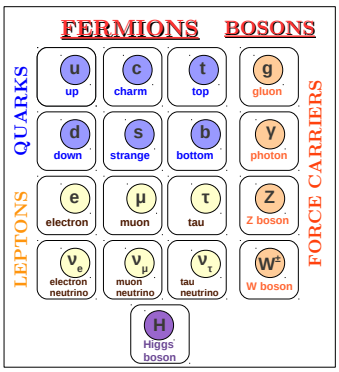

Figure 1.1: The Standard Model of elementary particles.

are described by gauge groups. These are SU(3), SU(2) and U(1) for strong, weak and electromagnetic interactions respectively.

It may also be mentioned that the unification of the electroweak and strong interactions could occur at a much higher energy and the relevant theories go beyond the SM.

1.2 Physics beyond the SM

The SM is a very successful model of particle physics as it is compatible with experimentally observed data and is believed to be free from mathematical inconsistencies. Nevertheless there are few questions which are not answered by SM. The most relevant questions in the present context are,

- *Unification of strong interaction and electroweak interaction.*
- *Experimental evidence of mass of neutrino, in spite of being massless in the SM.*

- *The theoretical formulation of quantisation of electric charge, which has been confirmed by the experiments.*
- *Observation of non-luminous matter in the Universe.*

Various theories have been put forth which aim to overcome the deficiencies of the Standard Model. Some of these theories are discussed below.

The transfer of neutrino flavours among themselves, is an indication of *mass of neutrino*. This phenomenon is called *neutrino oscillation*. It is a quantum mechanical phenomenon, where a neutrino of a specific flavour changes to another flavour as it propagates in space.

1.2.1 Grand Unified Theories

In Grand Unified Theories (GUTs) first three interactions are expected to have the same value at energies $\sim 10^{15}$ GeV or above. At this energy scale and beyond, it may be possible to describe the interactions among the elementary particles by a single gauge theory with a unique coupling constant. In gauge theory, the unification of three groups form a group 'G' with a single coupling constant 'α' ($g^2/4\pi$), where SU(3), SU(2) and U(1) are subgroup of G. SU(5), SO(10), SU(16) are some of the examples of the unified group G. The direct product of symmetric groups forms SU(5), Eq.(1.4). In addition SU(5) is the subset of SO(10) group.

$$G \supset SU(3) \otimes SU(2) \otimes U(1) \tag{1.4}$$

The new symmetry group introduces new gauge bosons. Apart from twelve gauge bosons (γ, Z^0, $W^{\pm}$, eight gluons) introduced by the SM, the SU(5) model introduces twelve more gauge bosons, which carry both baryon and lepton quantum numbers. These are X and Y bosons with a mass around 10^{15} GeV and participate in the interconversion between quarks and leptons. This interaction results in the decay of nucleon (proton and bound neutron). In another context, it also explained the *quantisation of electric charge* by introducing the existence of *magnetic monopole*.

1.2.2 Supersymmetry

Supersymmetry [8] is a space-time symmetry in particle physics that relates fermions with bosons and vice versa. This symmetry introduces the existence of super partner of fermions as bosons and bosons as fermions. The proposed super partners have the same mass as the partner but a different intrinsic angular momentum (spin).

The attractive features of supersymmetric theories are:

- It provides a framework for the unification of first three interactions and gravity at the Planck energy scale, $M_{\mathrm{P}} \approx 10^{19}$ GeV, where the gravitational interactions become comparable in magnitude to the gauge interactions.
- The *hierarchy problem* of the SM. For example, there is a large discrepancy between the strength of weak force and gravitational force. The weak force is 10^{33} times stronger than the gravitational. This disagreement could be explained with the supersymmetry.
- The unification of strong, weak and electromagnetic interactions at the Planck scale is possible by using new physics beyond the SM. It modifies the running gauge couplings above the electroweak scale.
- The *existence of dark matter* is explained in supersymmetry, by introducing a stable Weakly Interacting Massive Particle (WIMP). Its mass and interaction rate are governed by new physics and is consistent with the observed density of dark matter.

The Minimal Supersymmetric Standard Model (MSSM) [8] is the first realistic supersymmetric version of the SM. It was proposed to solve the hierarchy problem and predicts super partners with masses between 100 GeV and 1 TeV. Figure 1.2 shows the variation of coupling strengths as a function of energy ($\mathrm{Q} = \mathrm{E}/\mathrm{M_Z}$, $\mathrm{M_Z}$ is the Z boson mass and E is the energy in GeV) in SM and supersymmetric extension of the SM [9].

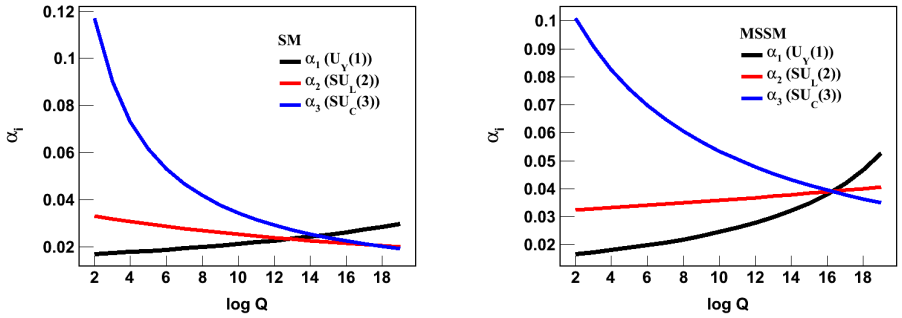

(a) (b)

Figure 1.2: Unification of strong, weak and electromagnetic interactions from SM (a) and from MSSM (b) [9].

1.3 Exotic particles

A brief description of the properties of the rarely interacting particles like *neutrino*, *dark matter* and *magnetic monopole* is given below.

1.3.1 Neutrino

The continuous energy spectrum of emitted e^- in a nuclear transition such as β-decay could be understood by introducing a neutral, spin-1/2 particle called a *neutrino*. It was first postulated theoretically by Wolfgang Pauli in 1930. It was given its named by Fermi [10]. Twenty four years after its postulation, it was experimentally discovered by Cowan and Reines [11] in 1956 using water as an anti-neutrino target with the reaction in Eq. 1.5. $CdCl_2$ is dissolved in it to greatly enhance the efficiency for detecting the slowed down product neutron. The water was surrounded by liquid scintillators.

$$\bar{\nu}_e + p \rightarrow e^+ + n. \tag{1.5}$$

In spite of the fact that neutrinos and anti-neutrinos do not possess electric charge, they behave like particles and anti-particles. When they interact with matter through the Charged Current interaction they produce leptons of opposite charge in the final state [12]. Neutrinos, being uncharged leptons, do not interact

via the strong and electromagnetic interactions. They only interact weakly and gravitationally. The neutrinos are left handed where as anti-neutrinos are right handed [13]. Just as there are three kinds of charged leptons (e, μ, τ) in SM, there exist corresponding flavours of neutrinos $(\nu_e, \nu_\mu, \nu_\tau)$ as confirmed from the decay width of Z^0 boson [14].

Neutrinos are produced copiously in the core of the Sun through nuclear fusion which is the source of solar energy. They are of electron type (ν_e) with energies up to ∼15 MeV. They were first detected by Davis [15] in a radiochemical experiment. These are also produced in cosmic ray interactions with the Earth′s atmosphere and are known as "atmospheric neutrinos". Atmospheric neutrinos are of the muon (ν_μ) and electron (ν_e) type with a number ratio of ∼2:1. These neutrinos were first detected experimentally at Kolar Gold Fields (KGF) [16] in India, in 1965 and almost simultaneously by Reines and his group in South Africa [17]. Various astrophysical objects like stars, galaxies, supernova also produce neutrinos through the nuclear processes. The Kamioka detector [18] in Japan has observed neutrinos (ν_e) from the supernova explosion SN1987A. Similarly the Earth′s core also produces neutrinos (ν_e and $\bar{\nu}_e$) from natural radioactivity and was first detected by the KamLAND detector [19] in Japan in 2005. All the naturally produced neutrinos are ν_e and ν_μ and their anti-particles. The above mentioned sources are the natural sources of neutrinos. They can also be produced artificially in accelerators and in reactors. So that their type, energy and flux are under control depending on the capability of the sources.

Neutrino oscillation is a quantum mechanical phenomenon predicted by Bruno Pontecorvo whereby a neutrino created with a specific lepton flavour (electron, muon or tau) can later be measured to have a different flavour. The probability of measuring a particular flavour for a neutrino varies periodically as it propagates. Neutrino oscillation is of theoretical and experimental interest since observation of the phenomenon implies that the neutrino has a non-zero mass, which is not part of the original Standard Model of particle physics.

The mass of neutrino can be determined directly from the processes like beta decay (ν_e mass), pion decay (ν_μ mass) and tau decay (ν_τ mass). Whether it has an anti-particle (Dirac) or it is its own anti-particle (Majorana) can also be found out from neutrino less double beta ($0\nu\beta\beta$) decay.

Neutrino mass ordering, precise measurement of neutrino oscillation parameters

and whether a 4^{th} or 5^{th} generation of neutrino exist are the other important problems that will be determined by the experiments.

1.3.2 Dark Matter

The Universe not only consists of matter but also of non-luminous matter, the so called *dark matter*. It does not interact through the electromagnetic force. This means it neither absorbs, nor emits electromagnetic radiation to make it directly detectable. These most elusive and non-emanating particles are not explained by the SM. In fact, its presence has been arrived at from various experimental observations such as the variation of rotational speed of spiral galaxies with distance and the motion of individual galaxies in clusters through its gravitational effect. Its other properties are not well known. It is assumed that it is composed of hypothetical particles like WIMPs and axions. They are expected to stable particles, on the scale of the lifetime of the Universe. The axions are weakly interacting bosons and are possible candidates for dark matter. A more detailed discussion about dark matter follows in Chapter 3.

1.3.3 Magnetic Monopole

Unlike electric charge, the existence of magnetic charge i.e. either north pole or south pole has not been observed till now. Theoretically it was introduced by P.A.M. Dirac in 1931, in order to explain the quantisation of electric charge. The magnetic monopole is a hypothetical elementary particle in particle physics that is an isolated magnet with only one magnetic pole. The details of the theoretical explanations and methods of detection are described in Chapter 4.

From many years ago, experiments at underground laboratories searched for such rare particles. The low cosmic ray background in an underground laboratory increases the sensitivity for the detection of magnetic monopoles. Various experiments have looked for magnetic monopoles. However there is still scope to reduce the upper bounds on the flux of these particles at an underground laboratory such as the India-based Neutrino Observatory (INO) [20] being set up in Pottipuram, Tamil Nadu in India.

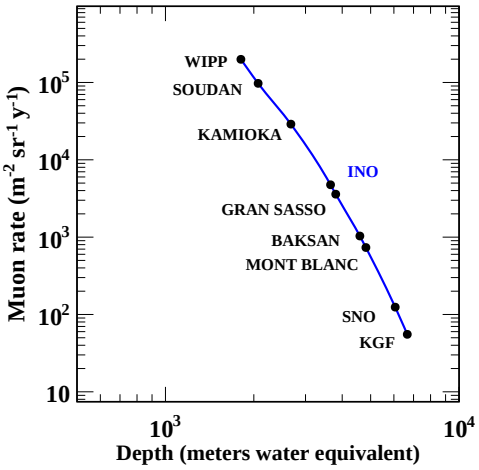

Figure 1.3: Flux of cosmic ray muons at various depths.

1.4 India-based Neutrino Observatory

Some of the issues related to neutrinos can be addressed through a more precise measurement of the neutrino oscillation parameters [21] by studying the zenith angle dependence of atmospheric muon neutrino at the Iron CALorimeter (ICAL) [22], address the neutrino mass hierarchy [23] and the search for neutrino-less double beta decay ($0\nu\beta\beta$) in ^{124}Sn using a cryogenic based bolometer detector [24, 25] at the upcoming India-based Neutrino Observatory. In addition to this the underground facility will also be able to search for dark matter [26] and magnetic monopoles [27]. The thesis is mainly focused on the potential of the ICAL detector for detecting the "invisible" particles making up dark matter and particle with "magnetic charge".

The proposed underground laboratory is to be built at Pottipuram in Bodi West hills of Theni District of Tamil Nadu, in India, at longitude 77^0 $16'$ $22''$ E and latitude 9^0 $57'$ $47''$ N. The observatory will be under an all round rock cover of $\sim$1 km, which provides an overburden of about approximately 3.8 km water equivalent in order to reduce the cosmic ray muons flux millionfold to about 3×10^3 m^{-2} sr^{-1} y^{-1}. Figure 1.3 [28] shows the expected vertical cosmic ray muons flux at various underground laboratories along with flux at INO site. At the present site the muon flux is $\sim$150 times higher than at KGF, which was under operation

from 1965 to 1992, in India. Sudbury Neutrino Observatory (SNO) is currently the deepest multi-purpose laboratory in the world.

The largest detector at INO is the ICAL detector with a mass of 51 kton. It is modular in structure with overall dimensions of ∼48 m × 16 m × 15 m. It is segmented into three modules and each module consists of 151 layers of horizontally placed low carbon steel, also providing target nuclei for neutrino interactions, with an average magnetic field of 1.3 T. The optimised dimensions of the iron plates are 2 m × 4 m × 0.056 m and interleaved by an air gap of 4 cm in order to accommodate 2 m × 2 m Resistive Plate Chambers (RPCs) as active detectors. The RPC has a pick-up panel based read out system and placed orthogonally on either side of the RPC in order to give the X, Y co-ordinate information of an interaction point in the detector. The Z co-ordinate is obtained from the layer number. A similar 34 kton detector MONOLITH, with somewhat thicker steel plates, was conceived by the Italian group but was not built [29].

The atmospheric neutrinos come in two flavours i.e. muon type (ν_μ) and electron type (ν_e) and corresponding anti-particles ($\bar{\nu}_\mu, \bar{\nu}_e$). They are produced from the decay of charged pions ($\pi^\pm$) and muons ($\mu^\pm$) (see Eq. (1.6)), which originate from the interactions of primary cosmic rays with the nitrogen and oxygen nuclei in the upper atmosphere. So these are considered as decay products of secondary cosmic rays. The existence of two flavours of neutrinos with a broad energy spectrum starting from 100 MeV and falling as $E^{-2.7}$ and from all directions makes it very useful in exploring the physics of neutrinos using neutrino oscillations.

$$\pi^\pm \rightarrow \mu^\pm + \nu_\mu(\bar{\nu}_\mu),$$

$$\mu^\pm \rightarrow e^\pm + \bar{\nu}_\mu(\nu_\mu) + \nu_e(\bar{\nu}_e). \tag{1.6}$$

The flux of cosmic ray particles on the Earth surface varies with longitude and latitude of the location due to the effect of galactic/extra-galactic field at the respective places and their energies. Since neutrinos, which are charge neutral, are produced through the decay of secondary particles, their flux is also affected and has a latitude-longitude dependence. The flux of atmospheric neutrinos at the INO site is plotted in Fig. 1.4 [30]. The plotted distribution is the sum of two neutrino flavours and their anti-particles and averaged over all direction as a function of

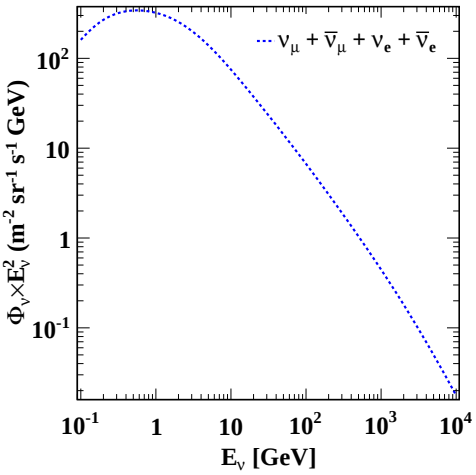

Figure 1.4: Flux of atmospheric neutrino at the INO site [30].

energy.

There is a large up-down asymmetry in the flux of neutrinos at low energy as shown in Fig. 1.5. The plot in the left panel shows the zenith angle dependence of the flux for 1 GeV neutrinos and the right panel for 10 GeV neutrinos. The cosine of zenith angle (θ) with negative value corresponds to up-coming neutrinos, zero value for horizontally incident events to the detector and positive for downward going events (see Fig. 1.6). The up-down asymmetry decreases with increase in energy and almost disappears at 10 GeV. This asymmetry implies that the flux of up-coming neutrino is higher than the down-going one and is due to the Earth magnetic field at low energy. For energies above a few GeV, the flux peaks near the horizon (cos θ=0) due to the availability of larger length of atmosphere.

1.5 Physics possibilities of the ICAL detector

The useful range of energy of atmospheric neutrinos is from 0.1 GeV to a few TeV. So it covers a wide range of neutrino interaction with matter. Depending on the neutrino energy [31], the interaction process is mainly quasi-elastic (QE), resonance scattering (RS) or deep-inelastic scattering (DIS).

The neutrino interacts with matter only via the weak interaction. Depending on the type of mediator, i.e. Z^0 or $W^\pm$ the interaction is either of the Neutral

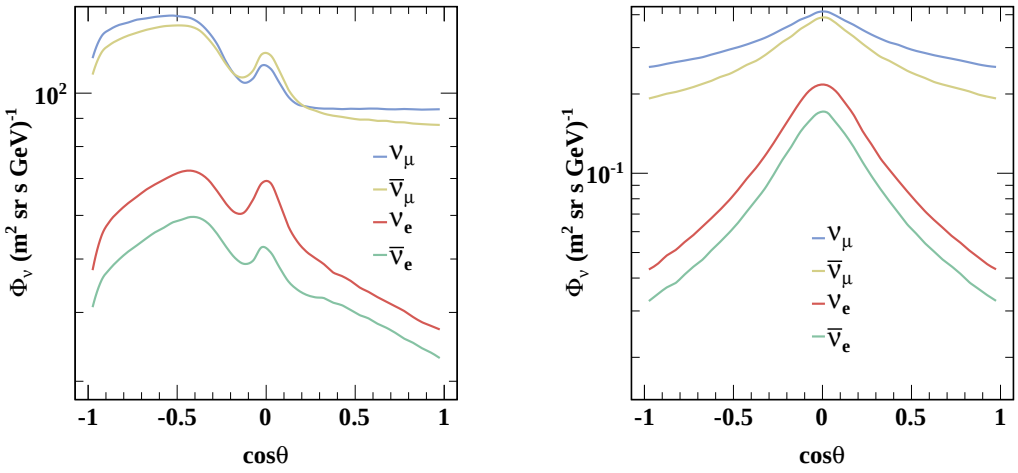

Figure 1.5: Flux of atmospheric neutrino at the INO site vs cos θ where θ is the zenith angle for neutrino energies of 1 GeV (left panel) and 10 GeV (right panel) [30].

Current (NC) or Charged Current (CC) type. A schematic view of these two type of interactions is given in Eq.(1.7). The difference is that, in NC type a $\nu_l(\bar{\nu}_l)$ produces corresponding neutrino(anti-neutrino) of same flavour but in CC interaction the outgoing particle will be the charged lepton ($l = e, \mu, \tau$) of the corresponding neutrino flavour. These two types of interactions take place in each of the three processes viz. QE, RS and DI, depending on the energy of the neutrino.

$$\nu_l(\bar{\nu}_l) + N \rightarrow l^-(l^+) + X \qquad \text{(CC)}$$

$$\nu_l(\bar{\nu}_l) + N \rightarrow \nu_l(\bar{\nu}_l) + X \qquad \text{(NC)}. \tag{1.7}$$

In the energy range from 100 MeV to ~ 3 GeV, the most prominent process of interaction is QE scattering. In this process a nucleon could be scattered elastically by neutrino. In the case of CC interaction, this is referred to as *quasi-elastic scattering* but in case of NC interaction it is *elastic scattering*. Above $2-3$ GeV neutrino energy and below 10 GeV, the RS is dominant. Hence the $\nu_l(\bar{\nu}_l)$ may excite the nucleon to a resonance which subsequently decays to one or more hadrons (pions, kaons etc.). This process is followed for both CC and NC scattering. At energies above 10 GeV, the process is mainly DIS. Here the energy of the $\nu_l(\bar{\nu}_l)$

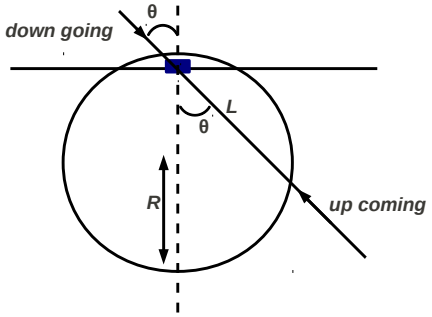

Figure 1.6: Direction of upcoming and down going event and the path length L associated with zenith angle θ. R is the radius of the Earth.

is sufficiently high to spatially resolve individual quarks in the nucleon. This is followed by the hadronization of the scattered quarks leading to the generation of a shower of hadrons in CC and NC. The only difference in CC and NC processes that distinguish them from each other is that, in CC the hadrons are accompanied by $l^-(l^+)$ and in NC by $\nu_l(\bar{\nu}_l)$. Even though all the processes are same for neutrino and anti-neutrino, the neutrino interaction cross-section is *two times larger* than that of the anti-neutrino. The suppression of the anti-neutrino interaction cross-section comes entirely from the *helicity* considerations.

The CC interaction, as opposed to the NC interaction, can be used to definitively identify whether the detected particle was a neutrino or an anti-neutrino. More specifically the tracking magnetised detector such as ICAL is most suitable for measuring muon neutrinos and anti-neutrinos. This is because the outgoing particle will be either a μ^- or μ^+ (corresponding to ν_μ and $\bar{\nu}_\mu$) which will give a clean track in ICAL. But due to the use of comparatively thicker (~ 5.6 cm) iron plates in ICAL both ν_e and $\bar{\nu}_e$ will give rise to an electromagnetic shower and/or a hadronic shower and will not be distinguishable from each other. *So broadly ICAL will be measuring ν_μ and $\bar{\nu}_\mu$ only.*

The ICAL is sensitive to the oscillation probabilities of the type $P_{\mu\mu}, P_{\bar{\mu}\bar{\mu}}, P_{e\mu}, P_{\bar{e}\bar{\mu}}$. However the former two are relevant for physics studies i.e. *survival probability* from the observation of *deficiency* in flux of $\nu_\mu(\bar{\nu}_\mu)$. Due to the broad range of neutrino energy and distance (L, see Fig. 1.6) travelled in matter before their detection in ICAL, it will be possible to measure the full oscillation leading to a precise

measurement of the absolute value of $\Delta m^2{}_{32}$ and θ_{23}. It will also be possible to determine the sign of $\Delta m^2{}_{32}$ i.e. identify the mass hierarchy by measuring ν_μ and $\bar{\nu}_\mu$ separately independent of any possible CP violation in the neutrino sector.

The existence of fourth generation neutrinos (ν_s, sterile neutrino) could also be addressed by ICAL. One of the ways of searching for such a mixing, for $\Delta m^2 \sim \mathrm{eV}^2$, is to search for deviation from the expected energy spectrum for down going neutrinos. A detailed discussion on neutrino oscillation is given in Ref.[22].

In addition to the issues mentioned above the detection of very high energy muons [32, 33], study on CPT violation [34] and non-standard neutrino interaction [35], interpretation on Kolar events and magnetic monopole in sub-relativistic region could also be addressed.

1.6 Preface of the Thesis

This thesis deals with the simulation studies related to the possible verification of two signatures of the new physics viz., the detection of dark matter particles through their decay and cosmic sub-relativistic magnetic monopoles.

The chapters are organised as follows, Chapter 2 introduces the Iron CALorimeter detector. Chapter 3 discusses the anomalous Kolar events detected by experiments at Kolar Gold Fields in India along with a brief introduction to KGF detectors. Following this the results of the Monte-Carlo simulations for the detection of dark matter particle decays in ICAL, as well as for ICAL with additional detectors on the cavern walls, are presented. Chapter 4 gives a short overview of Dirac′s proposal of the magnetic monopole and related theoretical developments and experimental searches. The present simulation study using ICAL to search for magnetic monopoles is described. The sensitivity of such a search is about 4 times better than that of experiments done hitherto. Chapters 5 and 6 present two kinds of analysis of data collected by the stack of twelve layers of RPC at TIFR. Chapter 7 presents results of a detailed simulation of the effect of different strip widths on reconstructed muon and hadron momenta. Finally, chapter 8 summarizes the results and gives a short outlook.

2

An overview of Iron CALorimeter

The Iron CALorimeter (ICAL) is a proposed massive (51 kton) magnetised tracking detector at the India-based Neutrino Observatory (INO) in India, mainly optimised for the detection of atmospheric muon neutrinos (ν'_μs). The magnetisation of the iron allows the identification of ν_μ and $\bar{\nu}_\mu$, separately, through the charged current interaction which leads to μ^- and μ^+, respectively. In spite of its large size the low event rate necessitates its placement beneath a rock cover of $\sim$1 km all around to reduce the cosmic muon background. In the following section some details of ICAL are presented.

2.1 Iron CALorimeter (ICAL)

A massive tracking calorimeter has been chosen in order to provide the necessary number of nucleons for neutrino interaction, as it interacts very weakly with matter with an interaction cross-section of $\sim 10^{-38}$ cm^2 (at 1 GeV energy). So the detection of such a tiny particle is possible using a detector consisting of a large mass in the smallest volume. Also the target material used in building the detector should be cheap and readily available. Finally since a magnetic field is required to distinguish between the oppositely charged muons produced in ν_μ and anti-ν_μ interactions the natural choice is soft iron or low carbon steel with good magnetic characteristics. Furthermore a high-density detector also allows the selection of a pure ν_μ CC event providing good μ/π separation.

The Iron Calorimeter detector, rectangular in shape and modular in structure, consists of three modules with mass $\sim$17 kton each. It is a "Sampling Calorimeter"

and consists of passive target like low carbon steel sandwiched with layers of active detector viz. Resistive Plate Chamber (RPC). The orientation of the detector is perpendicular to the direction of the cosmic ray particles. Such a detector configuration is easier to construct from a technical point of view and also helps in rejecting the background from downward going cosmic ray muons. Additional scintillator planes are proposed to be used in the cavern housing the ICAL for other physics studies like search for *dark matter particle* and *magnetic monopole*. It will also provide redundancy in this background rejection, and might eventually be used to increase the effective fiducial volume.

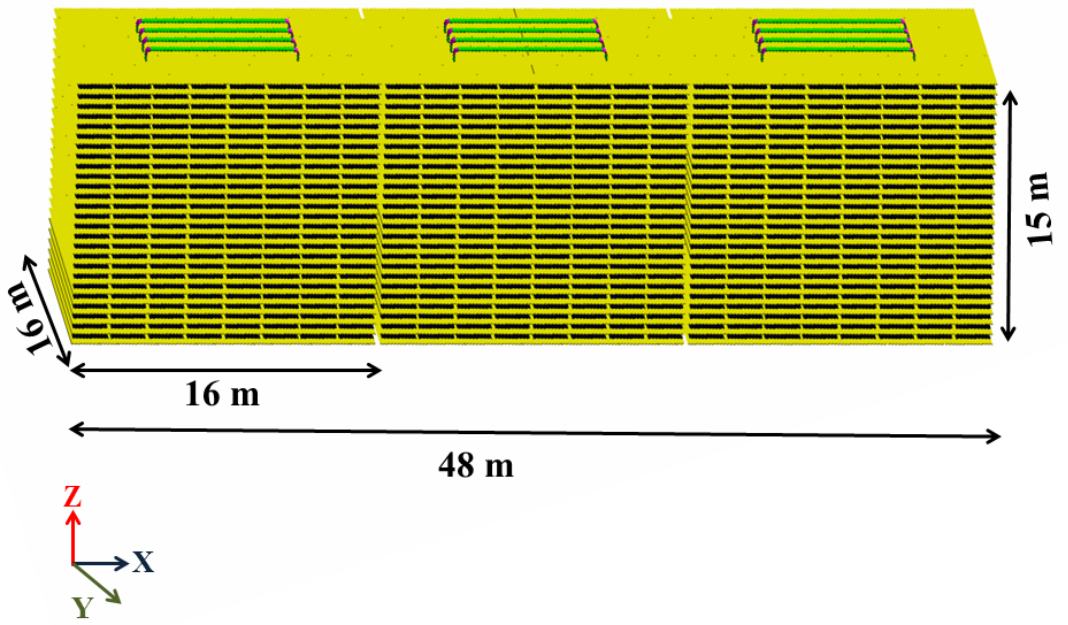

Figure 2.1: Schematic diagram of three ICAL modules.

The transverse dimensions of a single module of the proposed ICAL are ∼16 m × 16 m and consists of 151 layers of iron plates. Each layer is subdivided into 8 "roads" column wise consisting of 4 iron plates per road, each of dimensions 2 m × 4 m × 0.056 m and separated by an air gap of 2 mm. The optimized thickness and size of the iron plate for the ICAL has been estimated from desired field distribution, physics and the mechanical assembly point of view. Physics wise the use of a thicker iron plate leads to a larger bending of the track of muon resulting from CC ν_μ interaction inside the plate but also leads to more multiple scattering.

But the minimum separation between two plates in a layer has been decided by the magnetic field strength required for a reasonable budget of mains power. The two layers of iron plates are separated by a 40 mm air gap to accommodate RPCs between them. To maintain a gap of 40 mm suitable circular shaped spacers made of stainless steel are placed near the edges of the plate. The RPC detector of dimensions ∼2 m × 2 m × 0.03 m with a position resolution of ∼1 cm and time resolution of 1 ns is used. Such a detector configuration will also allow access of the active detector elements during maintenance to optimise the overall availability factor of the detector. The modular structure also allows the addition of more ICAL detector modules.

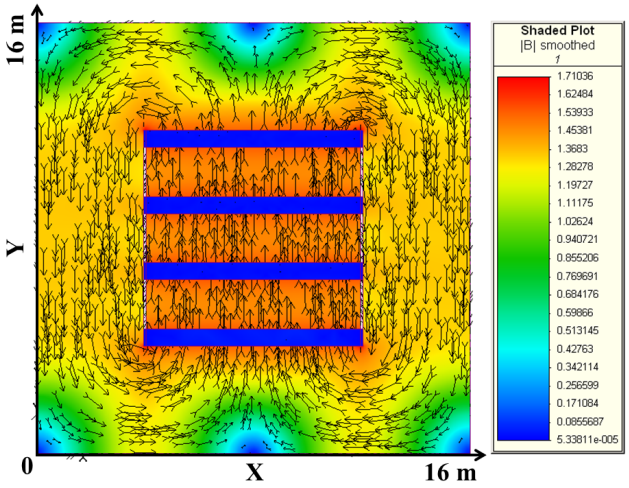

Figure 2.2: B-field over an iron layer having continuous slots containing four coils carrying 60 kA-turns.

For magnetisation a vertical slot (see Fig. 2.1) crossing the stack is made, through which the current carrying coils have to pass. This layout has been chosen in order to keep the magnetic field entirely inside an iron plate with minimum power consumption and to avoid stray field. The coils will be wound from a 30 mm × 30 mm hollow OFHC[2] conductor (18 mm bore hole for carrying low conductivity water). A 3D electromagnetic simulation has been carried to get a magnetic field strength of ∼1.3 T, using four coils through two continuous slots carrying current of 50 kA-turns [36]. These are the optimized dimensions for a single module of ICAL in order to achieve continuous and required field strength with

[2]Oxygen-free high thermal conductivity

a power consumption of 100 kW. The field distribution (direction and magnitude) on a layer of iron plate (16 m × 16 m) of a module for 60 kA-turns is shown in Fig. 2.2 [36]. The magnitude of the field is shown by different colours as marked on the right side of the plot.

Similarly two more identical modules are placed side by side with an air gap of 20 cm between them. A sketch of the three modules of ICAL is shown in Fig. 2.1. The overall specifications of the ICAL detector are summarized in Table 2.1.

Iron Calorimeter	
No. of modules	3
Size of a module	17 kton
Dimensions	16 m × 16 m × 15 m
Iron plate	
No. of iron layers	151
Plate dimensions	2 m × 4 m × 0.056 m
Material	Low carbon steel
Magnetic field	1.3 Tesla
Active detector element	
Resistive Plate Chamber	Glass, Avalanche mode
Dimensions	2 m × 2 m × 0.03 m
Position resolution	∼1 cm (X and Y plane)
Time resolution	1 ns

Table 2.1: Key physical parameters of Iron Calorimeter detector.

The response parameters for muons and pions of ICAL like energy resolution, direction resolution, position resolution have been found using GEANT4 [88] Monte-Carlo simulation. The response of the detector to these particles was estimated using the above detector geometry and associated parameters. The energy and direction resolutions are estimated separately for muons [37, 38], hadrons [39, 40] and muon-less (low energy ν_μ CC, ν_e CC and NC) [41, 42] events. However the position resolution (see Chapter 7) is decided using muons and hadrons.

2.2 Engineering module of ICAL

An engineering prototype module of ICAL of dimensions 8 m × 8 m × 2 m is planned to be built over ground at Madurai in next $2-3$ years. It has a mass

which is $\sim 1/30^{th}$ of that of a single ICAL module. This engineering module will be similar to the main ICAL module from all other points of view. Hence the various parameters of the detector are the same except for the scaling down of the size. The experience gained in assembling and operating the engineering module is expected to be very useful before taking on the assembly of the 17 kton modules.

2.3 RPC stack at TIFR

A stack consisting of 12 RPC detectors of dimensions (1 m $\times$ 1 m) installed at TIFR (see Fig. 2.3) has been working for more than 10 years. Each 1 m $\times$ 1 m RPC has 32 parallel pick-up strips on each side laid orthogonally. Two consecutive layers are at a distance of $\sim$16 cm. The detector efficiencies are above 95% [43] as measured using cosmic-ray muons. Apart from assessing the long term performance of RPCs, it has also been used to make measurements on the cosmic muon flux [43].

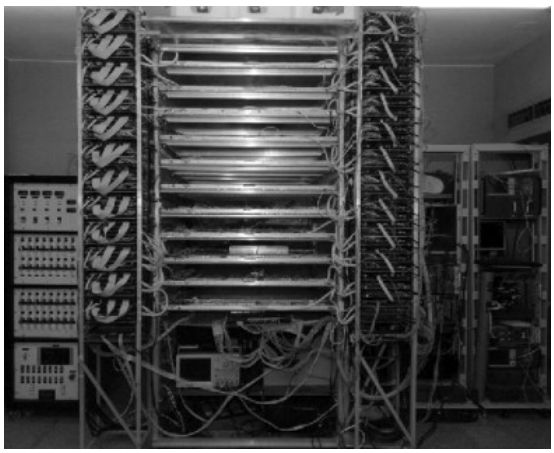

Figure 2.3: Twelve layer RPC stack at TIFR.

Resistive Plate Chamber

The RPC [44] for ICAL is a gaseous detector composed of two glass electrodes of 3 mm thickness, separated by suitable spacers of 2 mm height to accommodate the gas mixture of R134A (95.15%), Iso-Butane (4.51%) and SF_6 (0.34%) just above the atmospheric pressure. The float glass has a volume resistivity of $\sim 10^{12}\ \Omega \cdot$cm.

These are also coated with graphite having an area resistivity of $\sim 1 \frac{M\Omega}{\Box}$. This in conjunction with the high resistivity of the glass gives good position localisation of the location of the charged particle traversing the RPC.

Gas System

The mixing of gases in the proportion required for RPC operation in the avalanche mode is done in the gas system. The gas system used for the prototype is an open loop system [45] with 16 independent channels and designed for mixing up to four gases. So one can connect 16 RPCs at a time and can operate them independently. After the gas cylinder, the gases are passed through filters with molecular sieves of $3-5$ Å pores to scavenge them of impurities. The proportion of gases is controlled using Mass Flow Controllers (MFCs) leading to a manifold where the mixing takes place [46]. This mixture is routed to RPCs via flow resistors made up of 5 m long thin capillaries having inner diameter less than 1 mm. These flow resistors provide uniform pressure and avoid back pressure to adjacent non connected channels. At the input of each RPC line, a safety bubbler is provided to avoid any damage of RPC in case any blockage occurs in output line. The oil level of the safety bubbler is adjusted in such a way that if the pressure inside RPC increases by certain value it releases the pressure by bubbling gas through it. At the outlet of each RPC an isolation bubbler is in place, to isolate the system and ambient pressure, and avoid back flow. It is also an indicator of proper gas flow through the RPC. All channel outputs are connected to an output manifold and the outlet gas is released in the atmosphere. To create a small negative pressure at the output line an exhaust fan has been inserted.

As it is an open loop gas system the gas is discharged in to the atmosphere. Even though the gas is not harmful to the atmosphere (ozone friendly), it is good economics to reuse the gas as it is fairly expensive. A prototype version of a closed loop system (CLS) in which used gas can be re-circulated after its purification has been installed at TIFR. Presently it is under going tests with 10 numbers of 2 m $\times$ 2 m RPCs [47].

Data Acquisition

The information one needs from the stack are the event time, co-ordinates of the interaction zone, its relative time of interaction in the detector with respect to event trigger and the status of the detector.

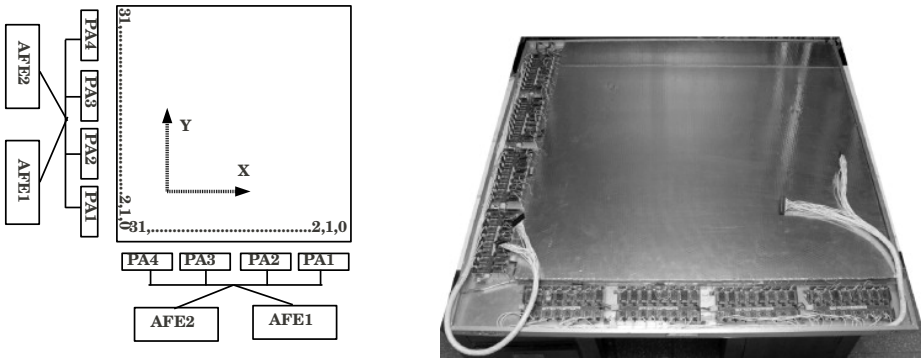

(a) (b)

Figure 2.4: (a) Schematic diagram of Resistive Plate Chamber with pre-amplifiers and AFEs. (b) The photo of 1 m × 1 m RPC with pre-amplifiers.

Due to the avalanche mode of operation of the detector the signal strength is of the order of few mV. The necessary amplification of the signal, from a pick-up strip, has been done using a 8 channel two stage cascading amplifier with a gain of ∼80. The amplified output is fed to a 16 channel analog discriminator cum analog front end (AFE) with a voltage threshold at - 20 mV (see Fig. 2.4). Then the AFE output is fed to digital front end board (DFE). Each individual strip signal is stretched to 720 ns as the trigger signal arriving at DFE is delayed due to the longer signal path. The pre-trigger signals from AFE are used to form level 1 signals which are further used for generation of an event trigger in a CAMAC based Data Acquisition (DAQ) system. To generate a triggered event, these level 1 ECL signals from different layers are fed to a coincidence module via an ECL to NIM converter module. Data in the DFE board is latched and the TDC data is also stored for every trigger. The scalar is used to monitor the strip count rate irrespective of the trigger signal. All required control signals for event and monitoring processes routed to DFEs via the Control and Data router (CDR) board are initiated by the Control Module. A schematic diagram of transfer of data from front end to back end is shown in Fig. 2.5. Event data is transferred serially to the Readout

board. The DAQ system has been optimised for the VME format and the details are presented in Ref.[48].

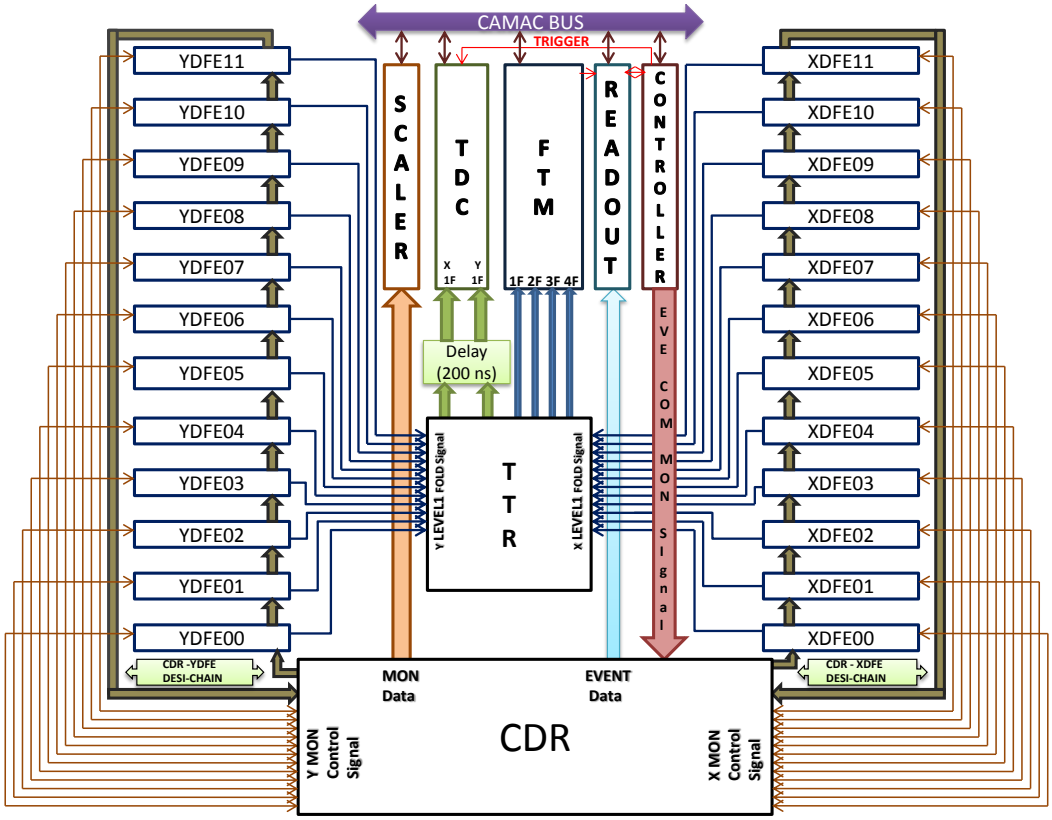

Figure 2.5: Schematic view of data acquisition system for prototype stack.

3

Detection of dark matter using ICAL at INO

The experimentally well established dark matter is still a mystery with regards to its constituents. Except its gravitational interaction with visible matter, very little is known about the constituents, spin, life time and interaction cross-section. We know that it is stable on the scale of a few billion years but its stability is an open question. In this chapter, we have presented the sensitivity of the ICAL detector for the detection of cold dark matter through its decay to muon channel and the motivation behind the proposed detection method.

3.1 Introduction

There is strong experimental evidence that Dark Matter (DM) constitutes about $80 - 90\%$ of all known matter in the Universe. The nature of DM is unknown. It could consist of one or more particles or bound states of a combination of these. The presence of DM has inferred from the gravitational effect on visible matter and radiation. Experiments such as PAMELA [49], AMS-02 [50], DAMA [51], CoGeNT [52] have given hints of DM from the observation of excess of antiparticles (e^+, anti-proton, anti-deuteron) either from annihilation or decay or a low energy excess with an annual modulation. Dark Matter particles, sometimes also referred to as WIMPs, with certain range of mass, spin and nuclear interaction cross-section are claimed to have been observed by experiments like CRESST [53], CDMS-II [54] through direct detection method by measuring the recoiling nuclei in a

DM/WIMP−nucleus scattering. Similarly the *anomalous Kolar events* [55, 56, 57] observed in two phases of the detector upgrades and operations at Kolar Gold Fields (KGF) in South-India during 1965−90, have been recently reinterpreted as the decay of cold DM [58]. The earlier suggestion of a new particle produced in high energy cosmic neutrino interactions with the rock was ruled out by accelerator based neutrino experiments [59, 60]. The newer suggestion, if proven correct, could open a whole field of study of DM particles.

If this idea is correct, it should be possible to search for such decays of DM particles with much greater sensitivity using the 51 kton ICAL detector in the much larger cavern at INO. The results of such a simulation study are reported in this chapter. Alternatively one can place lower bounds on the partial life time of DM for an experiment carried out in the underground ICAL cavern. The lower limit on DM life time has been estimated by assuming a 100% branching ratio for the dimuon decay of a DM particle in the mass range of 1 to 50 GeV/c^2. The addition of scintillator detectors on the cavern walls increases the sensitivity of the ICAL detector to DM particle decays. The larger sensitive volume at ICAL-INO, as compared to that in the KGF experiments, results in a larger number of decay events being detected.

Section 3.2 gives a brief summary of the observed anomalous events and their specific properties. In §3.3 and §3.4, we give historical overview of DM and its detection mechanism. The rest of the sections dwell on the detection method used to detect DM at INO, the detector configuration used for DM detection, Monte-Carlo based simulation study for sensitivity measurement, Frequentist approach for the estimation of the absolute life time of low mass DM and comparison of the results with other experiments.

3.2 The anomalous Kolar events

A special class of events were recorded in several detectors operated in KGF during 1965 − 90. Due to their special character these are named as "*Kolar events*". These were observed in two periods of the experiments at KGF in south India.

The first period corresponds to the detector for atmospheric neutrinos at a depth of 2.3 km during 1965 − 69. The detector consisted of three layers of neon

flash tubes with a separation of two layers of 1″ thick lead absorbers and outer walls of plastic scintillators. The detector was aligned vertically with an area of 2 m × 3 m. Such an orientation made it sensitive to horizontal tracks i.e. events coming at steep angle.

The second period corresponds to two phases of experiments looking for proton decay at a depth of 2.3 km and 2 km in the same mine. Here the detector covered an area of 2 m × 4 m with an absorber consisting of 40 cm thick iron plates which was magnetised to a B-field of 14.5 kilogauss and the active elements were same as the above. The details of the detector configurations are discussed in Ref.[61].

The characteristics of first five events reported in 1975 [55] are as follows:

1. The observed events consisted of two or more tracks with a large opening angle with at least one being a penetrating track such as that due to a muon.

2. All tracks of an event seemed to originate from a single vertex located either in air or from the low density material of the detector.

3. The fraction of such anomalous events out of total number of recorded events was about 25%.

4. The explanation in terms of the production of a long lived particle produced in neutrino-rock interactions was ruled out by accelerator experiments.

The events observed in the second phase had a penetrating track and an associated shower. The summary of the characteristics of observed events at KGF in 1986 [56] are given in Table 3.1.

Event Number	**Penetrating Track (GeV)**	**Shower (GeV)**	**Opening Angle (deg)**	**Vertex**
1	> 1.3	> 2.6	32	air
2	> 0.4	> 2.5	69	air/rock
3	> 1	≥ 5	41	inside detector

Table 3.1: Summary of Kolar events reported at KGF during 1986.

Various theoretical [62, 63, 64] and experimental [59, 60] attempts were made to understand the origin of these events. Finally considering the results from

the experiments carried at accelerator and using neutrino beams, and the several possible backgrounds at KGF like probability of interaction of cosmic ray muons at steep angle, inelastic neutrino interaction and chance rate from the stray firing of flash tubes or through radioactivity in the rock surrounding the detector assembly, these were interpreted as due to the decay of *new, massive* and *long-lived* particles.

Recently these have been re-interpreted [58] *due to the decay of cold dark matter particles, of mass around* $5-10$ GeV/c^2 *with a life time comparatively the life time of the Universe or longer than it.* This reinterpretation came from the observation of three DM events with mass of $\sim$8.2 GeV/c^2 through nuclear recoil in the CDMS-II [54] detector. So considering the isotropic decay of DM, it may be that KGF experiments had observed one of the decay products of the two resulting from back-to-back decay, leading to a DM particle mass estimate of $\sim$double the observed energy.

So in the following sections we present a brief introduction to the dark matter, its properties, detection methods and then the simulation work carried for the detection of Kolar events through dark matter decay using ICAL at INO.

3.3 Dark Matter

Unlike ordinary matter, dark matter is non-emanating and non-absorbing. The presence of dark matter has been inferred through the gravitational interaction. It is present every where in the Universe due to the dominant role of gravitation on scales from a tiny dwarf galaxy, to large spiral galaxies, to cluster of galaxies and to the largest scales yet observed. The Universe consists of approximately 4.9% ordinary matter, 26.8% dark matter and 68.3% dark energy. In spite of being invisible the dark matter is predominant over visible matter.

3.3.1 Evidence of dark matter

The presence of DM was first pointed out by F. Zwicky [65] in 1933, from the dynamics of galaxies in the Coma cluster. The observation was that, the measured rotational velocity of the galaxy is not sufficient to explain the estimated mass from the emitted light. Similarly S. Smith [66] in 1936 also concluded at the same conclusion as Zwicky, from the study of the Virgo cluster. So they had concluded

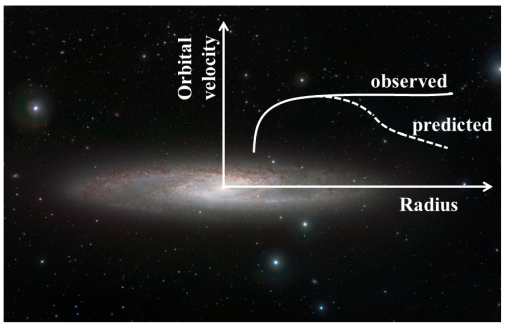

Figure 3.1: Rotational velocity distribution vs distance [81].

that their must be another component of matter in order to explain the whole things.

The clear experimental evidence of such non-emanating matter hypothesis was established by Vira Rubin [67] during $1960-70$ from the kinematical study of the galaxies using the rotational curves. In principle the mass of the Galaxy should be concentrated at the center as with the luminosity, which is concentrated at centre and then decreases as one moves out. Newtonian gravity, together with a matter distribution consistent with optical observations, predicts an initial rise in the velocity (v) of a star with respect to its radial distance from the center of the galaxy (r) and then a fall. The detailed variation of v with r depends on the particular mass density distribution. If M is the mass of the galaxy, R is the radius of the galaxy and G is the gravitational constant, then the dependence of v on r, for a uniform mass density distribution up to a sharp cut-off radius R is,

$$v = \begin{cases} r\sqrt{\frac{GM}{R^3}}, & r < R \\ \sqrt{\frac{GM}{r}}, & r \geqslant R \end{cases} \tag{3.1}$$

From Eq.(3.1), with in the body of the galaxy the orbital velocity increases linearly with the radius of the galaxy and it is in comparable with the experimental observation. But outside of the luminous mass distribution of the galaxy it falls with the square root of the radius and is in contradiction with experiments. Observations show a constant distribution with the distance as shown in Fig. 3.1.

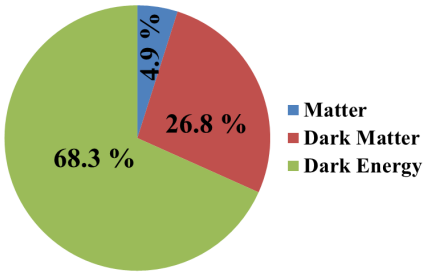

Figure 3.2: Distribution of matter in the Universe.

Dark matter existence has also been inferred from the observation of gravitational lensing. The concept is that light bends while passing through a strong gravitational field. So the image of an object behind a massive star or galaxy can get enlarged or distorted and an example of this is seen in images of the Bullet cluster [68], which is formed by the collision of two clusters of galaxies. In the collision the visible matter of in each of the clusters interacts whereas the dark matter does not. So the matter content is separated from each other, with the luminous matter lagging behind the invisible matter. Hence the central region of the Bullet cluster is almost made up of ordinary matter and the DM resides outside the central region. This non-luminous matter has been suggested from gravitational lensing.

Measurements of the cosmic microwave background (CMB) radiation allow an estimate of the mass and energy distribution in the Universe. The Wilkinson Microwave Anisotropy Probe (WMAP) mission played an important role in establishing the components of matter in the Universe [69]. The last result from Planck mission has established that the total mass energy of the Universe contains 4.9% ordinary matter, 26.8% dark matter and 68.3% dark energy (see Fig. 3.2). Dark matter seems to be essential in the evolution of the Universe.

These are the studies which show the presence of invisible matter in the Universe. A brief discussion of recent results on the searches of dark matter by various experimental groups is presented in §.3.4.

3.3.2 Properties of DM

Our present day understanding of the origin of the Universe is that it started with the Big Bang. Soon after Dark Matter was created. The Universe expanded and cooled with time. Stars were formed, evolved and died. The non-luminous or Dark Matter that we see today is of two kinds viz. "baryonic" and "non-baryonic".

Baryonic DM is like ordinary matter, i.e. the constituents are protons and neutrons. For e.g. it include cold clouds of gas, black holes, brown dwarfs, burned out white dwarfs and rogue planets. The primary candidate for baryonic DM is generally called a MAssive Compact Halo Object, or MACHO. As the name suggests these objects are massive and compact, and exist in the halo of galaxy.

On the other hand *non-baryonic* DM does not consist of quarks or gluons. The constituents of such DM particles must be *electrically neutral*, otherwise they would have interacted with the normal matter in the Universe and become "visible". But such DM must necessarily interact gravitationally. It could also interact through some kind of "weak" interaction with normal matter.

The non-baryonic DM is further classified into *hot* and *cold* DM. The classification in terms of hot and cold DM are related to some of their kinematical attributes, i.e. whether it is light and relativistic or heavy and non-relativistic speed. *Neutrinos* may constitute the hot DM, whereas hypothetical particles like *axion*, *Weakly Interacting Massive Particle* (WIMP) could be the fundamental components of the cold DM.

The particle axion was proposed in connection with CP violation in strong interactions [70] and could be a component of DM. Supersymmetric theories (SUSY) allow Weakly Interacting Massive Particle (WIMP) that could account for the observed DM in the Universe. WIMPs could include particles like neutralino introduced by SUSY as a partner of neutrino in SUSY, higgsino, squarks, photino, cosmion etc. Similarly in higher dimension a hypothetical particle introduced by the Kaluza Klien model may also constitute the basis of dark matter [71]. This model also predicts the mass and coupling strength of these particles. So depending on the properties of DM it also suggests the detection method and the mode of interaction with the constituents of ordinary matter.

However all properties predicted by various models have to be probed experimentally. This includes the stability of DM particles which has been addressed by

various observations, both terrestrial and astrophysical.

3.4 General discussion of DM detection

In general the detection of particle is based on the transfer of energy to the electrons in a detecting medium. The charged particles can be detected directly, whereas neutral particles are in general detected by exploiting an interaction or sequence of interactions which produces a charged particle. Similarly the DM can be detected by electron recoil, or by nuclear recoil, or by detecting SM particles from annihilations and decays.

The general overview of various principles which can be used for dark matter detection are discussed below. The discussion follows on the basis of detection of fundamental properties of the dark matter like mass, spin, interaction cross-section and life time. So mainly the detection is classified into two categories, such as *direct* and *indirect* method.

3.4.1 Direct detection method for DM

Direct methods are those in which the detection takes place from the direct interaction of the particles in the terrestrial apparatus. In what follows the principles for the detection of light and heavy DM particles are described.

Light mass DM:
Light mass DM such as the axion can be detected either by detecting photons from the interaction of axion with magnetic field or by ionisation in the form of transferring energy to e^{-}s in matter via the interacting electron or nucleus which recoils. The idea of conversion to photon by interaction of axion with magnetic field was introduced by P. Sikivie [72, 73]. The concept is that a boson coupling with any charged particles gives two photons as in Fig. 3.3. Similarly axions can interact with the magnetic field (see Fig. 3.3) and the energy of produced photon is same as the mass of the axions, if axions are slowly moving.

In case of ionisation by light boson due to the much smaller value of coupling constant with matter, the event rates are negligible. The cross-section (σ) is given

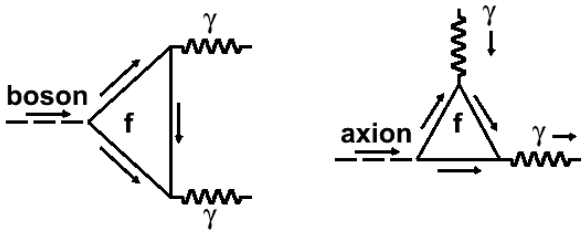

Figure 3.3: Feynman diagram for axion detection [77].

by,

$$\sigma = (3 \times 10^{-24}\ cm^2) g^2 (m_a/\beta_a m_e)^2, \tag{3.2}$$

where m_e is the mass of electron, g is the coupling constant, m_a and β_a are the initial mass and velocity of the axion. So the former method is most suitable for the detection of low mass DM.

The Axion Dark Matter eXperiment (ADMX) [74] is currently the only experiment, which is searching for cold dark matter axions in the local galactic dark matter halo through the Sikivie effect as discussed above. It uses high quality resonant microwave cavity within a large superconducting magnet in order to scan the range of axion mass in the range of $1.90 - 3.54$ μeV [75, 76].

Heavy mass DM:
For heavy mass DM, the search involves either ionisation or the detection of nuclear recoils resulting from DMs colliding with the atoms in a detector. WIMPs can couple to nuclei via *spin* interaction or a *spin-independent* interaction. In the spin interaction, the WIMP couples to the spin of the nucleus, and in the scalar interaction, the WIMP couples to the nucleus with or without an isospin dependence.

For a heavy weakly interacting particle the spin independent cross-section vary with the square of the mass of the target nuclei [78]. So high mass nuclei are used for the search. The recoil energy of the nuclei in-terms of the dark matter mass ($m_{\rm D}$) and atomic mass of the nuclei (A),

$$E_{\rm R} = E_{\rm D} \frac{4 A m_{\rm D}}{(A + m_{\rm D})^2} \frac{(1 - cos\ \theta)}{2}, \tag{3.3}$$

where $E_{\rm D} (= \frac{1}{2} m_{\rm D} \beta^2)$ is the incident energy of the DM, and θ is the scattering

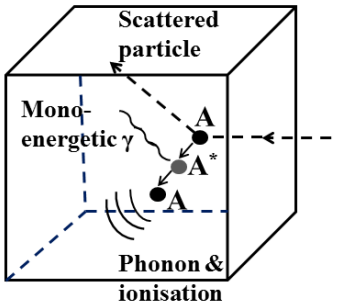

Figure 3.4: Principle of dark matter detection [77].

angle. The maximum recoil energy is given by,

$$E_{\mathrm{R}} \mid_{max} = E_{\mathrm{D}} \frac{2Am_{\mathrm{D}}}{(A + m_{\mathrm{D}})^2}. \tag{3.4}$$

So a measurable energy transfer occurs for not too heavy mass DM. The maximum recoil energy is ∼keV for a DM mass of few GeV. Hence the measurement of recoil energy is possible either from the production of phonons (detected directly or thermal pulses), or by ionisation or through scintillation (see Fig. 3.4).

These detectors consist of rare gases such as argon or xenon in the liquid or gas phase, scintillators (NaI(Tl), CaF_2 etc.), semiconductors (HPGe or Si) or cryogenic bolometers. The CRESST experiment with an exposure of 730 kg.days has reported the observation of 67 events obtained from the WIMP scattering [79]. But these signals have been classified as different sets of background. Recently the CDMS experiment with silicon detectors has been claimed the observation of three events with mass of ∼8.2 GeV with an exposure of 140 kg.days [54].

Direct detection also involve the measurement of the *annual modulation* due to the Earth orbit around the Sun. Dark Matter is expected to form a halo in and around the visible constituents of our Galaxy. As the Solar System is in motion around the centre of the Galaxy, then the Earth should experience a fluctuations in the magnitude and direction of a DM signal. This anisotropy comes due to

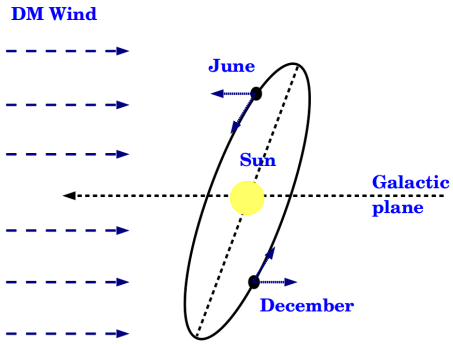

Figure 3.5: Annual modulation [81].

the direction of the Earth motion along the DM wind motion or in the reverse direction as shown in Fig. 3.5. This has been observed by the DAMA/NaI and DAMA/LIBRA experiments. The detectors have observed 7 annual cycles [80] by combining 1.04 ton-year of exposure by DAMA/LIBRA phase and 1.33 ton-year of DAMA/NaI phase.

3.4.2 Indirect detection method for DM

Indirect methods are those which involve the detection of the secondary particles at the Earth surface, from the interaction of the DM with the celestial bodies like the Earth, Sun and galaxies or due to the decay and mutual interaction.

Heavy mass DM

WIMPs are present whole over the Universe. They may interact with the celestial bodies like Earth, Sun and galaxy. Hence could be slow down, captured and trapped in celestial objects. They can annihilate or decay, and will be able to detect through their decay products. The products include neutrinos, gamma rays, positrons, anti-protons, and anti-nuclei.

So experiments looking for neutrino oscillation like SK, IceCube and AMANDA have also studied the neutrinos from dark matter annihilation or decay. Space based experiments like AMS, PAMELA and Large Array Telescope (LAT) also have looked for excess of anti-particles from DM decay. The AMS and PAMELA experiments have measured the e^+ flux at energies of tens to hundreds GeV [82, 83],

the best measurements on anti-proton flux at energies range of 60 MeV to 180 GeV comes from the PAMELA satellite [84] and the FERMI/LAT experiment has put stringent bounds on the flux of high energy photons [85].

Light mass DM

Another way one looks for light DM in particle colliders is to identify events with missing energy and momentum. If a DM particle is produced in a collision it will escape detection carrying with it energy and momentum. Such DM particles could be candidates for supersymmetric particles and are being searched for in experiments at the Large Hadron Collider (LHC) [86].

A summary of the above mentioned detection methods are presented in Fig. 3.6.

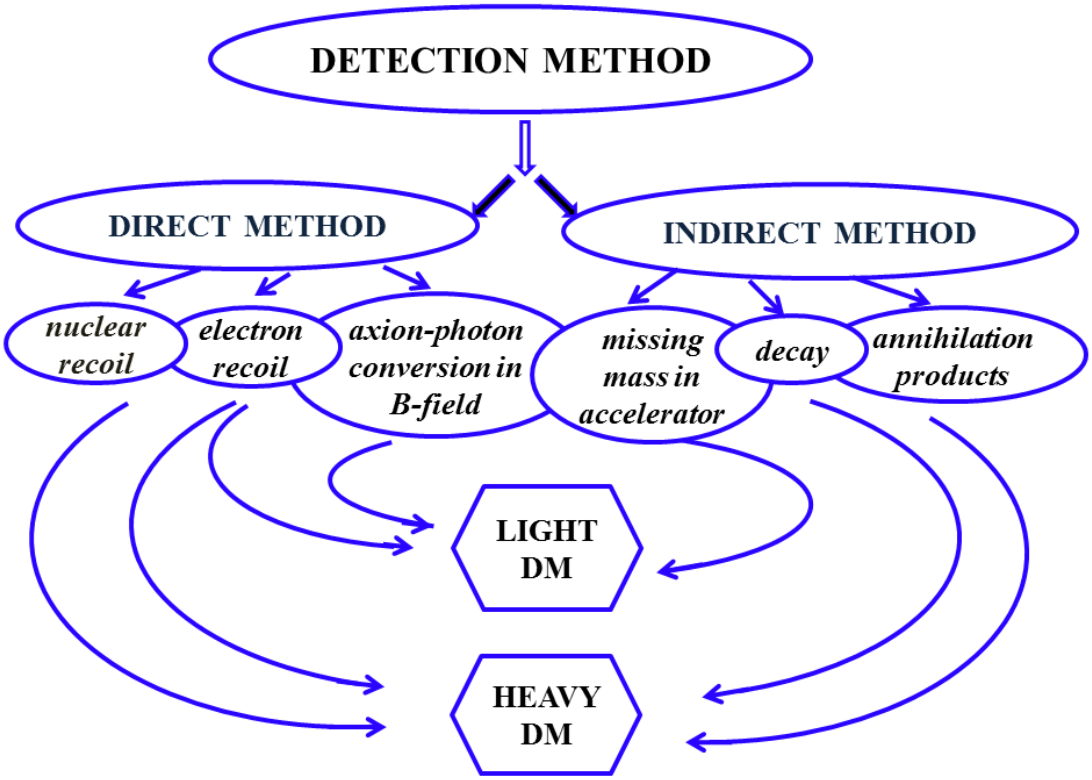

Figure 3.6: Summary of the experimental principles for the dark matter detection.

3.5 Detection method for DM at INO

Even though the numbers of DM particles in the region of galactic halo, centre of the Sun and centre of the Earth is huge due to large volume, the detection of leptons from decay or annihilation of low mass DM at the underground laboratory at the Earth is difficult. The low energy charged leptons will get deflected by the Galactic and the Earth magnetic field during their travel from Galactic system to the Earth surface. In addition they will not reach ICAL because of the 1 km rock cover, unless the DM particle mass is $>\sim$TeV. On the other hand the dineutrino channel has been used to place very stringent upper bounds on DM particle number densities as a function of its mass [8]. However a terrestrial search for the decay of DM particles to charged dileptons in large underground caverns may still be valuable. So in order to detect such decay products at the underground laboratory, it can be assumed that these are present at the laboratory as they are present everywhere in the Universe and are invisible due to their non-luminous nature.

So here we introduce an indirect method to look for the DM. The deep underground neutrino detector should be able to detect the possible decay of DM provided the mass of DM is in a suitable range and its decay products are easily detectable. To detect DM using the ICAL detector at INO, we assumed that it decays to Standard Model particles.

The DM can then have decay channels such as $q\bar{q}$, W^+W^-, Z^0Z^0, $b\bar{b}$, $\tau^+\tau^-$, $\mu^+\mu^-$ and e^+e^-. Out of all these decay channels, for convenience, in this simulation, it is assumed that DM is a neutral scalar particle ($\Phi_{\rm DM}$) that decays to lepton pairs only. This mode of decay is also most suitable for detecting DM using the ICAL detector. The ICAL is a sampling calorimeter and is especially suitable for tracking muons which may arise from DM decays to $\mu^+\mu^-$ pairs. Therefore, in general, we look for the decay modes of the type,

$$\Phi_{\rm DM} \rightarrow \mu^+ + \mu^-. \tag{3.5}$$

The *dimuon decay channel* has been used to simulate the decay of DM particles in the ICAL cavern for a given mass and life time of DM. Given the 56 mm thick iron plates that will be used, ICAL is not very suitable for detecting the other branches such as e^+e^- and $\tau^+\tau^-$. As ICAL will use 56 mm thick iron plate the

electron will give rise to an electromagnetic shower in the detector whereas the heaviest lepton such as τ decays to hadrons (64%), muons (17%), electrons (17%) and corresponding neutrinos (ν_e, ν_μ, ν_τ) with in a distance of $c\tau \sim 90$ μm. So ultimately tau will get detected through the decay products very close to the decay vertex. To investigate the detection capability of the ICAL detector to these decay channels we have estimated the detection efficiency using the hit information in the detector and this is discussed in §.3.8. But these two channels are not used in the physics studies.

The leptonic decay channel of DM has been studied by the satellite based experiments like AMS, PAMELA and LAT. They have measured the ratio of positrons and electrons as a function of their energy. Various sources of positron production lead to a certain predicted dependence of the positron to electron ratio as a function of electron/positron energy. Above about 10 GeV the measured ratio in these experiments exceeds expectations [87] that do not include DM decay or annihilation. The DM decay in the ICAL cavern that we will search for at INO has, of course, equal numbers of particles and anti-particles.

Due to the non-relativistic nature (speed $\simeq 220$ km s^{-1}) of DM, it is assumed that they are almost at rest, its decay will be isotropic. For a given mass of the DM the energies of the daughter particles are obtained by two body kinematics. Assuming the mass of the decay particle and anti-particle to be m, the mass of the DM to be M the momentum of each of the daughter particles, p_1 and p_2, is given by

$$|\overrightarrow{p_1}| = |\overrightarrow{p_2}| = \sqrt{\frac{M^2}{4} - m^2}. \tag{3.6}$$

If no such decay is observed, one should be able to put lower bounds on the possible partial life time after sufficiently long exposure. As pointed out in Ref.[58], a large cavern located deep underground, as in the case of neutrino detectors, should be able to identify the DM decay if the life time is around the age of the Universe. Either way this provides a novel way of putting limits on the DM decay or its detection which has not been compared before.

In order to detect such events at INO, a detector configuration with ICAL as the central detector and some additional detectors around it is proposed. This is described in the next section.

3.6 A detector for DM particle decay

The ICAL detector is well suited for the detection of ν_μ type neutrinos. As it is a tracking calorimeter, it could nicely track μ's from neutrino interaction. If a DM particle decays into two back-to-back muons inside the ICAL detector, the tracks can be characterized and reconstructed. On the other hand the ICAL cavern has a volume which is about an order of magnitude higher. If one can place additional detectors in the cavern to detect the DM particle decay products the sensitivity towards DM particle decay is expected to increase substantially.

The Dark Matter is believed to be present everywhere. The biggest cavern at INO is the ICAL cavern having dimensions of ∼132 m × 26 m × 32 m and a cavern volume ∼ 10^{11} cm^3. As mentioned in Ref.[58], this large volume will lead to an increase in the number of detected DM decay events which is around ∼1/year based on the analysis of Kolar events. For the event rate estimation, the DM decay lifetime of 10^{10} years and a number density ∼ 0.1/cm^3 (local DM density ∼0.39 GeV/cm^3, if DM mass = 3.9 GeV) of DM is assumed. So to detect all the decay products in the form of visible particles, we have placed detectors on the 4 walls of the ICAL cavern in the simulation.

The proposed ICAL detector will occupy 48 m × 16 m × 15 m of the ICAL cavern. In principle, the remaining space of the ICAL cavern can be used for additional DM detector installations. One such simple configuration is proposed in this work.

As the ICAL detector will be located towards one end of the cavern, four scintillator detectors (SDs) are mounted close to the walls of the cavern. A schematic diagram of the detector is as shown in Fig. 3.7. As shown in the figure surfaces 1, 2, 3 and 4 depict the scintillator detectors. Two of these detectors are placed along the length of the cavern with dimension of 132 m × 0.04 m × 32 m. The third one is placed in YZ plane with area of cross-section 26 m × 32 m, having thickness of 4 cm. The fourth one is above the ICAL surface at a height of 17 m from the top surface of the ICAL. This can also be used as a muon veto for ICAL. In the simulation only one layer of detector is used for each surface. So no energy measurement is available from these detectors. On the other hand they provide the signals for identifying back-to-back leptonic decays of DM particles.

ICAL uses around 30,000 RPCs of dimensions 2 m × 2 m. If RPC with same

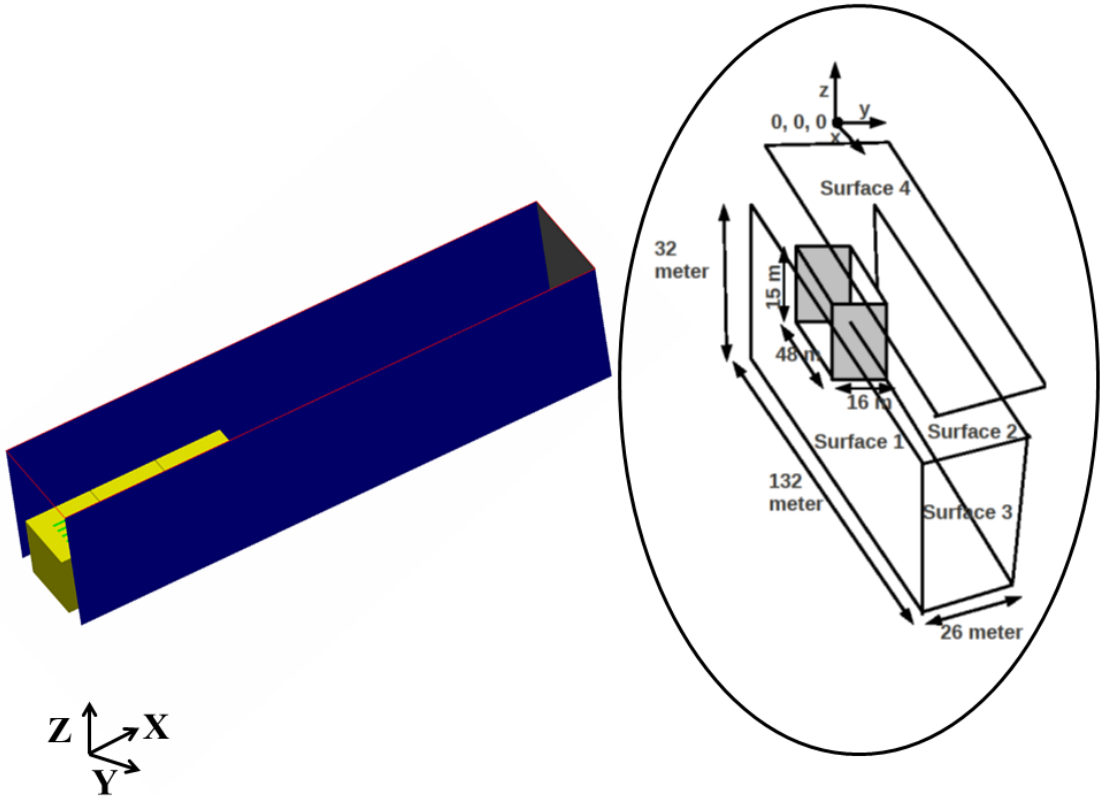

Figure 3.7: Top view of DM detector configuration used in GEANT4 simulation. Two scintillator detectors (blue, surface1 and 2) along the length of the ICAL detector, detector (gray, surface 3) in YZ plane and the top detector (border with red in colour, surface 4) has been made transparent in order to see the detector geometry.

dimension were to be used instead of scintillator detector, then around 3,000 of them would be needed for a single layer lining on each plane. This is 1/10 of those required for ICAL.

3.7 Simulation of decay of DM particle

On the basis of detection criteria for the decay of DM, the simulation is carried out in two regions separately. These two regions are specified by the air region i.e. the gap between the ICAL and the scintillator planes and another one is inside the ICAL detector.

In case of a DM decay to $\mu^+\mu^-$ channel, it can be identified unambiguously in the ICAL provided its energy is 0.5 GeV or more, since there are two muon tracks back to back, which can be easily distinguished from other events. But for the other two channels i.e. e and τ, some uncertainties arise.

The DM mass is taken as input to the simulation instead of the daughter particle energy. The mass of the DM, decaying into μ and e pairs, is varied from 1 GeV/c^2 to 50 GeV/c^2 in 1 GeV/c^2 steps. As the τ mass is 1.7 GeV/c^2, the DM mass is varied from 6 GeV/c^2 to 50 GeV/c^2 in this decay channel. In the simulation two daughter particles start from a single vertex in opposite directions and with momenta given in Eq.(3.6). To simulate the isotropic decay the zenith angle ($cos\ \theta$) is smeared from 0 to π and the azimuthal angle (ϕ) by 2π. The charge of one of the daughter particles in a decay event is chosen randomly and the other daughter particle has the opposite charge. A total of 5000 DM events are generated for each DM particle mass with each decay event having $\mu^+\mu^-$ in the final state.

3.7.1 Simulation of DM particle decay in air region

The High Energy Physics (HEP) simulation tool-kit GEANT4 [88], is used to do the simulation for DM decay in the air region. In the simulation, the defined detector geometry is the same as mentioned in §.3.5 in addition to the ICAL detector geometry. The B-field distribution for a single layer of iron plate as shown in Fig. 2.2 has been implemented in GEANT4. The events are generated in the air gap i.e. between the SDs and the ICAL detector. In a fraction of the simulated events the trajectories of the daughter particles are such that at least one of them enters the ICAL detector and its partner hits the SD. Thus it will be possible to measure the energy of at least one decay product.

In case the DM decays to a pair of muons, one of them will give rise to a clean track in the ICAL detector and the other one will have hits in the SD in the opposite direction. The background for such events will be the cosmic ray muon or a muon produced due to the interaction of neutrino with the rock and detection in the ICAL detector. But this can be eliminated by using the timing information from the detector.

The genuine events are selected by considering the reconstructed momentum

within $\pm 3\sigma$ of the incident momentum measured by the ICAL detector. The Kalman Filter [89] algorithm is used to reconstruct the momentum of the muon inside the ICAL. It is also possible to reconstruct the vertex position and direction cosine inside ICAL. The position of the other muon in the scintillator is obtained by extrapolating the hit position in it using the reconstructed vertex and direction cosine. If the extrapolated position and the simulated position match within a certain range then these events are used in the efficiency calculation. The uncertainty in the measurement of the extrapolated position is taken as 1 m individually for each position component. Decreasing this reduces the efficiency of detecting low mass DM decay. The reconstruction efficiency is as shown in Fig. 3.8a. With increase in mass the efficiency increases. At lower mass the efficiency is small due to large uncertainty in angular resolution during the extrapolation of the hit position on the SD.

The energy and direction of muon are reconstructed using Kalman Filter algorithm inside the ICAL and only momentum reconstructed muons are used in the calculation of efficiency. Since at least one muon has to enter ICAL and at low energies angular resolution is poor due to the multiple scattering, we get poorer reconstruction efficiency for the muon in ICAL and hence a poorer efficiency for DM decay.

At higher muon energies, up to about 25 GeV, the reconstruction efficiency is about 0.9 [37] leading to a reasonably high efficiency for DM decay for masses up to 50 GeV/c^2.

A single layer of the SD may not help to distinguish them from background. So to improve this situation at least 2 layers of detector should be in place. From the timing information it will be possible to identify and discriminate the decay products from background. At least 6-8 layers are needed for good range energy resolution in ICAL. In this case the efficiency will be obtained by separately reconstructing the direction for SD and ICAL and then by reconstructing the vertex. It will also result in enhancement in the efficiency.

When DM decays to a τ pair, either it will have a bunch of hits or a clean muon track depending on its decay products in the detector. In this case the events produced due to the interaction of the neutrino with the rock matter will be act as a background. So if the DM vertex is near the SD, then the background arises from neutrino induced events. A detailed discussion on the elimination of backgrounds

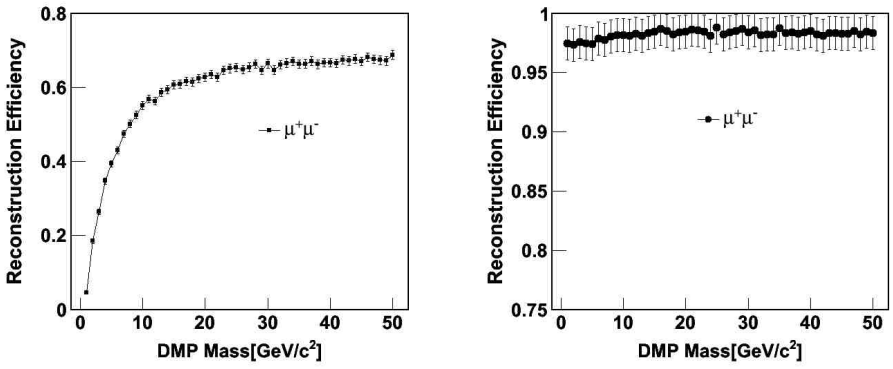

(a) (b)

Figure 3.8: (a) The reconstruction efficiency for DM decays to $\mu^+\mu^-$ in air region. (b) The reconstruction efficiency inside the ICAL for the DM decays to $\mu^+\mu^-$ pair.

for the detection of dark matter particle from its products are presented in §.3.9.

3.7.2 Simulation of DM particle decay in ICAL

In this case all the events are generated inside the ICAL detector within a fiducial volume of 40 m × 14 m × 12 m. Inside the ICAL it is possible to measure the energy of two muons and hence the invariant mass.

For DM decays to $\mu^+\mu^-$ the timing and trajectory information can be used to separate them from background due to cosmic ray muons and neutrinos. The Monte-Carlo technique is used to simulate DM decays, uniformly distributed within the fiducial volume of ICAL, and track the decay muons. For each energy and theta bin the momentum resolution and direction resolution are used separately for μ^+ and μ^- from the muon look-up table [37]. Figure 3.8b shows the detection efficiency for DM decays to $\mu^+\mu^-$ channel inside the ICAL.

3.7.3 Detector acceptance

In the above two cases, we forced the particles to be generated in their respective regions. But to get the detector acceptance, the events are generated uniformly whole over the ICAL cavern i.e. including the ICAL detector and the air region.

Only the DM decays to $\mu^\pm$ channel are used and the simulation is carried out using GEANT4. Figure 3.9 shows the detection efficiency for 5 different situations.

Bands with different markers represent 5 different cases. The classification is based on their type of detection. The efficiency is obtained by taking the ratio between the numbers of events with hit in the respective detector to the total number of simulated events. The error bars in each case correspond to the statistical uncertainty. In cases I and II, these are small due to smaller detection efficiency.

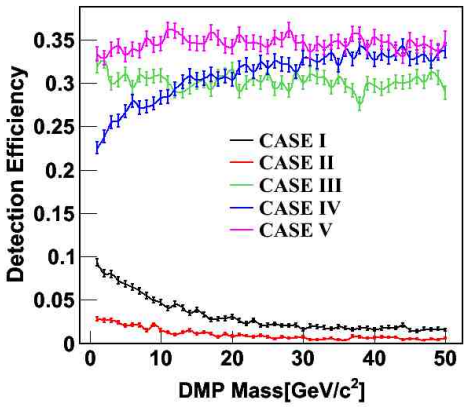

Figure 3.9: The detector acceptance by considering the DM decays to μ pair in the whole ICAL cavern. CASE I: Not detected, CASE II: 2 or 1 in ICAL not in SD, CASE III: 2 in SD and not in ICAL, CASE IV: 1 in ICAL and 2nd one in SD, and CASE V: 1 in SD and another one is not detected.

The cases II and IV are sensitive to DM decay detection. The Case III is also sensitive if absorbers are placed between SD and is relevant for low mass of DM.

3.8 Detection efficiency for DM decay to e and τ pairs

As τ is the heaviest lepton with a short life time ($\sim 0.29 \times 10^{-12}$ s), its decay products include hadrons, muon, electron and their corresponding neutrinos. As the ICAL detector will use 56 mm thick iron plates it will be difficult to separate electrons from π decays. As the τ mass is 1.7 GeV/c^2, the DM mass is varied from 6 GeV/c^2 to 50 GeV/c^2 in this decay channel.

When a DM decays to a τ pair, it will either result in a bunch of hits or a clean muon track in the detector, depending on the decay products. The detection

efficiencies are also obtained for DM decays to e^+e^- and $\tau^+\tau^-$ mode. They are obtained by using the minimum number of hits in the ICAL detector and shown in the right panel of the Fig. 3.10. Even though it is difficult to identify $e^{\pm}$ from hadrons, which mainly lead to showers, the detection probability grows with increasing mass of DM and saturates beyond $\sim 20\,\mathrm{GeV/c^2}$. The detection efficiency for $\mu^{\pm}$ channel obtained in similar way is also shown in the same plot.

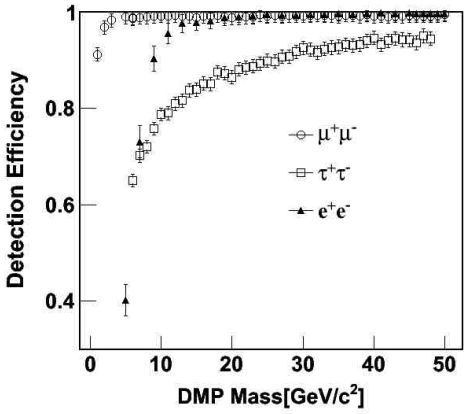

Figure 3.10: The detection efficiency for DM decays to e, μ, and τ channel in air region of the ICAL cavern as a function of DM particle mass.

The GEANT4 simulation tool-kit is used to do the simulation for DM decays to $\tau^+\tau^-$ channel. As τ decays to other particles in two- and three-body decay modes on a time scale of $\sim$ps, it is easier to do the simulation in GEANT4 instead of a simple Monte-Carlo simulation.

3.9 Studies of possible background

Since the expected DM particle decay events are small, understanding and suppressing the background is very important. So in order to extract the actual signal from various backgrounds, we identify the sources of background and how to reduce it.

The schematic diagram for DM decay event, muon event and neutrino event are shown in Fig. 3.11. The characteristic signature of each of these events will allow their identification using the timing information from the SDs and ICAL.

The cosmic ray muons and neutrino induced events will have tracks in essentially one direction only while the DM particle decay products will have 2 sets of tracks in opposite directions.

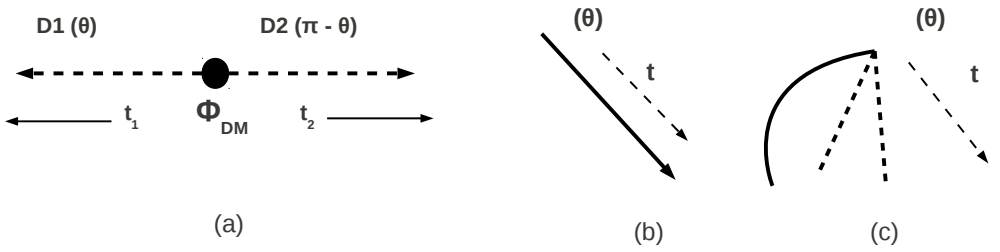

Figure 3.11: Schematic diagram of DM event (a), muon event (b) and neutrino event (c).

The various sources of backgrounds for the DM event decaying in the air region are cosmic ray muons and induced events from neutrino interactions with the rock of the ICAL cavern. These background events originate from outside the ICAL cavern while those that arise from DM decay arise inside the ICAL cavern. This can be identified and eliminated by using time of flight method as demonstrated in Figs. 3.13,3.14.

An event coming from outside the ICAL cavern fires detectors in a increasing time sequence, so that it first enters the SDs (t_1) and then the ICAL (t_2), respectively, as shown in Fig. 3.12a. But in case of the DM decay products, this sequence could be increasing or decreasing, depending on the vertex position of the decay products, as in Fig. 3.12(b,c,d). If the vertex position is close to the SD or ICAL, it may be identified as an event arising from outside or generated in ICAL. The time taken by the outside particle to travel a distance from the SD to the first layer of the ICAL detector is finite, where as for the DM decay products which originate between these two detectors have a smaller time difference.

Hence a DM decay event can be captured by using a time window in the difference in time of two detectors ($\delta t = t_1 - t_2$). The simulated δt vs distance (ds) between SD and ICAL has been plotted in Fig. 3.13. Events shown by blue solid circles in the plot corresponds to upcoming muons and black solid triangles

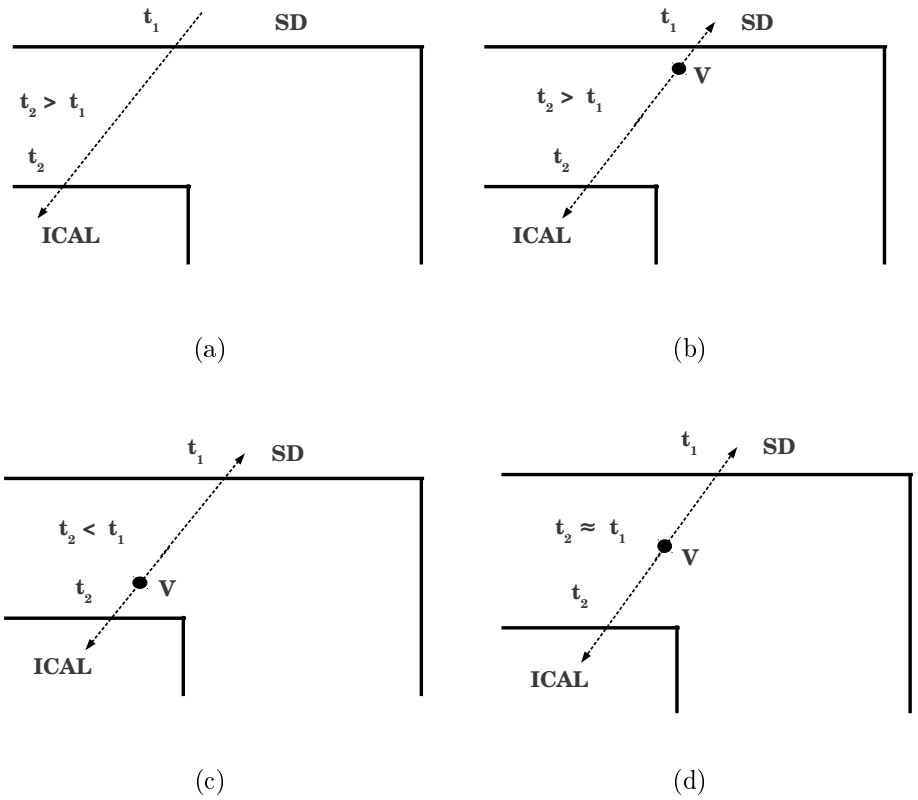

Figure 3.12: (a) The track of a muon event coming from outside. (b,c,d) The vertex position of a DM event at three different positions inside the ICAL cavern between the SDs and the ICAL.

represent DM events.

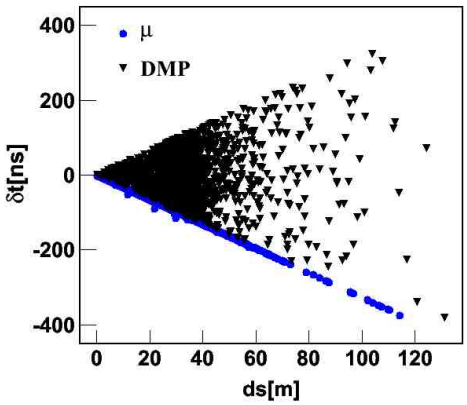

Figure 3.13: The distance between hit points vs time difference.

In other words, the difference between the time taken for a relativistic particle to travel the same distance and the mod of δt is equal to 0 for a particle coming from outside. But in case of DM decay equidistant from the two detectors this will be ds/c, where 'c' is the velocity of light. So their difference will be a positive quantity but some times it is negative due to the detector time resolution of 1 ns. The left panel of the Fig. 3.14 shows such a distribution for a DM with mass 10 GeV/c^2 and the other plot (right panel) represents the fraction of events having time difference $>$ 8.5 ns. Such an analysis cut on the time difference drastically reduces the number of background events to about 10^{-3} in 10 years.

In case of decay of the DM inside the ICAL detector, the possible backgrounds are eliminated by considering the fiducial volume of the ICAL detector and by estimating the probability of getting such type of event due to the chance coincidence rate.

The fiducial volume of the ICAL excludes two layers from the top and bottom surface of the ICAL and three strips of the RPC detectors in the ICAL on either side. So mainly the fully contained events are considered for this purpose.

The events having hits in at least 5 layers of RPC detectors of the ICAL are considered for energy reconstruction. So in case of decay of DM inside the ICAL, the background arises from events with similar feature viz. those with hits in 10 consecutive layers leading to a chance coincidence rate of $<$ 1 in 10 years. This is obtained by assuming the time window of 10 ns and RPC strip rate of 200 Hz

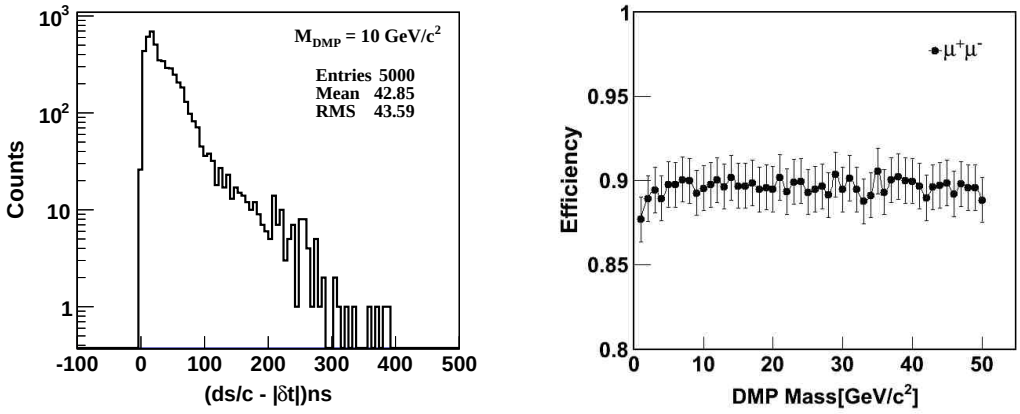

Figure 3.14: Left: The distribution of difference between propagation time of relativistic decay products of 10 GeV/c^2 DM and mod of δt. Right: The fraction of events obtained from putting gate on the time difference vs DM mass.

(incl. noise). This number is negligible in comparison with that expected from the estimated life time of the DM.

Inside the ICAL the background for such events will be arise from neutral current (NC) interactions induced by neutrinos. However the main difference between them is that in a NC event all the particles will be in one direction, whereas in DM decay the decay products will be on either side of a single vertex resulting in an increase in the time with hit position in both the directions.

All these backgrounds are very small. So for the life time estimation and number of expected events it is assumed to be zero.

3.10 Frequentist approach to the life time estimation

In the following we have used the Frequentist approach as it is well suited for the poison distribution.

3.10.1 Life time of DM

The efficiencies obtained in different regions from §3.7 are used to estimate the life time of DM for a finite number of observed events using Frequentist Method [8].

If ρ (GeV/cm^3) is the local dark matter density, V (cm^3) is the detection volume, ϵ is the detection efficiency, B is the branching ratio, M (GeV/c^2) is the DM mass and R (year^{-1}) is the rate of decay, then the life time T (year) of the DM is given by

$$T = \frac{\rho\, V\, \epsilon\, B}{M\, R} \tag{3.7}$$

Here, and in further calculations, the local dark matter density is taken as 0.39 GeV/cm^3 [8]. The limit on the life time is obtained by considering the upper limit of 2.3 counts for the 0 observed events and 0 background in 1 year of detector running time with 90% confidence level using Eq.(3.7). The obtained limit for different regions with mass is shown in the Fig. 3.15a by different symbols. With increase in the mass of DM, the limit on the life time of the DM decreases due to the corresponding reduction in number density in a fixed volume.

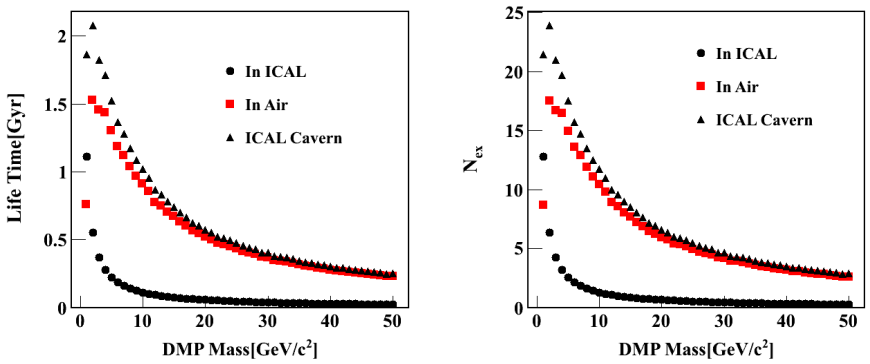

(a) (b)

Figure 3.15: (a) The lower bound on the life time of DM vs its mass for $\mu^+\mu^-$ decay channel. (b) The number of expected events due to the DM decays to $\mu^\pm$ with life time 2 Gyear at ICAL cavern for 10 years of detector running period.

3.10.2 Expected DM events

Alternatively, using the higher limit of DM life time (2 Gyear) from the above result and the local dark matter density, the number of expected events due to the decay of DM is obtained separately for events simulated in air region between cavern wall and ICAL detector, inside the ICAL detector and the whole of the ICAL cavern by combining the first two results. The expression for expected number of events

($N_{\rm ex}$) due to the decay of DM is given by

$$N_{\rm ex} = \frac{\rho\ V\ \epsilon\ B}{M\ T} \tag{3.8}$$

The Fig. 3.15b shows the number of expected events for 10 years of counting for the 3 cases mentioned above.

3.11 Comparison with other experiments

In the Standard Model all massive particle should decay to lighter mass particles. Like proton, electron and bound neutron, dark matter is also long lived. The lower limit on the life time of dark matter has been estimated by detecting their decay modes. For this purpose different channels are used depending on the location of detectors and possible decay products.

The experiments at underground laboratories mainly estimate the stability of dark matter by detecting mono-energetic neutrinos from the decay. The Super-Kamiokande (SK) [90] has put a stringent limit on the life time of a DM particle with a mass greater than about 10 GeV/c^2, decaying into a ν_μ and $\bar{\nu_\mu}$. Each would have an energy of $m_{\rm D}/2$ ($m_{\rm D}$ is the mass of dark matter) and one of them could interact via a charged current interaction producing a definite energy muon in the final state. The much smaller detection efficiency for the neutrinos from DM decay is more than compensated by the much larger spatial volumes accessed. For 10 GeV/c^2 DM mass the life time is of the order of 10^7 Gyear as obtained by SK. Similarly IceCube [91] has also put limit by similar way. The ICAL detector can be used, like SK, to place bounds on the life time of DM particle in the core of the Earth, or the Sun or our galaxy.

4

Sensitivity of the INO-ICAL detector to magnetic monopoles

Sub-relativistic magnetic monopoles are predicted from the GUT era by theory. However there is as yet no firm experimental evidence of magnetic monopoles. The experimental searches have placed upper bounds on the flux of magnetic monopoles and these use various kinds of detection techniques with their characteristic sensitivity for a given detector size. In this chapter we present the sensitivity of the ICAL detector, dark matter particle detector and the ICAL engineering module for the detection of magnetic monopoles.

4.1 Introduction

The existence of *magnetic charge* (like electric charge) had been conceived by Dirac as early as 1931. Dirac's argument was an outcome of the requirement of quantization of electric charge. Similarly Grand Unified Theories also accommodate magnetic charge with a certain mass. But these theoretical ideas have not been confirmed by any experiment. The experiments have only placed bounds on the magnetic monopole (MM) flux, interaction cross-section with matter and absolute life-time of proton through MM interaction from the absence of candidate MM events.

In this chapter we report the results of the simulations that have been carried out for MMs with one Dirac charge ($g_{\rm D} \cong 68.5e$) [92] to estimate the sensitivity of the ICAL detector for MM within a mass range of $10^7 - 10^{17}$ GeV and a velocity

range from $10^{-3}c$ to $0.7c$, where 'c' is the speed of light. We have simulated the response to MMs of ICAL alone, and of ICAL combined with large scintillation detectors on the walls and ceiling of the ICAL-INO cavern.

In §4.2, we briefly review the physics of MMs. Section 4.3 explains the mechanisms by which a MM gives a signal in the detector. In Secs. 4.4 and 4.5, we discuss the future prospect of detecting the MM in the ICAL. Section 4.6 presents the enhancement in the MM sensitivity using additional detectors placed in the cavern surrounding the ICAL detector. The possibility of measurement of low mass MM by the ICAL engineering module on the surface has been presented in §4.7 and in §4.8 we summarize the results of ICAL in the context of present well established limits.

4.2 Properties of magnetic monopole

Even though there is no experimental evidence of a MM, so far, there are various theories which can accommodate, or even require the existence of single magnetic charge. Starting from classical to quantum, in Grand Unified Theories, in Cosmology and Astrophysics the motivation of its existence are well explained.

4.2.1 At the classical level

Electromagnetic theory is one of the pillars of physics. Even if it describes two different phenomena (electricity and magnetism), they are similar from all points of view except on the basis of elementary charge. Maxwell's equations (Eq. (4.1)), which unify electricity and magnetism, assume the non-existence of a magnetic charge.

$$\nabla \,.\, E = 4\pi\rho_e \qquad\qquad \nabla \,.\, B = 0 \tag{4.1a}$$

$$\nabla \times E = -\frac{1}{c}\frac{\partial B}{\partial t} \qquad\qquad \nabla \times B = \frac{1}{c}\frac{\partial E}{\partial t} + \frac{4\pi}{c} j_e \tag{4.1b}$$

The Maxwell's equations in terms of co-variant tensor is

$$\partial_\mu F^{\mu\nu} = \frac{4\pi}{c} J^\nu. \tag{4.2}$$

Where $J^\nu = (\rho_e, j_e)$ and $F^{\mu\nu} = \partial_\mu A_\nu - \partial_\nu A_\mu$.
The expression for duality field tensor is given by

$$\partial_\mu \tilde{F}^{\mu\nu} = 0, \tag{4.3}$$

where $\tilde{F}^{\mu\nu} = \frac{1}{2}\epsilon_{\mu\nu\rho\sigma}F^{\rho\sigma}$. In vacuum J^ν takes 0 value, hence Maxwell's equations are symmetric under the duality transformation. So a conversion occur between the field tensor in vacuum.

$$F^{\mu\nu} \rightarrow \tilde{F}^{\mu\nu} \qquad\qquad \tilde{F}^{\mu\nu} \rightarrow -F^{\mu\nu}$$

It corresponds to the interchange of Electricity and Magnetism $E \rightarrow B$ and $B \rightarrow -E$. This symmetry is broken by the presence of electric current (J^ν) in the expression of co-variant field tensor. *So introducing the magnetic current ($K^\nu = (\rho_m, j_m)$) in Eq. (4.3) keeps the symmetry between Electricity and Magnetism under the duality transformation also.*

$$J^\nu \rightarrow K^\nu \qquad\qquad K^\nu \rightarrow -J^\nu.$$

At a particular angle these two parameters became identical. This transformation is a rotation (by 90^0) in such two dimensional planes.

$$E \rightarrow E\ cos\ \theta + B\ sin\ \theta \tag{4.6a}$$

$$B \rightarrow B\ cos\ \theta - E\ sin\ \theta \tag{4.6b}$$

By introducing the elementary magnetic charge (ρ_m) and magnetic current density (j_m) the Maxwell's equations are modified as follows,

$$\nabla\ .\ E = 4\pi\rho_e \qquad\qquad \nabla\ .\ B = 4\pi\rho_m \tag{4.7a}$$

$$\nabla \times E = -\frac{1}{c}\frac{\partial B}{\partial t} - \frac{4\pi}{c}j_m \qquad\qquad \nabla \times B = \frac{1}{c}\frac{\partial E}{\partial t} + \frac{4\pi}{c}j_e \tag{4.7b}$$

4.2.2 In quantum description

The presence of a monopole in Magnetism explains the quantization of electrical charge. It was first introduced by Dirac in 1931, in order to explain the quantization

[92] of electric charge as given by Eq. (4.8).

$$eg = \frac{n\hbar c}{2} \tag{4.8}$$

Where g is the magnetic charge, e is the electric charge and n is an integer which can take both positive and negative values ($\pm 1, 2, 3, 4 \cdots$).

Derivation of Dirac quantization condition :
The quantization condition can be derived from a study of the motion of an electric charged particle in the field of a MM.
The magnetic field due to a MM of strength g fixed at the origin at a distance r is given by

$$B = \frac{g}{r^2}\ \hat{r}. \tag{4.9}$$

The motion of a particle with mass m and electric charge e in this field is

$$m\ddot{r} = e\dot{r} \times B. \tag{4.10}$$

The rate of change of its angular momentum is

$$\frac{d}{dt}(r \times m\dot{r}) = r \times m\ddot{r} = r \times (e\dot{r} \times B) = \frac{d}{dt}(eg\hat{r}). \tag{4.11}$$

This suggests that one can define the total angular momentum (J) as,

$$J = r \times m\dot{r} - eg\hat{r}. \tag{4.12}$$

The second term on the right hand side of Eq. (4.12) corresponds to the angular momentum due to the electromagnetic field. For angular momentum to be quantised, the components of J will satisfy the usual angular momentum commutation relations. This would imply that the eigenvalues of J_i are half integral. Since the orbital angular momentum, the first term in J, have integral eigenvalues, we get

$$eg = \frac{1}{2}n. \tag{4.13}$$

The above expression is the Dirac quantization condition (using natural units $\hbar$ and $c = 1$) [92, 93].

Dirac string:
In order to explain the relation $B = \nabla \times A$ satisfied by the magnetic field (B) after introducing a MM, the relation is valid every where except in a line going to infinity. As the concept was suggested by Dirac, this line is called the *Dirac String*.

Charge and mass of MM in classical and quantum theory:
The Dirac quantization expression does not say anything about the MM mass, it only relates the charge of the monopole to the electric charge. Considering the basic electric charge to be that of electron, the basic *magnetic charge* is $68.5e$ [94]. There are various theoretical formulation giving a range of masses for the MM [95, 96, 97]. By equating the monopole radius to the classical electron radius the mass of the monopole is $\sim$2.4 GeV [98].

The coupling constant for a MM is given by $g^2/\hbar c$. The value is $\sim 68.5^2\alpha$, which is much larger than the coupling constant for an electric charge. The interaction between two MMs,

$$g \cdot g = (\frac{\hbar c}{2e}) \cdot (\frac{\hbar c}{2e}) = e^2(\frac{1}{2\alpha})^2 \sim \alpha^{-2} \sim 10^4.$$

Where α is the Fine Structure Constant. The interaction between two magnetic charge is 10^4 times stronger than the interactions between the electrically charged particles.

4.2.3 Magnetic monopole in Grand Unified Theory

In 1974 it was realized by 't Hooft [99] and Polyakov [100] that the electric charge is naturally quantized in Grand Unified Theories (GUTs) assuming the existence of MM. This leads to a lower bound on the mass of the MM (M_{MM}), which depends on the mass of the carrier of the unified interaction (M_{x}) and coupling constant (G),

$$M_{\mathrm{MM}} \geqslant \frac{M_{\mathrm{x}}}{G}. \tag{4.14}$$

It is assumed that these are the topological point defects during the transition in the Early Universe. They are produced when a GUT group breaks into separate group, where one of them is the non-Abelian group U(1). Given below is the

transition envisaged, assuming the GUT group to be SU(5).

$$\mathrm{SU(5)} \xrightarrow[10^{-35}\mathrm{s}]{\mathrm{M_X}} \mathrm{SU(3)_C} \times [\mathrm{SU(2)_L} \times \mathrm{U(1)_Y}] \xrightarrow[10^{-9}\mathrm{s}]{\mathrm{M_W}} \mathrm{SU(3)_C} \times \mathrm{U(1)_{EM}} \tag{4.15}$$

In such a theory one can have possible structures of a GUT monopole. So considering M_{X} to be of the order of 10^{16} GeV, MM masses would be of the order of $10^{17} - 10^{18}$ GeV.

Intermediate mass magnetic monopole (IMM):
They have masses smaller than the GUT MM. Asymptotically both are assumed to be originate in similar processes. But here, the appearance is comparatively late in the Early Universe. In this case the GUT group would not yield a U(1) group at the end of the GUT phase transition, it would appear in the following transition.

$$\mathrm{SO(10)} \xrightarrow[10^{-35}\mathrm{s}]{\mathrm{M_X}} \mathrm{SU(4)} \times \mathrm{SU(2)} \times \mathrm{SU(2)} \xrightarrow[10^{-23}\mathrm{s}]{10^{9}\mathrm{GeV}} \mathrm{SU(3)} \times \mathrm{SU(2)} \times \mathrm{U(1)} \tag{4.16}$$

This lead to MMs with masses of the order of 10^{10} GeV.

4.2.4 Cosmological and Astrophysical bounds

From a cosmological point of view it is conjectured that MMs are created around 10^{-34} s after the Big-Bang. Parker [101] has obtained an upper bound on the flux of the MMs in the Galaxy. A MM would gain energy while travelling through the galactic magnetic field. The integrated rate of energy gain of all MMs has to be small compared to the time scale of the regeneration of the galactic magnetic field, leading to an upper bound on the MM flux, also known as the Parker limit. The bound on the flux of MMs with mass is given by,

$$F_M = \begin{cases} 10^{-15}\ \mathrm{cm^{-2}sr^{-1}s^{-1}}, & M \leqslant 10^{17}\ \mathrm{GeV} \\ 10^{-15}\frac{M}{10^{17}\ \mathrm{GeV}}\ \mathrm{cm^{-2}sr^{-1}s^{-1}}, & M \geqslant 10^{17}\ \mathrm{GeV} \end{cases} \tag{4.17}$$

The Parker limit has been extended by Turner et. al. [102]. The conclusion is that, the directionality of monopole can be neglected below a certain critical velocity β_{c} of the monopole, but velocities above β_{c}, the angle between the monopole

velocity and the Galactic magnetic field must be considered. The critical velocity β_c, is the reduced velocity that a monopole acquires in the typical Galactic length scale ($\sim 10^{21}$ cm), i.e.

$$\beta_c \simeq 3.5 \times 10^{-3} \tag{4.18}$$

The modified Parker limit is,

$$F_M = \begin{cases} 10^{-15}\ \mathrm{cm^{-2}sr^{-1}s^{-1}}, & \beta \leqslant \beta_c \\ 10^{-15}(\frac{\beta}{\beta_c})\ \mathrm{cm^{-2}sr^{-1}s^{-1}}, & \beta \geqslant \beta_c \end{cases} \tag{4.19}$$

4.3 Experimental techniques for the detection of magnetic monopole

The detection methods based on the MM properties, its interaction with matter, are briefly discussed below.

4.3.1 Induction method

The flux quantization of a superconducting loop or a hole in a bulk superconductor is related to the particle carrying magnetic charge [103]. When a monopole passes through a superconducting loop it interact electromagnetically with the macroscopic quantum state and induces electromotive force as well as a current. If the particle carry the Dirac charge, the flux changes in the loop by two quantized flux units. If 'N' is the number of turns in the coil and 'L' is the inductance, then the change in current (Δi) is

$$\Delta i = \frac{4\pi N g_D}{L} = 2\Delta i_0, \tag{4.20}$$

where 'Δi_0' is the current change corresponding to a change of one unit of the flux quantum of superconductor. The schematic view of penetration of a MM through superconducting loop is shown in Fig. 4.1.

During the early 80's, the experiment at Stanford University by Cabrera [104] performed a mass and velocity independent search for MMs by the induction method using a Superconducting QUantum Interferometer Device (SQUID) as the detector. The induction based experiment was subsequently improved upon to

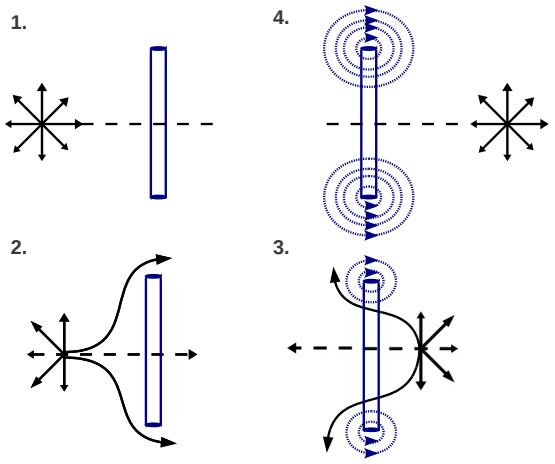

Figure 4.1: A monopole travelling through a loop of superconducting wire [103].

yield an upper bound on the flux of MMs $\sim 3.8 \times 10^{-13}$ cm^{-2} sr^{-1} s^{-1} [105].

4.3.2 Method of ionisation or excitation

In this method the detection of a MM in a particle detector is similar to that of a charged particle as both are detected through a certain amount of energy loss in the detector medium. Just as the stopping power of a charged particle depends on its charge and velocity, the energy loss of a MM also depends on its magnetic charge and velocity.

Energy losses of fast monopole:
A fast MM is characterized by its velocity $v = \beta c$ which is much larger than the typical electron orbital velocity (αc, α being the fine structure constant). For a fast MM, the electrons bound in an atomic system can be assumed to be stationary so that the MM-e collisions can be characterized by an impact parameter. In close collisions, the large energy transfer from the projectile allows the electrons to be treated as free. But in the case of distant collisions the atoms are excited by the perturbation caused by electric field of a moving MM. These approximations are valid for a particle irrespective of whether it carries an electric or magnetic charge. However there is a difference between the dependence of the stopping power of fast MM and an electric charge through the dependence on velocity. For a MM, the magnitude of the electric field is reduced by a factor of β from that of an

electrically charged particle with the same velocity and charge. For $\beta \geqslant \alpha$ it is essentially the lab frame electric field which determines the interaction between the projectile and the electrons. Since the stopping power scales as the square of the electric field, it is apparent that the ratio of fast MM stopping power to that of an electric projectile is $\sim(g\beta/Ze)^2$. Hence the stopping power expression is similar to that of an electrically charged particle which is given by modified Bethe-Bloch expression [106, 107]. In this expression the Ze term is replaced by $g\beta$ for the MM is given by

$$-\frac{dE}{dX} = \frac{4\pi N e^2 g^2}{m_e c^2}(\ln(\frac{2m_e c^2\beta^2\gamma^2}{I_m}) - \frac{1}{2} - \frac{\delta_m}{2} - B(\mid g \mid) + \frac{K(\mid g \mid)}{2}), \qquad (4.21)$$

where N is the electron number density, m_e is the mass of the electron, I_m is the mean ionisation potential of the target material, δ_m is the density correction for high energies,

$$B(\mid g \mid) = \begin{cases} 0.248 & \mid g \mid = 137e/2 \\ 0.672 & \mid g \mid = 137e \end{cases}$$

is the Bloch correction for an MM, and

$$K(\mid g \mid) = \begin{cases} 0.406 & \mid g \mid = 137e/2 \\ 0.346 & \mid g \mid = 137e \end{cases}$$

is the Kazama cross-section correction [107].

In the above mentioned velocity range the ratio between the stopping power of the MM and the relativistic singly charged electric particle is $\sim(g/e)^2\beta^2 \sim 4700\beta^2$. Due to its enormous energy loss, a MM can be detected easily by any device that can detect electrically charged particles.

Energy losses in the velocity region ($10^{-3} \leqslant \beta \leqslant 10^{-2}$):
The expression in Eq. (4.21) is valid for velocities satisfying the relation $\beta^2 \geqslant I_m/2m_e c^2 \simeq 10^{-4}$, Z $\leqslant 10$, $\beta \geqslant 10^{-2}$ [108]. For lower β, the interaction between the MM and the absorber is different. For an absorber with atoms with larger atomic numbers ($Z > 10$) the electron motion in an atom is approximated by that in a locally uniform potential, such as obtained from a Thomas-Fermi approximation. But for lower Z materials the excitation of the atom is due to the interaction of the

magnetic field of the MM with the electron magnetic moment, where the energy loss varies with β [109, 110].

The energy loss of MMs at lower β is comparatively less than that for electrically charged particles. It has been pointed by that this can be used to distinguish MM from electrically charged particles [111].

Energy losses in the velocity region ($\beta \leqslant 10^{-3}$):
For electric and magnetic charged particles, the electronic interaction predominant over others for particle velocities $\geqslant 10^{-3}$c. A MM with $10^{-3} \leqslant \beta \leqslant 10^{-4}$, lose energy via excitations with the detecting medium. So particularly detectors using noble gases [112] are most suitable for detecting MM in this β range. When the MM slows down further ($\beta \leqslant 10^{-4}$), it can not lose energy by exciting the target atom. They only lose energy in the medium via. elastic collisions with atoms and nuclei.

This method is suitable for both relativistic and non-relativistic MM, as the former will produce immense energy loss and the latter one comparatively less. But they can be detected by specific detectors such as scintillator and nuclear track detectors. The experiments MACRO [113], SLIM [114] and Soudan 2 [115] used the excitation/ionisation method for non-relativistic and relativistic MM detection as they have used scintillators, gaseous detectors or nuclear track detectors.

This method is also used in accelerator based searches. In these experiments one mainly looks for low mass monopoles with relativistic speed. Experiments such as ATLAS [116], CDF [117] and Oklahoma [118] have looked for low mass MMs.

4.3.3 Catalysis of nucleon decay

It has been suggested by Dokos and Tomara [119], that the MMs introduced in GUTs could catalyse [119] baryon number violating process of nucleon decay such as,

$$\begin{aligned} p \ + \ \mathrm{MM} \ &\rightarrow \ \mathrm{MM} \ + \ e^{+} \ + \pi^{0}, \\ n \ + \ \mathrm{MM} \ &\rightarrow \ \mathrm{MM} \ + \ e^{+} \ + \pi^{-}. \end{aligned} \tag{4.22}$$

It was believed that the catalysis cross-section is the geometrical cross-section of the monopole core $\sim 10^{-58}$ cm^2, where the unified gause bosons could be found.

However Rubakov [96] and Callan [120] showed that the cross-sections are independent of $M_X{}^2$ and could be comparable with the normal strong interaction cross-sections. Figure 4.2 shows the catalysis reaction for proton. According to them the cross-section for catalysis depends on $1/\beta^2$. If the cross-section for catalysis is large then a monopole may trigger a chain of baryonic decays along its trajectory through a large detector. If 'ρ' is the density of the detector and 'σ_{cat}' is the cross-section for the catalysis, the mean free path (λ_{cat}) is given by,

$$\lambda_{cat} = \frac{1}{N_a \rho \sigma_{cat}}. \tag{4.23}$$

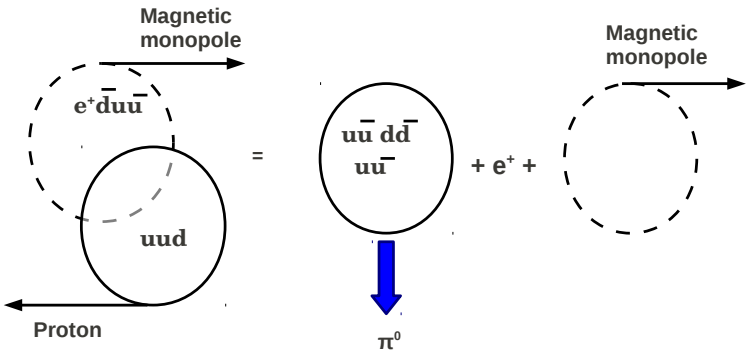

Figure 4.2: Possible process for proton decay due to the interaction of MM.

Most of the ice and water Cherenkov based detectors like IceCube [121, 122], ANTARES [123], Baikal [124] and Kamiokande [125] have also looked for light relativistic and heavy sub-relativistic MMs and have placed upper bounds on the MM flux. All these experiments have also looked for the MM through the decay of nucleon, as predicted by the Callan-Rubakov [96, 120] mechanism.

4.3.4 Time of flight method

The time of flight method is widely used in the context of measuring the speed of particles. If the velocity of a particle is significantly different from the velocity of light, then the time of flight yields valuable information that helps in determining

the mass and momentum of the particle. For non-relativistic MM this method is perhaps the most suitable.

4.4 Detection method for MM using ICAL

It may be recalled that the ICAL will use RPCs as the active detectors. So the ionisation produced by MM in this type of gaseous detector results in a saturated pulse which only carries "hit" and "time" information. The track of the MM in the ICAL and the characteristic sequence of trigger times of consecutive layers of RPCs will help in identifying the MM event against background, mainly due to random coincidences, by the time of flight method. The fast timing signal (σ $\sim$1 ns) from the RPC is used to discriminate MMs from muons in the relativistic speed region.

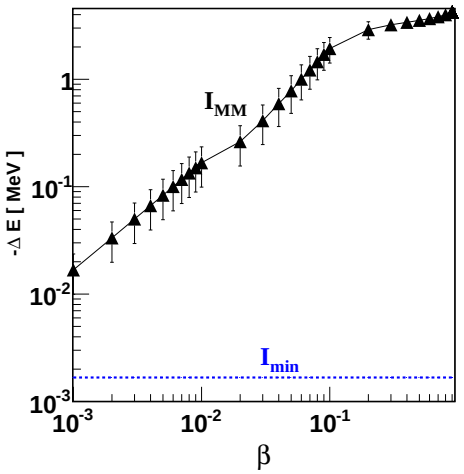

Figure 4.3: Energy loss of a MM and minimum ionising particle in 2 mm thick RPC gas (composition of gas is in text) as function of velocity in units of c.

While propagating through the ICAL detector particles lose energy in the sensitive region of the detector which has a gas mixture of R134A (95.15%), Iso-Butane (4.51%) and SF_6 (0.34%), and register "hits". This gas mixture of RPC will enable detection of MM with velocity $\geqslant 10^{-3}$c. Each hit has an associated position and time information. The plot in Fig. 4.3 shows the GEANT4 [88] simulation based energy loss of a MM in 2 mm thick RPC gas with a density 4.18 mg/cm^3 and

the composition mentioned above as a function of β. At lower β, the energy loss increases with β but at higher value it increases as $\ln(\gamma^2)$.

4.5 Simulation of magnetic monopole for ICAL

The GEANT4 [88] simulation tool-kit is used to define the ICAL detector geometry as well as to simulate the detector response for a MM passing through the simulated detector volume. The ICAL detector design as described in Chapter 2 has been implemented in GEANT4.

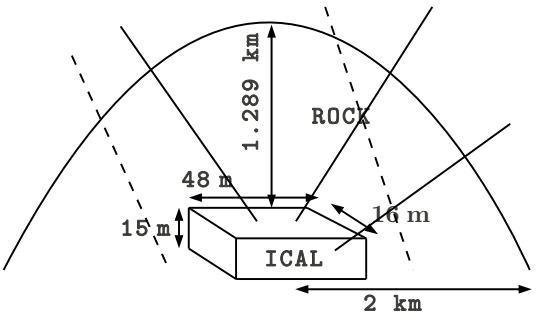

Figure 4.4: Schematic view of the MM events generation in the ICAL detector with rock.

To simulate the MM events for the ICAL at INO, a rock mass of density 2.89 g/cm^3 and of height 1.3 km from the top surface of the detector is defined in addition to the ICAL geometry (see Fig. 4.4). Particles are incident from above the rock body, so that they move through the rock losing energy before detection in ICAL. Paths crossing ICAL are represented by solid lines in Fig. 4.4. Events presented by dashed lines are discarded. To simulate an isotropic flux the zenith angle (cos θ) is smeared from 0 to $\pi/2$ corresponding to downward going MMs, and 0 to 2π in azimuthal angle (ϕ). The stopping power in different materials is used from Refs.[106, 109, 110].

The MM will be tracked by the ICAL in the form of hits by losing energy in the sensitive region of the ICAL detector viz. the RPC. Each hit has an associated position and time information. So further analysis has been carried using this information.

4.6 Frequentist approach for the estimation of sensitivity and event rate

For each mass (M) and β bin a sample of 10,000 events has been used to estimate the sensitivity of ICAL to MMs. In order to get the detection efficiency of MMs in the ICAL detector, the time and position information of each hit is used to reconstruct the velocity of a particle. If they are massive, they will not be bent during their travel through the ICAL detector with an average magnetic field of 1.3 Tesla. Hence a *straight line* fit is used to reconstruct the MM velocity.

Due to the large mass and sub-relativistic velocity, the *time of flight method* is suitable for identifying the MM. A MM with β of 10^{-3} will take 0.3 μs to travel successive layers of the active detectors in ICAL separated by $\sim$10 cm. The RPC in ICAL gives X and Y information corresponding to ionisation point with a spatial resolution of $\sim$3 cm, Z information from the layer number and the time information of the registered hit. The velocity of MM in ICAL can be reconstructed using the position and time information. So the reconstructed beta (β_{rec}) of a MM in ICAL type tracking detector is given by

$$\beta_{rec} = \frac{1}{c}\sum_{i=1}^{n-1}\left(\frac{\sqrt{((x_0 - x_i)^2 + (y_0 - y_i)^2 + (z_0 - z_i)^2)}}{t_i}\right), \tag{4.24}$$

where 'n' is number of fired layers, 'c' is the velocity of light, 'x_0, y_0 and z_0' are the co-ordinates in first fired layer.

The possible backgrounds for MM simulation are as follows,

1. For relativistic MMs high energy muons will constitute the main background. The uncertainty of the reconstructed β is due to the timing accuracy of the detector. This background can be minimised by requiring a minimum number of layers for the β reconstruction and by considering only values $\beta \leqslant 0.7$.

2. For slower MMs, the main background will be due to chance coincidences, which can also be minimised by requiring a minimum number of layers for reconstruction. So by requiring a coincidence of an additional layer, using Eq. (4.25) the random coincidences reduce by a factor of $\sim 2\times10^{-6}$ for $\beta \sim 0.7$ and 10^{-5} for $\beta \sim 10^{-3}$, assuming a RPC strip rate (incl. noise) of 200 Hz and

time windows of 10 ns and 50 ns respectively.

$$R = m \cdot r^m \cdot \tau^{m-1}, \tag{4.25}$$

where 'm' is the fold rate, 'r' is the noise rate of the RPC and 'τ' is the time window.

In order to suppress all the above mentioned background, the minimum number of layers is taken as 10. This reduces the background to negligibly small values. So for sensitivity calculations we have assumed that the number of background events to be zero.

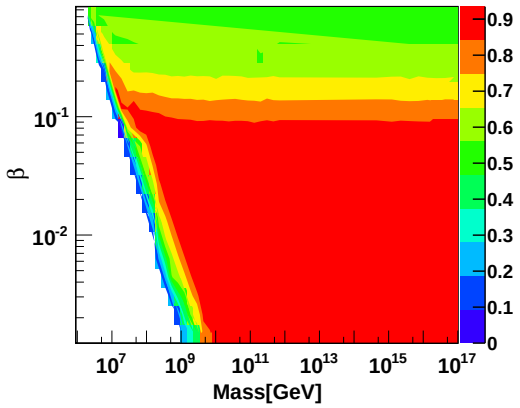

Figure 4.5: ICAL detection efficiency for MM in its M$-\beta$ plane. The efficiencies in different regions in the plot are marked by different colours as shown in legend on the right side.

Figure 4.5 represents the sensitive region for ICAL in the M$-\beta$ plane by considering 10 as the minimum number of layers for velocity reconstruction. The events with reconstructed β within 3σ of the simulated β are considered for the efficiency calculation. The different colours in the plot depict the efficiency in different regions of the M$-\beta$ plane with the value shown by the legend on the right side of the plot. In the plot the uncoloured part represents zero sensitivity of ICAL, red colour represents detection efficiency with 90% and colour coded such that the decreasing efficiency is depicted by colour with decreasing wavelength. At the lower mass and sub-relativistic β, the MMs get absorbed by the rock before reaching the ICAL. For lower β ($< 10^{-3}$) their energy loss is not sufficient to detect them in the RPC.

They travel more than 10 layers, but they may not give any signal.

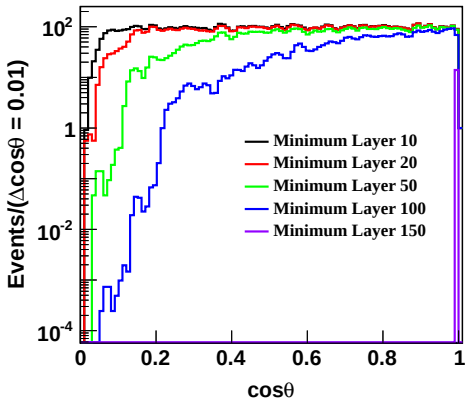

Figure 4.6: Percentage of MMs as a function of cos θ by requiring that the velocity βc is reconstructed. The colors refer to a minimum number of crossed layers equal to 10, 20, 50, 100 and 150.

Figure 4.6 shows the reconstructed event distribution for different minimum numbers of layers. An increase in the minimum number of layers decreases the acceptance towards the horizon. This problem can partly be overcome by adding scintillation detectors at the cavern walls. They not only increase the lever arm for the velocity measurement but also add *vertical* layers, improving thereby the sensitivity in horizontal direction (see section 4.6).

4.6.1 Expected event rate

In the following we calculate the number of expected events for fluxes corresponding to the present upper limits from different experiments.

If the effective area of cross-section of the ICAL detector is A, the solid angle is Ω, detection efficiency of a MM estimated by ICAL is ϵ, MM flux is f and T is the counting time period, then the expected number of events (N_{Ex}) is given by

$$N_{Ex} = f(\text{cm}^{-2}\ \text{sr}^{-1}\ \text{s}^{-1})\ A(\text{cm}^2)\ \Omega(\text{sr})\ T(\text{s})\ \epsilon. \tag{4.26}$$

Furthermore, if we choose the ICAL transverse area A = 16 m $\times$ 48 m = 768 m^2, $\Omega = 2\pi$ sr, T = 1 year, ϵ = 1 and the isotropic [126] MM flux equal to the

Parker limit [101] i.e. $f = 10^{-15}$ cm^{-2}sr^{-1}s^{-1}, we can get a rough estimate for the expected number of events as $N_{Ex} \simeq 1.5$ events per year.

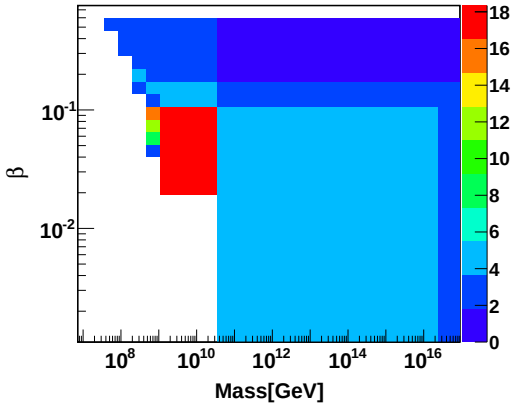

Figure 4.7: Expected number of events obtained for ICAL in 10 years live-time using flux upper bound from the MACRO and SLIM experiments.

Figure 4.7 shows expected number of events estimated for 10 years of running using a flux equal to the upper bound obtained from the MACRO [113] and SLIM [114] experiments for each pixel in the MM M-β plane. The transverse area of cross-section of the ICAL, detection efficiency for MM from Fig. 4.5 and solid angle obtained by the ICAL for minimum 10 layers from Fig. 4.6 are used for the estimation of expected events.

The number of events in different regions are presented by different colours and are indicated on the right side of Fig. 4.7. The regions with red colour indicate 18 events in 10 years. In this region the 90% C.L. upper limit on the flux (1.3×10^{-15} cm^{-2} sr^{-1} s^{-1}) obtained by the SLIM experiment is used. There is a drastic change in the number of events (from 18 to 6) at $\beta \sim 10^{-1}$ and in the mass region of $10^9 - 10^{11}$ GeV due to the bin size. A smoother variation can be obtained with a finer binning.

4.6.2 Estimation of sensitivity

An estimation of the sensitivity that can be obtained by ICAL assuming zero observed event is based on the Frequentist Method [8] including background. If the upper limit in number of events for finite observed events is N_{upper}, N_{obs} is the

number of observed events and N_{BG} is the number of expected background events, then the sensitivity is given by

$$f_{upper} = \frac{N_{upper}(N_{obs}, N_{BG})}{A(\mathrm{cm}^2)\ \Omega(\mathrm{sr})\ T(\mathrm{s})\ \epsilon}. \tag{4.27}$$

For zero observed events and zero background N_{upper} is 2.3 [8] at a 90% confidence level. The β value is confined to the region from 10^{-3} to 0.7. This procedure has been followed to get the sensitivity, which is presented in Fig. 4.8. The plot on the left panel of Fig. 4.8, represents the flux limit in the mass scale from 10^7 to 10^{17} GeV and β between 10^{-3} to 0.7. However the plot on the right panel gives the flux limit estimated by ICAL for 3 fixed β values in addition to results obtained from the other experiments.

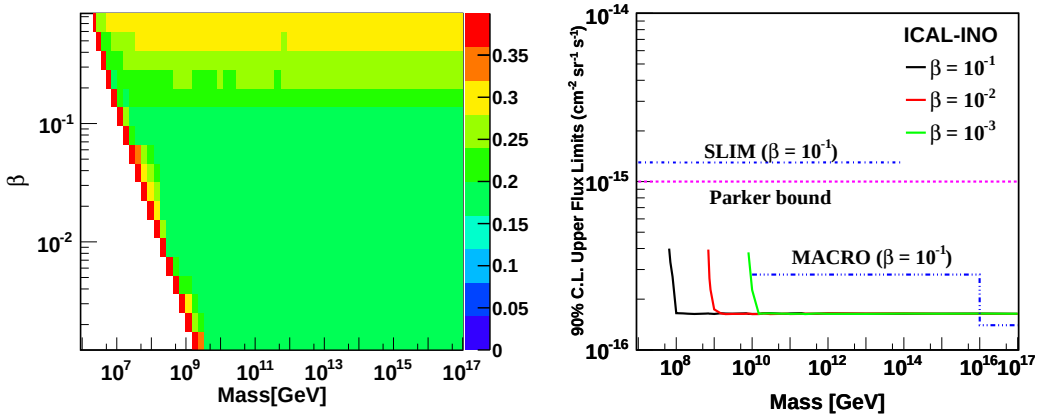

Figure 4.8: Left Panel: Sensitivity obtained by ICAL with 90% C. L. for 10 years in units of 10^{-15} cm^{-2} sr^{-1} s^{-1}. Right Panel: Sensitivity obtained by ICAL for β = 10^{-3}, 10^{-2} and 0.1.

4.7 Magnetic monopole simulation including additional detectors for dark matter particle decay

The sensitivity obtained in the previous section represents a moderate improvement of a factor of two with respect to the MACRO upper limit. For this reason, we investigated ways to further improve it. For this purpose we simulated the

combined operation of ICAL with large area scintillation detectors covering the walls and the ceiling of the cavern. These detectors have been recently proposed to search for decays of dark matter particles (DMPs) [26] as discussed in chapter 3.

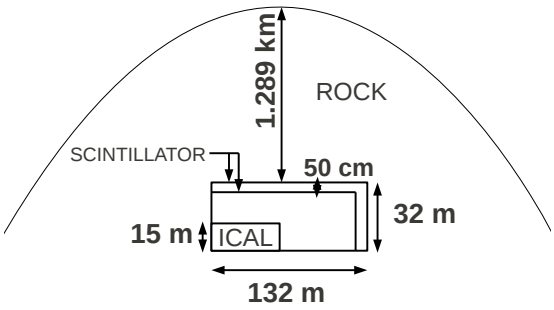

Figure 4.9: Schematic view of the ICAL detector in addition to scintillator detector with rock cover.

The tentative configuration of the DMP detectors and ICAL is shown in Fig. 3.7. The schematic diagram of the DMP detector under the rock overburden is shown in Fig. 4.9. The plot corresponds to a 2D view along the length and height of the ICAL cavern. Assuming the location of the ICAL detector towards one end of the cavern, four scintillator detectors (SDs) are mounted close to the walls of the cavern. Two of these detectors are placed along the length of the cavern with dimension of 132 m $\times$ 0.01 m $\times$ 32 m. The third one is placed in the YZ plane covering an area of 26 m $\times$ 32 m, having thickness of 1 cm. The fourth one is above the ICAL surface at a height of 17 m from the top surface of the ICAL and covering an area of 132 m $\times$ 26 m. Two layers of detectors are used for each surface with a separation of 50 cm. The separation between two layers of detectors helps to distinguish a particle coming from outside from that generated inside (as a decay product of the dark matter particle).

The GEANT4 simulation tool-kit is used with the detector geometry as described above. To calculate the detection efficiency for a MM event using the scintillator detectors and the ICAL, they should pass through the rock and the scintillator detector before detection in ICAL. As the scintillator detectors are not covering all sides of the ICAL, the combined detectors will not cover 2π solid angle as for the ICAL. The events are selected by requiring hits in a minimum of

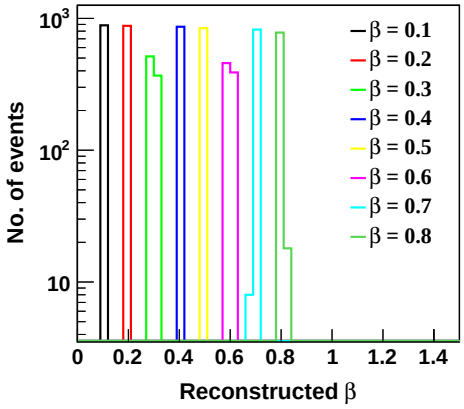

Figure 4.10: Reconstructed β distribution for MM events with 4 as minimum number of layers during reconstruction.

4 detector layers, two from the scintillator and the rest from the ICAL detector. The smaller minimum number of ICAL layers greatly improves its aperture towards the horizon. Therefore the effective aperture of the combined configuration exceeds that of ICAL alone by about a factor 2. Due to the gap between the scintillators and the ICAL detector of several meters, slowly moving particles can be triggered accurately by time of flight and the velocity can be reconstructed with an accuracy of 5-10% (see Fig. 4.10). So the time of flight method is used for a MM with β value from 7×10^{-4} to 0.8, for the same range in the mass of MM. The minimum β value of a MM is considered by considering the energy loss in the scintillator in order to get the signal from the photomultiplier tube (PMT). However this detector configuration can also be used for detection of fast monopoles, by the method of ionisation in the scintillator detector.

The background due to high energy muons can be eliminated for such a detector configuration. For scintillator detector the main background will be due to the radioactivity from the rock, but by demanding coincidences with a few ICAL layers that can also be suppressed. The left panel of Fig. 4.11 represents the detection efficiency for a MM in its mass-β plane. Most of the region in the plot shows an efficiency of 90%.

The plot on the right panel of Fig. 4.11 shows the sensitivity in the MM flux, obtained for 0 observed event with 0 background using the modified geometry for running time periods of 10 years. This limit is estimated by using Eq. (4.27). The

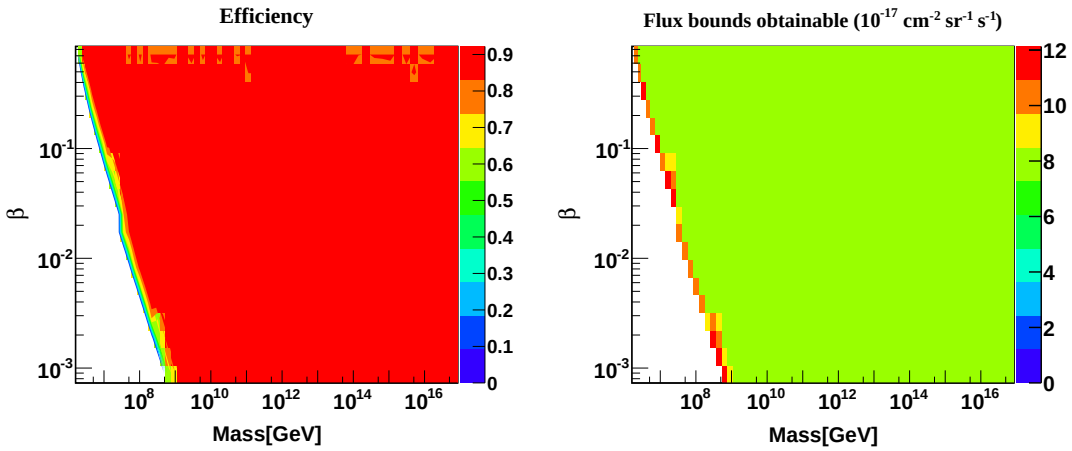

Figure 4.11: Left Panel: The MM detection efficiency with new detector geometry at the underground laboratory. Right Panel: Sensitivity obtained by ICAL with 90% C. L. for 10 years duration.

obtained limit is of the order of $8{\times}10^{-17}$ cm^{-2} sr^{-1} s^{-1}.

4.8 Magnetic monopole simulation for ICAL engineering module

The MM simulation has been done to identify the region of M$-\beta$ space where the ICAL prototype has a reasonably good efficiency.

The same simulation tool-kit has been used as for the main detector module and the defined detector geometry[3] same as discussed in chapter 2. To simulate the events in the ICAL prototype, the events are generated randomly from the surface of the atmosphere with a height of 10 km from the top surface of the prototype detector. The $cos\ \theta$ is smeared from $0\ -\ \pi/2$ and ϕ from 0 to 2π to obtain an isotropic flux for MM. For the detection of such type of events on the surface, cosmic ray muons will be the main background. However the sensitivity for lower β is expected to increase, where one can use the time information to minimise the background due to cosmic muons. Also one has the possibility of covering the lower mass region which is not possible for the underground ICAL due to the energy loss of the MM in around 1 km rock cover.

[3]When the study was conducted it was planned to be 75 layers. Now it has been reduced to 20 layers.

The minimum number of layers used for β reconstruction is 10 for $\beta > 0.2$ and 5 for lower β. The plot on the left panel of Fig. 4.12 shows the sensitive region for MM in the M$-\beta$ plane. It covers a region starting from mass 10^5 GeV to 10^{17} GeV and β from 10^{-3} to 0.6, which is mainly in the sub-relativistic region. The plot on the right side of Fig. 4.12 represents the sensitivity obtained by the prototype ICAL for β values of 10^{-3}, 10^{-2} and 0.1. The sensitivity is obtained for 0 observed event with 0 background for 2 kton-year with 90% confidence level. For all masses with higher β the efficiency is low due to the 1 ns time resolution of the detector.

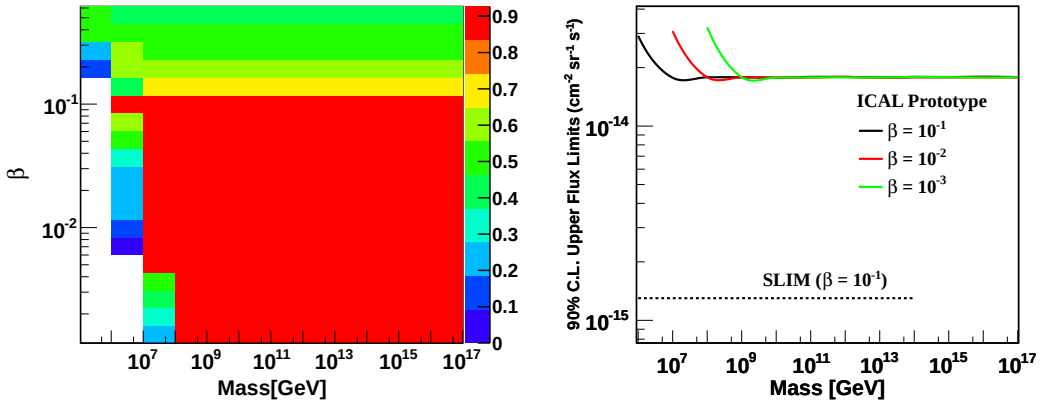

Figure 4.12: Left Panel: Efficient region of MM using ICAL prototype in the M$-\beta$ plane. Different colours in the plot present different values of the efficiencies. Right Panel: Sensitivity in flux estimated by prototype ICAL for $\beta = 10^{-3}, 10^{-2}$ and 0.1.

4.9 Comparison with other experiments

An experimental search using a SQUID was made by Cabrera in 1981 for search of cosmic ray monopoles by induction method using a 5 cm diameter coil with an ambient magnetic field of 5×10^{-8} G. In an exposure of 151 days. He found an event consistent with the passage of a singly charged magnetic monopole. The observation of only one event corresponds to a monopole flux $\sim6.1\times10^{-10}$ cm^{-2} sr $^{-1}$ s^{-1}. An experiment by Incandela et al. [127] did not report any MM event and was able to set an upper bound on a MM flux of 7.1×10^{-11} cm^{-2} sr $^{-1}$ s^{-1}. Although this method is very elegant, the construction of detector of a large enough size to measure a flux $\sim$the Parker bound, is very difficult. The limit was improved

to $\sim 7.2\times10^{-13}$ cm^{-2} sr $^{-1}$ s^{-1} (90% C.L.) by Cabrera's group using an 8-loop super conducting detector of effective area 1.1 m^2 with a coverage of 4π sr with an accumulated live time of $\sim$547 days [128].

Later on the experimental searches made use of the energy loss of the MM which is quite different from that for an electrically charged particle, sub-relativistic speed, catalysis of nucleon decay, observation of non-helical path in an uniform magnetic field. These attributes or characteristics can be used to search for MMs in much bigger detectors such as those used to search for proton decay, dark matter and measurements involving neutrinos.

The MACRO detector operating at Gran Sasso, Italy, searched for MMs in a wide range of masses and velocities. It was using gaseous, scintillator and nuclear track detectors (NTD) to track MM in different velocity ranges and in a broad range of mass (IMM to GUT). Similarly an experiment at high altitude, SLIM, has put upper limit on flux of relativistic intermediate mass magnetic monopoles. The ATLAS experiment at the CERN Large Hadron Collider put a limit of 2 fb on the production cross-section of lower mass (200 GeV) single Dirac charge MM. A summary of the best upper bounds on the flux of MMs by various experiments is given in Table 4.1.

The transverse area of the ICAL detector is of the order of 768 m^2 and is comparable to the MACRO detector ($\sim$918 m^2). The active detector in ICAL is a RPC detector with excellent time resolution. The fast time response and the 2π solid angle coverage of ICAL detector can be used to put a reasonable bound on the MM flux.

The ICAL at the underground laboratory can detect MMs with mass ranging from 10^7 to 10^{17} GeV. For the mass range from 10^7 to 10^{17} GeV ICAL is sensitive to MMs with $10^{-3} \leqslant \beta \leqslant 0.7$. The obtained sensitivity is of the order of 1.6×10^{-16} cm^{-2} sr^{-1} s^{-1} (90% C.L.) for 500 kton-years of exposure and is a factor of 2 lower than the upper bound set by MACRO at the mass above 10^{10} GeV and β above 10^{-3}.

The search can also be carried by an extended ICAL detector. The extended detector consists of ICAL with few layers of scintillator detectors covering the walls of ICAL cavern. The scintillator detectors extend the lower limit on the β of MM and also the higher limit, as the energy loss at relativistic β is huge and can be measured. The ICAL detector with additional scintillator detectors increases the

sensitivity to the MM flux by an additional factor of 2 in 10 years of live-time in the sub-relativistic region of MM leading to a sensitivity to a MM flux about 4 times lower than the present best experimental result given by MACRO.

Detector	**Type**	**Upper flux limit** (cm^{-2} sr^{-1} s^{-1}) 90% C.L.	**Note**
IBM-BNL [105]	SQUID	3.8×10^{-13}	Independent of M_{MM}, β
SLIM [114]	NTD	1.3×10^{-15}	$10^5 < M_{\mathrm{MM}} < 10^{12}$ GeV, $\beta > 0.03$
MACRO [113]	Gas, scintillator, NTD	1.4×10^{-16} 2.8×10^{-16}	$M_{MM} > 10^{10}, \beta > 0.1$ $M_{MM} > 10^{16}, \beta > 10^{-4}$ $M_{MM} > 10^{6}, \beta > 0.1$ $M_{MM} > 10^{10}, \beta > 10^{-4}$
ICE-CUBE [121, 122]	Cherenkov	3×10^{-18} $10^{-18}(10^{-17})$	$\beta \geqslant 0.8$ sub-relativistic
ICAL ICAL++	Gas Gas, scintillator	1.6×10^{-16} 8×10^{-17}	$10^{-3} \leqslant \beta \leqslant 0.7$ $7 \times 10^{-4} \leqslant \beta \leqslant 0.8$

Detector	**Lower mass limit** (MM with g_D)	**Upper cross-section limit** (pp collisions)
ATLAS [116]	200 GeV	2 fb (95% C.L.)

Table 4.1: Upper limit on MM flux and cross-section by experiments of various detector types.

5

A study of relative time resolution of glass RPC

This chapter reports on the study of the position dependence on time resolution of the RPC detector using cosmic muon data collected by a stack of twelve layer of RPC detectors at TIFR.

5.1 Introduction

The atmospheric muon neutrinos (ν_μ) and anti-muon neutrinos ($\bar{\nu}_\mu$) are the main source for the ICAL detector. They interact with nucleons through Charged Current (CC) and Neutral Current (NC) interactions. In the CC interaction of a neutrino with a target nucleon the final state has the corresponding lepton and hadrons but in a NC interaction the inelastically scattered neutrino is accompanied by hadrons. Due to the presence of a neutrino in the final state of NC interaction this process is difficult to use for getting information about the incoming neutrino. On the other hand in the CC interaction with a muon in the final state the energy and direction of the incoming neutrino can be extracted by combining the energy and momenta of the muon and the hadrons. The direction of the muon momentum, downward or upward, is derived using the time information from the RPC. Hence any improvement in the timing information will help in clearly identifying downward from upward going muons.

The RPC gives X and Y information corresponding to the ionisation produced by any charged particle, such as a muon, passing through the detector. This is

derived from the electrical signal induced by the passage of the charged particle, due to the multiplication of charge on account of the high electric field applied between the anode and cathode, on the pick-up strips of ∼3 cm width placed on either side of RPC and orthogonal to each other. Since the RPC will be operated in the avalanche mode the signal rise-time is ∼1 ns. In a CC interaction of the muon neutrino the outgoing muon track is derived from the X and Y hit information of the RPCs and the upward or downward direction is obtained by using the time information from the detector. Typically the time difference Δt between consecutive RPC layers separated by ∼9.6 cm and by considering the zenith angle from $0^0 - 75^0$ is between 0.32 to 1.24 ns. Here we would like to see the position dependent time resolution of the RPC detector using cosmic ray muons.

In Sec. 5.2, we discuss the various causes of fluctuation in timing of the detector signal. Section 5.3 presents the experimental data on timing information using cosmic-ray muons.

5.2 Detector time resolution

The detector time resolution is one of the criteria in judging the quality of a detector with respect to its response to minimum ionizing charged particles. So the time resolution describes quantitatively how precisely the time at which a particle crossed the detector can be determined. Here the time distribution is usually characterised by a Gaussian with the parameters sigma(σ) centred around a time t_0, where the time distribution is parametrized as $\propto e^{\frac{-(t-t_0)^2}{2\sigma^2}}$.

The overall time resolution of a detector arises from,

1. the fluctuation or spread in the time response of the detector,
2. contribution from the electronics (pre-amplifier and readout system which include time-walk and time-jitter), and
3. the time measurement device such as time to digital converter (TDC).

For a detector with high signal-to-noise ratio the *time jitter* is much smaller than the rise time, where as due to the different amplitudes there is a shift in the timing signal due to the use of leading edge discriminator termed as *time-walk*. This difference in amplitude arises from the avalanche process as well as

the variation in attenuation of the signal due to the position dependent signal propagation path length through the pick-up panel depending on the point of induction in the detector.

Figure 5.1 shows a schematic diagram of a RPC detector. Figure 5.1 (left) shows possible hits of muons triggering a single X-strip at 3 locations in Y-strip giving rise to 3 signal times t_1, t_2 and t_3. They have different propagation delays corresponding to their propagation distances. If d_Y is the distance travelled by the signal through the pick-up panel and v is the signal propagation velocity, the time t is

$$t = \frac{d_Y}{v}. \tag{5.1}$$

So t_3 will be delayed by 5 ns than t_1, by assuming velocity of signal propagation as 2/3 of the velocity of light (c). The shifts in timing due to variation in amplitude of the detector signal is shown in the right panel of Fig. 5.1.

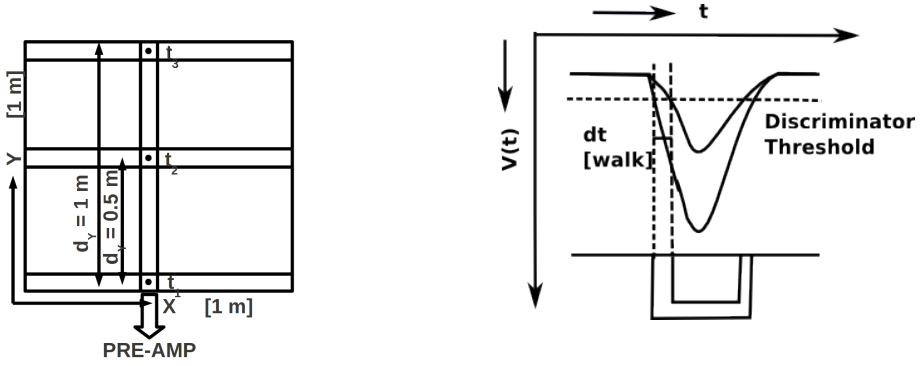

Figure 5.1: Position of hit point in a RPC (left), schematic diagram for voltage pulses showing time-walk of the discriminator output (right).

5.3 Prototype data analysis by pixel method using cosmic-ray muons

In Section 2.3, we have given a brief introduction of RPC stack at TIFR. Here we will present the analysis of the data collected by this stack using cosmic ray muons.

The analysis involves the processing of raw detector data. The raw data consist of the digitised output of detector electronic signals. Signals are induced in the detector electronics by the passage of cosmic-ray muons, which leave "hits" in active detector elements. So the raw data contains the X,Y co-ordinates of hits in terms of strip number and their corresponding time information.

5.3.1 Time walk on time resolution

As mentioned in Section 2.3, each 1×1 m^2 RPC has 32 strips per plane with a pitch of 3 cm. In the analysis, each detector is divided into 32 groups along Y-axis by considering all strips in X-axis. So each group has a cross-section of 1×0.03 m^2. Events having a hit in the triggered layer are considered for the analysis. The time resolution of a group in a detector is obtained by considering the events with both X and Y position in that group. For this calculation electronic offset and the propagation delay due to pick-up panel are taken into account.

So the time information of a hit point is given by combining the time recorded by TDC and the corresponding offset at that point,

$$\mathrm{T_{hit}} = \mathrm{T_{TDC}} - \mathrm{T_{offset}} \tag{5.2}$$

and

$$\mathrm{T_{offset}} = \mathrm{T_{eloffset}} + \mathrm{T_{stripoffset}}. \tag{5.3}$$

Where $\mathrm{T_{hit}}$ and $\mathrm{T_{TDC}}$ are respectively the time information of the hit position and the TDC. $\mathrm{T_{eloffset}}$ is the delay due to electronics for each strip on the pick-up panel. It is obtained by using cosmic ray muon data. $\mathrm{T_{stripoffset}}$ is equal to t from Eq. (5.1). The signal propagation velocity is assumed to be equal to 2/3 of the velocity of light.

The time resolution of a single detector using cosmic ray muons data is obtained from the relative time resolution i.e. time difference between two detectors. In the time difference the propagation delay between two detectors is also considered. So if $\mathrm{T_{hit}}|_1$ and $\mathrm{T_{hit}}|_2$ are the time information from first layer and second layer (from bottom to top) respectively, d_Z is the separation between two detectors and 'c' is the velocity of muon travelling with equal velocity of light, the time difference

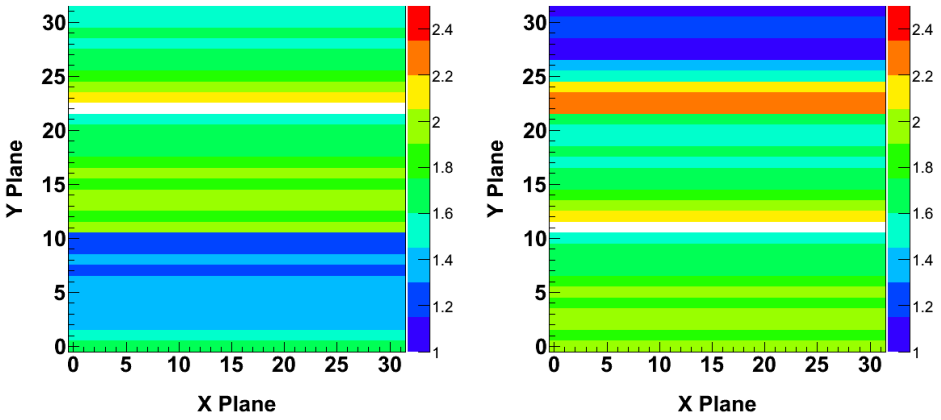

(a) Layer 4-5 (b) Layer 5-6

Figure 5.2: The σ of the relative time difference distribution obtained between two consecutive layers in row wise from left to right (Layer 4-5, 5-6)

between two layers will be,

$$\Delta T = T_{hit}|_1 - T_{hit}|_2 - \frac{d_Z}{c} \tag{5.4}$$

If σ is the standard deviation of the distribution of time difference (ΔT) between two detectors, then the time resolution of a single detector will be $\sigma/\sqrt{2}$, assuming that the two detectors are identical. In the analysis we have shown the results for σ of the distribution.

The time difference between two layers is derived from the X-TDC timing data corresponding to the X-plane. Figures 5.2, 5.4 show the standard deviation of the distribution of relative time differences in *ns* per group between two consecutive layers from third layer to twelfth layer. In the figure X-strips are along X-axis and in Y-axis Y-strips of RPC. The values of colour coding are represented by the side bar next to each plot. The distribution of time difference between 4^{th} and 5^{th} layers for 7^{th} and 23^{rd} Y-strips is shown in Fig. 5.3.

The first three layers were noisy, so they were not considered further in the analysis. For example, consider the plot in the left panel of Fig. 5.2. If we compare this with Fig. 5.1, we see a systematic variation of sigma from 0^{th} strip to the last strip along Y-axis. The deviation should be larger at end than at the beginning. The σ for the 22^{nd} strip in Y Plane has zero value as it was a dead channel. If we

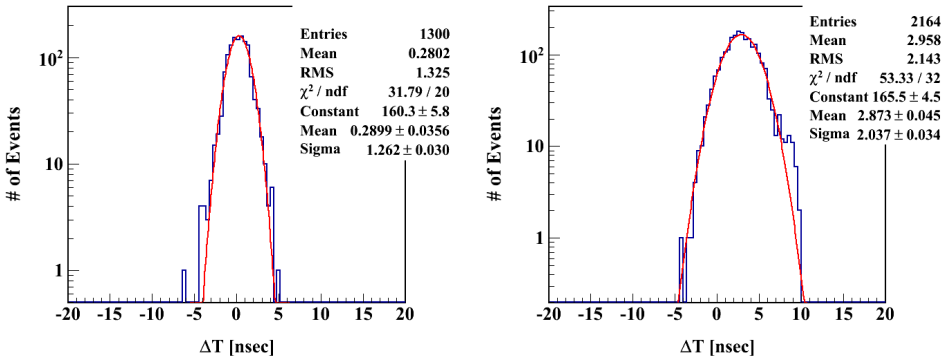

(a) 7^{th} strip (b) 23^{rd} strip

Figure 5.3: The relative time difference distribution for 7^{th} and 23^{rd} strips along the Y-axis for layer 4-5.

will study other layers, they all have similar characteristics. In summary we have observed a random distribution of σ and hence the time resolution ($\sigma/\sqrt{2}$) of a single detector along Y-axis.

5.3.2 Pixel wise dependence of the RPC resolution

In order to see the uniformity of this distribution of the time difference between two detectors, we study the pixel wise time response (hence forth referred to as the Pixel Method). Each 1×1 m^2 RPC has 32 strips per plane. In "Pixel Method" 32 strips are divided in to 8 groups with each group having 4 strips. A similar scheme has been employed for the Y-plane. So there are a total of 64 groups with each of dimensions 12 cm × 12 cm or 4 × 4 pixels. The divided area including both X and Y planes is shown in Fig. 5.5 (left) and the zoomed part of a single block is shown in the right panel.

A calculation of the relative time difference for each group has been done by considering the X and Y co-ordinates of the muon hit position in that pixel. These plots shows the homogeneity of the distribution over 1 m × 1 m RPC detector area. Some of the edge pixels have 0 events due to low detector acceptance and is an artefact of trigger logic as shown in Fig. 5.6.

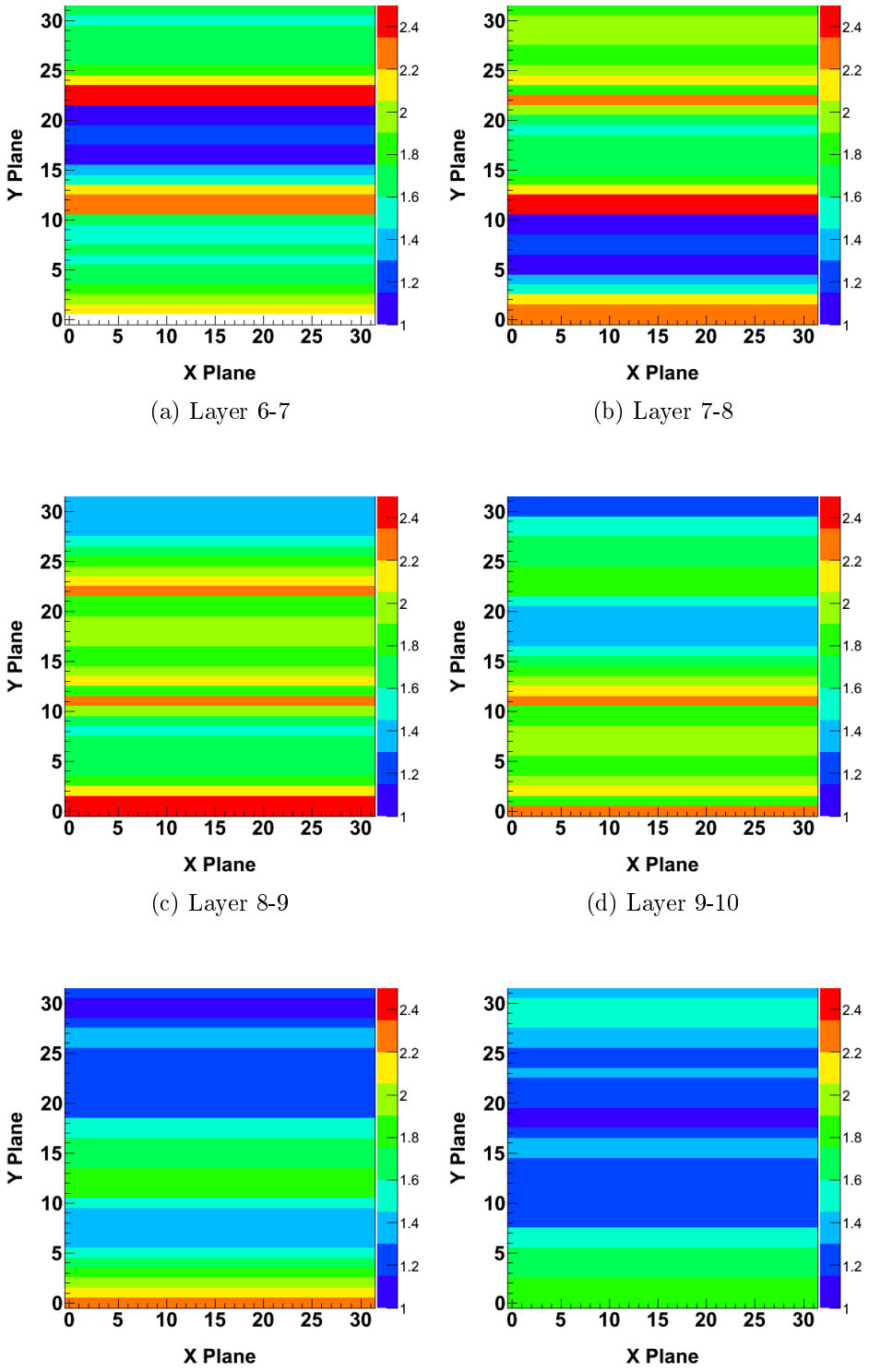

(a) Layer 6-7

(b) Layer 7-8

(c) Layer 8-9

(d) Layer 9-10

(e) Layer 10-11

(f) Layer 11-12

Figure 5.4: The σ of the relative time difference distribution obtained between two consecutive layers in row wise from left to right (Layer 6-7, 7-8, 8-9, 9-10, 10-11, 11-12)

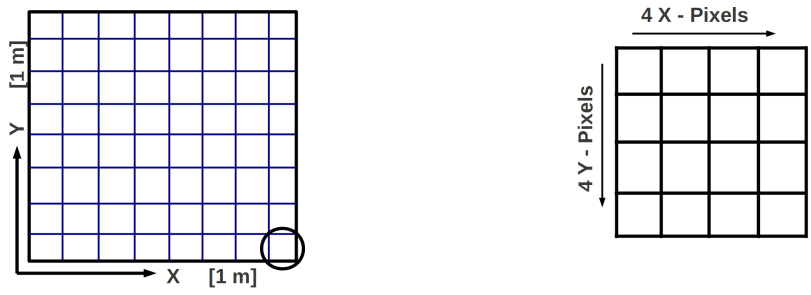

Figure 5.5: Grouping of RPC by Pixel Method with 64 pixels of size 12 cm × 12 cm (left), single pixel (right) of size 12 cm × 12 cm.

5.4 Conclusions

In summary we have measured the time resolution of the glass RPC obtained by analysing prompt time spectra using cosmic ray muons incident on the 12 layers 1 m^2 RPC stack at TIFR, Mumbai. We have not observed any systematic improvement in the time resolution of detector along the Y Plane and observed resolution is independent of path length. On the other hand the good time resolution in some areas of the spectra of 7-8 and 11-12 (1.0 to 1.4 ns) could suggest the absence of any large gap between the RPC electrode and the pick-up strip leading to a larger pulse height from a minimum ionising particle.

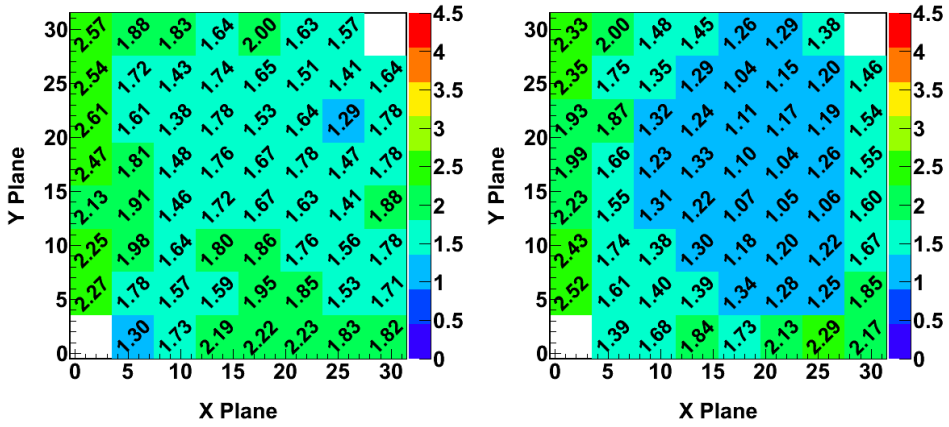

(a) Layer 6-7

(b) Layer 7-8

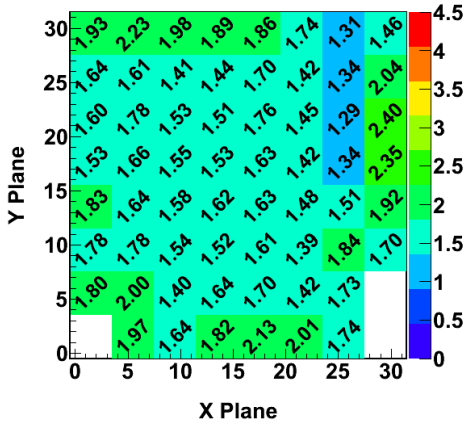

(c) Layer 8-9

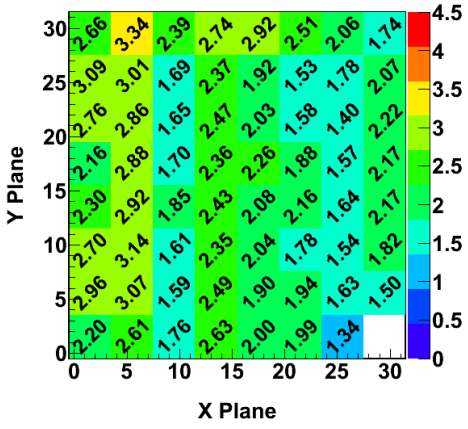

(d) Layer 9-10

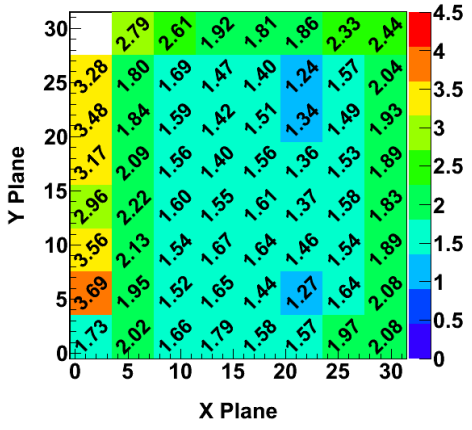

(e) Layer 10-11

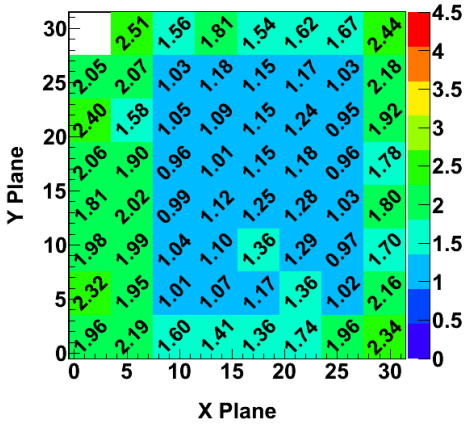

(f) Layer 11-12

Figure 5.6: The σ of the relative time difference distribution obtained between two consecutive layers in row wise from left to right (Layer 6-7, 7-8, 8-9, 9-10, 10-11, 11-12)

6

Study of correlated noise using TIFR prototype data

This chapter introduces various noise patterns observed in different layers of the RPC stack at TIFR using cosmic ray muons.

6.1 Introduction

In addition to $\nu_\mu(\bar{\nu}_\mu)$, the ICAL detector could detect atmospheric electron neutrinos (ν_e) and anti-neutrinos ($\bar{\nu}_e$). The ν_e also interact with nucleons in the same manner as ν_μ. In case of ν_μ the Charged Current (CC) interaction leads to a μ^- in the final state, and one will be able to see a clean track in the ICAL in addition to hadrons like $\pi^\pm, \pi^0$. But the observation of a clean track is possible only at high energy. At low energy due to few hits in the ICAL detector, muon and hadron tracks, together, can be mistaken for a shower. The ν_e CC event will result in an electromagnetic shower due to the e^- in the final state. As ICAL uses iron plates of 5.6 cm thickness, it is not possible to discriminate between π's and e$'$s. Apart from events containing muon track, all these events fall in the category of *muonless* events including Neutral Current (NC) events.

The properties of muonless events and the hadron produced from ν_μ CC interaction are used in physics studies. In case of hadrons, NC, low energy ν_μ CC and ν_e CC event, the energy and direction are estimated from the hit multiplicity in the detector. But if these are all true hits, the required information can be extracted accurately. In an event in addition to true hits there will also be some noise hits,

either due to electronics or genuine detector noise. So they may bias the actual information.

In this chapter, we examine the unexpected noise pattern from the TIFR RPC stack measuring cosmic ray muons. The observed patterns are with the present electronics and might be different, with bigger and larger number of detectors, in the underground laboratory environment.

6.2 Noise

Electronic noise is a very broad term that indicates everything that mixes with the signal without giving any useful information, and making the useful part less clear. So knowing the statistical properties of the signal and noise can help in separating the former from the latter. The cosmic muon data are used to estimate the correlated noise in the RPC stack. The method of data analysis and the steps followed are discussed below.

6.3 A scheme for selection of an event

In Section 2.3, we have given a brief introduction of the RPC stack at TIFR. The analysis involves the processing of the digitised output of detector electronic signals. The digitised output contains the X,Y co-ordinates of hits in terms of strip number and their corresponding layer number which gives Z. The events are selected on the basis of strip multiplicity, number of fired layers and quality of fitting.

An example of hits arising from a muon event using the stack at TIFR is shown in Fig. 6.1. As can be seen the tenth layer (from bottom to top) has more than three hits. An ideal detector will not show such type of behaviour. Either it should have $\leqslant 3$ hits or none if it is dead. So the rest of the hits may be due to electronic noise in addition to muon hit. This type of layer is the topic of interest in order to study the sources of noise.

In the analysis, events are selected by considering hits in triggered layers, irrespective of number of hits in respective layer, because the events are recorded by *self triggered* criteria. A straight line has been fitted event by event to both

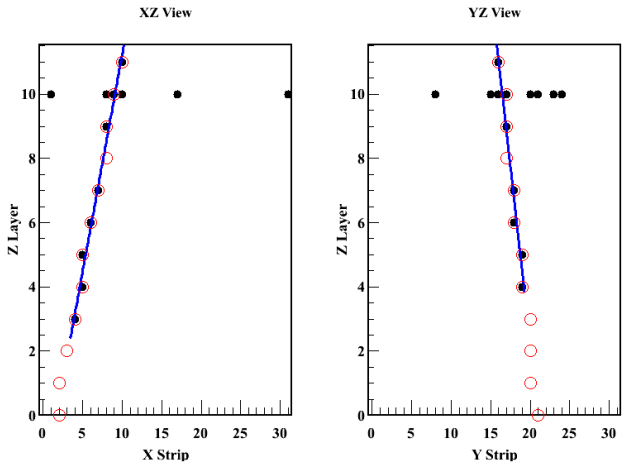

Figure 6.1: Track of a muon event, closed circles with black colour are the raw hit, open circles are the extrapolated hit points.

X-plane (XZ view) and Y-plane (YZ view) separately by considering at least six fired layers (blue line in Fig. 6.1). The layers are selected with maximum of 3 hits per layer, either consecutive fired strips or with a gap of one strip, if there is more than one hit. The fitted events are selected from the *reduced chi-square* ($\chi_\nu{}^2$) of the fitting with a maximum value of 5 for $\chi_\nu{}^2$.

From the best fit the extracted slope and intercept are used to arrive at the muon hit point for the layer with hits $\geqslant 3$ (the muon hit point is extrapolated for a layer with more than 3 hits) and for the layer which does not satisfy the above strip difference criteria. For example, the 10^{th} layer in Fig. 6.1 has hits with a separation of more than 2 strips. The correlated noise has been obtained by studying the correlation between the extrapolated hit vs other hits in the layer. This procedure has been followed for different combination of planes in a layer.

6.4 An archetype for noise studies

There are various ways to identify the correlated noise. Here we have studied the correlation between X-plane and Y-plane of same layer. So mainly we have focused on the reason behind the correlation of noise in same plane.

We have followed two ways to scrutinise the noise pattern and these are as follows,

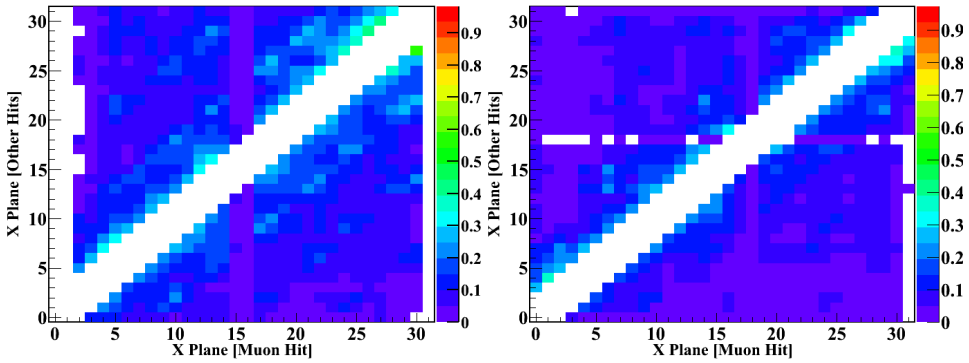

(a) May 2011 (b) May 2013

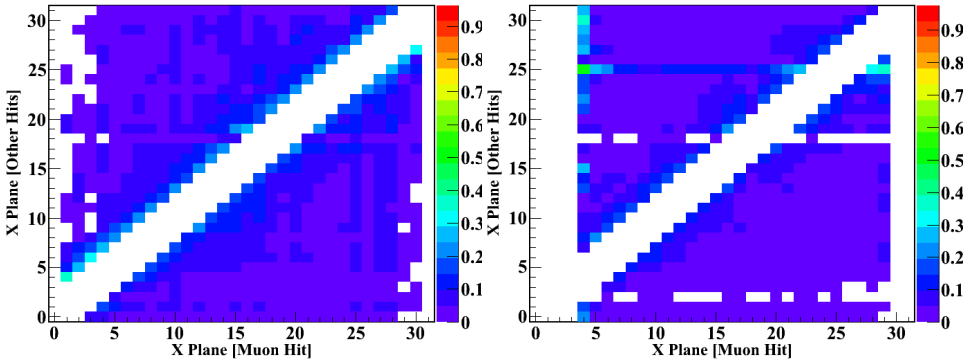

(c) August 2013 (d) March 2014

Figure 6.2: Extrapolated hit vs other hits for X-plane of fourth layer for data sets collected on May 2011, May and August of 2013, and March 2014.

1. Correlation between extrapolated hit (EH) vs other hits (OHs) in a plane of same layer.

2. Correlation between extrapolated hit in X-plane vs other hits in Y-plane for a layer and vice versa.

6.4.1 Correlation between EH vs OHs in a plane of same layer

We have studied three sources of noise for this case.

Case 1: Figure 6.2 shows the correlation between EH and OHs for fourth layer in RPC stack. EH is along the X axis and OHs along the Y axis. The diagonal

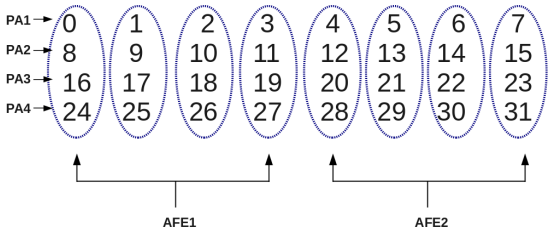

Figure 6.3: Trigger logic in RPC stack.

portion of the plot ±2 unit always shows 0 as shown by white in colour in the plot. The rest of the plot is shown by different colour whose value is represented in the legend box to the right side of each plot. These values represent the number of events, normalised to 1.

The plots shown in Fig. 6.2 are for the X-plane, for different sets of data. The off diagonal band in the first plot of Fig. 6.2 is due to the ORed combination of the strips used for Triggered Logic System as shown in Fig. 6.3. These four plots are plotted using the data files taken at different times. So mainly it shows the variation of band with time for fourth RPC layer in the stack. It is due to the reflection in trigger logic, which is mainly due to a loose connection.

Similarly Fig. 6.4 shows the correlated noise produced due to the reflection from the trigger module for the Y-plane of fourth layer.

Case 2: In Fig. 6.5a, a patch of band parallel to X axis from strip 1 to strip 5 along Y axis is due to noise. Figure 6.5b shows the raw data strip multiplicity (black colour) and strip multiplicity after excluding the muon hits in layer (red colour). The strip multiplicity is 10 times more for strip 1-5 than the other strips after excluding the muon hits. This is clear evidence of a noisy channel. Two bands parallel to the Y axis for strip number 5 from X axis shows when ever there is a hit in strip 5, strips 6-11, 14, 24-17, 29 and 31 have hits. The strip multiplicity for raw data and extrapolated hit is shown in Fig. 6.5b. This suggests that there is a correlated noise which triggered them.

Figure 6.6 represents the EH vs OHs for the Y-plane of second layer of RPC detector. In addition to the correlation plot the strip multiplicity (see Fig. 6.6b) for the Y-plane using raw data sets (black line) and excluding muon hits (red line) is also presented. In Fig. 6.6a, strips 16 and 24 have maximum hits, irrespective of hits in other strips. These are the noisy strips as can be seen from Fig. 6.6b.

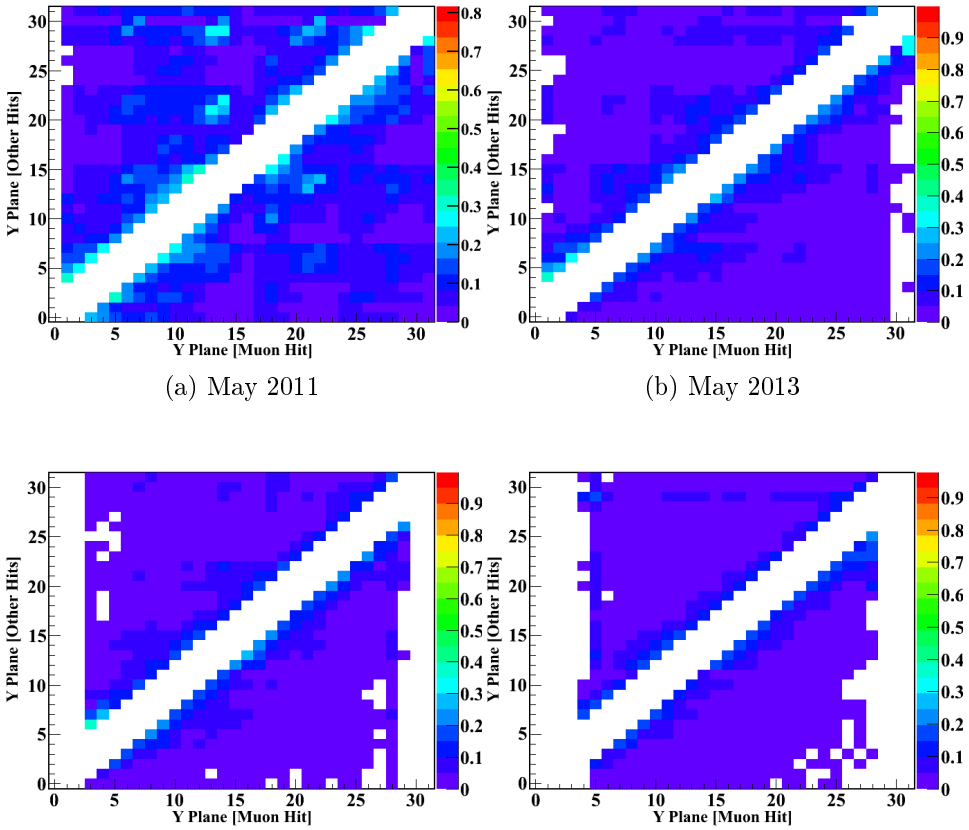

(a) May 2011 (b) May 2013

(c) August 2013 (d) March 2014

Figure 6.4: Extrapolated hit vs other hits for Y-plane of fourth layer for data sets collected on May 2011, May and August of 2013, and March 2014.

Case 3: Four Pre-Amplifiers (PA) are connected to each plane of a RPC. All 32 strips in a plane are divided into four groups, each group with eight strips are connected to a PA as in Fig. 6.3. In Fig. 6.7 whenever the strip 5 has signals other nearby strips also give hits, perhaps because the PA is fast and a signal is induced through capacitative coupling. One may draw the inference that this is because of the PA.

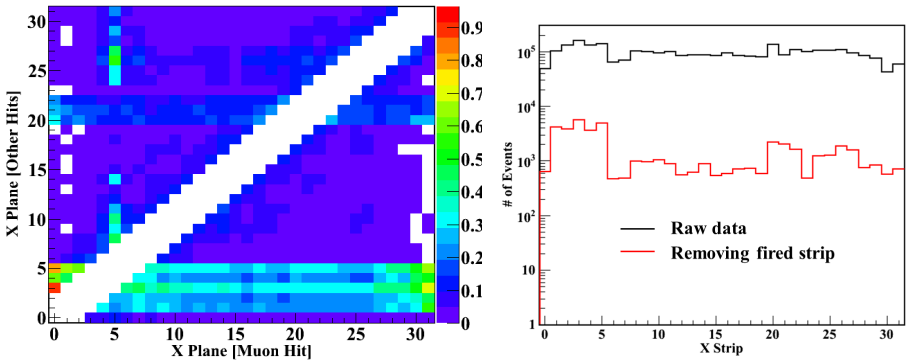

(a) August 2013 (b) August 2013

Figure 6.5: Plots for third layer of RPC stack for data sets collected on August 2013. (a) Extrapolated hit vs other hits for X-plane of third layer. (b) Noise rate for the same plane of corresponding layer.

6.4.2 Correlation between EH in X-plane vs OHs in Y-plane for a layer and vice versa

This case is similar as above, but here the muon hit from X-plane is along X axis and other hits excluding muon hits from Y-plane are along Y axis. It is represented in Fig. 6.8 and sixth layer of the stack. In Fig. 6.8a the 23^{rd} strip has hits irrespective of a muon hit in any strip from X-plane. After removing the muon hit from Y-plane if the strip multiplicity is taken in to account which is represented in Fig. 6.8b then that strip is showing high count due to noisy channel. This problem has been observed on 1^{st} July 2013 data set. But it has been sorted out on 28^{th} Aug 2013 data set which is shown in Fig. 6.8c and Fig. 6.8d.

6.5 Conclusions

The observed correlated noise in RPC, will affect the hadron energy measurement, but the expected effect in muon measurement is very small. The main noise is due to the reflection in trigger logic. Most of the dead channels are due to loose contact in between Cu-strip and signal cable.

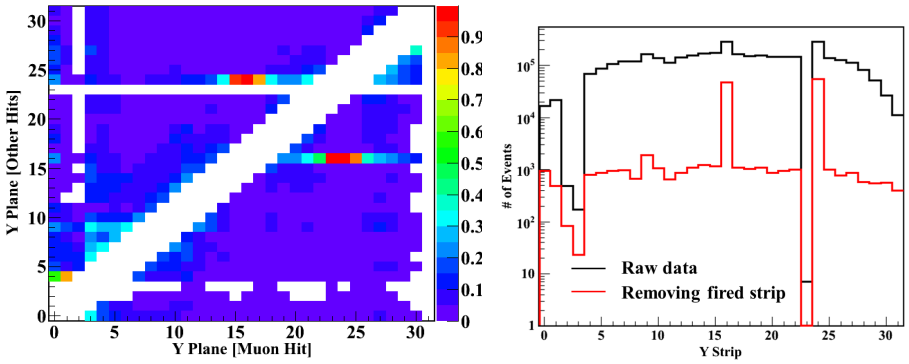

(a) August 2013 (b) August 2013

Figure 6.6: Plots for second RPC layer for data sets collected on August 2013. (a) Extrapolated hit vs other hits for Y-plane of second layer. (b) Noise rate for the same plane of corresponding layer.

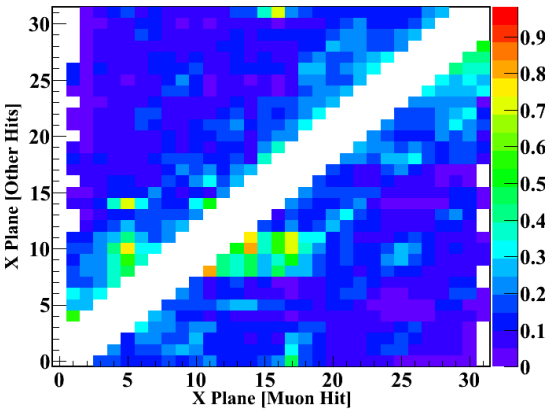

Figure 6.7: Extrapolated hit vs other hits for X-plane of third layer for data sets collected on May 2011.

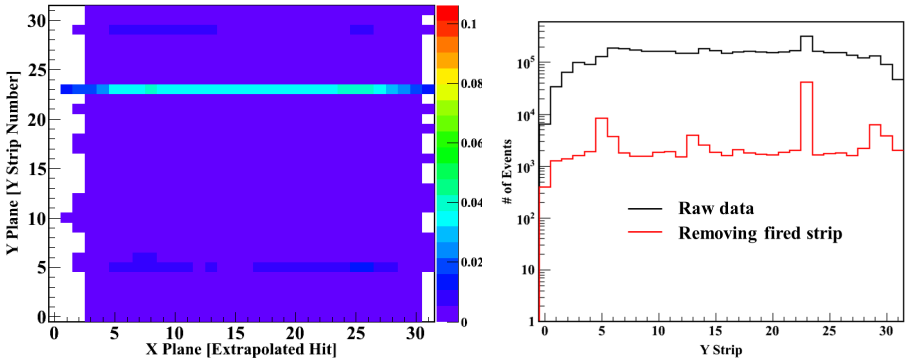

(a) July 2013 (b) July 2013

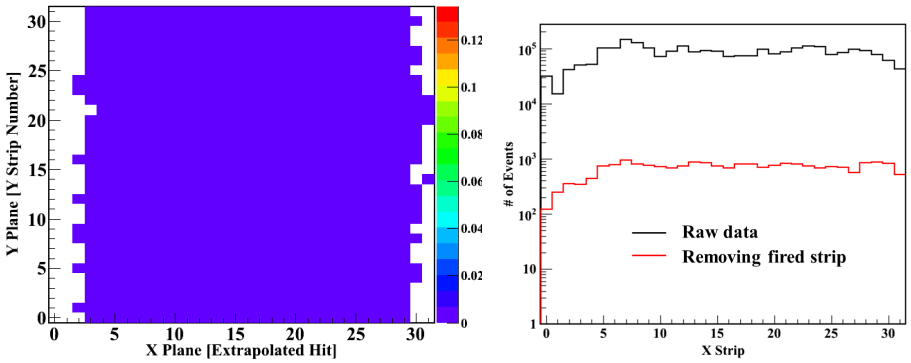

(c) August 2013 (d) August 2013

Figure 6.8: Extrapolated hit in X-plane vs other hits in Y-plane of sixth layer and noise rate in Y-plane for data sets collected on July and August of 2013.

7

Simulation studies with varying strip width in the RPCs in ICAL

A more precise measurement of the position of a hit registered in ICAL type detector, as compared to that in the baseline design, is expected to increase the sensitivity of various physics studies. The ICAL is a sampling calorimeter, where the dimensions of both absorber and active detector are important. Keeping the detector dimensions fixed, the effect of varying the RPC pick-up strip width on the reconstructed muon momentum, electric charge identification efficiency etc. has been studied. This chapter presents the results of such a study.

7.1 Introduction

The passage of a charged particle through the detector causes ionization in the gas which is subsequently multiplied in the gas medium due to the high applied electric field. This induces a tiny signal, $\sim$mV, on the pick-up panels which also transmit it to the front end electronics. Two readout units are used on either side of the glass plates and are placed orthogonally to give the X, Y co-ordinates of a hit point.

As a part of optimization of ICAL detector parameters, this chapter describes the simulation studies for different strip width dimensions of the RPC pick-up panel. It plays a crucial role in deciding the spatial resolution along the transverse direction. The measurement of the hadronic energy and the momentum of the muons in Charged Current (CC) interaction allow a reasonably good reconstruction

of the neutrino energy and as well as the direction of neutrino. So a fine-tuning of strip width in the readout panel of the RPC may result in improvement in neutrino sector. The simulations have been carried out for strip widths of 1.6, 2.2, 2.875 and 4 cm.

Hence the aim of this study is to see the influence of strip width on the physics studies for ICAL through its effect on momentum resolution, angle resolution, reconstruction efficiency, charge identification efficiency and shift in the mean of reconstructed energy of the muon and hadron. These studies are discussed in the following sections along with a brief summary on the strip width dependent signal propagation.

7.2 Effect of strip width on signal transmission

The material characterisation [129] of the pick-up panel of ICAL RPCs has already been studied from the characteristic impedance and transmission of signal without any significant degradation. Out of three type of materials i.e. G10, foam and plastic honeycomb panel, the last type of panel is used in TIFR RPC stack because of ease of matching the 50 Ω impedance requirement. This type of pick-up panel does not need any additional impedance matching circuit between panel and front end electronics.

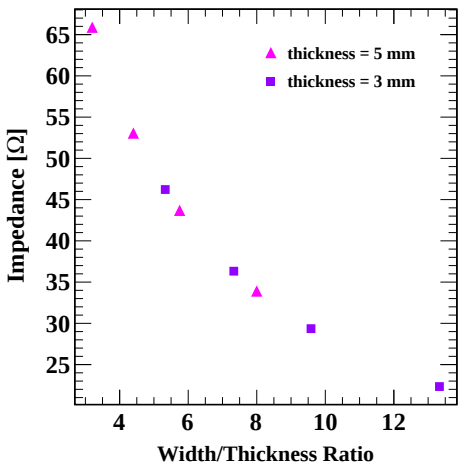

Figure 7.1: Ratio of strip width and thickness vs impedance [130].

The strip readout system consists of 5 mm thick plastic honeycomb glued with a layer of aluminium and copper on either side. The surface facing the RPC detector volume is laminated with a copper layer and divided into 28 mm wide strips, with 2 mm gaps between adjacent strips, for position information. So the structure of the panel is basically a dielectric coated with two different type of materials, one side for signal transmission and other side, coated with aluminium, for signal protection. The combination acts like a capacitor and picks up the RPC charge signal through induction.

Further the signal in the pick-up panel could be reflected and that can be avoided by using a resistor with appropriate impedance. The terminating impedance depends on strip width and panel thickness. The expression [130] for impedance (Z) as a function of ratio of strip width and panel thickness (x) is given in Eq. 7.1, where ER is related to the relative permittivity of the material (E_r) and x as in Eq. 7.2.

$$Z = \begin{cases} \frac{60ln(\frac{8}{x}+\frac{x}{4})}{\sqrt{ER}}, & x \leq 1 \\ \frac{377}{(x+1.393+0.667ln(x+1.444))\sqrt{ER}}, & x \geq 1 \end{cases} \tag{7.1}$$

$$ER = \frac{E_r+1}{2} + \frac{E_r-1}{2\sqrt{1+\frac{10}{x}}} \tag{7.2}$$

Figure 7.1 shows the impedance vs pitch width to readout thickness for four dimension of strip widths of 1.6 cm, 2.2 cm, 2.875 cm and 4 cm with 5 mm and 3 mm thick panel. In the main ICAL modules 3 mm thick readout panel has been decided. With decrease in strip width the impedance increases rapidly. The experimentally optimised strip width has been chosen as 3 cm as mentioned in Ref.[130]. It is advisable to use FR grade material pick-up panel at the underground laboratory.

In the following sections we report the results of simulation studies by varying strip width.

7.3 Simulation framework for strip width studies

The simulation framework for this study is based on GEANT4 [88]. The standalone program contains the detector geometry, Monte-Carlo event generators, propagation of particles in different materials along with the separation of muon

and hadron hits, and the reconstruction of incoming momentum and direction of minimum ionising particle i.e. muon. The three modules of ICAL along with actual dimensions, as discussed in Chapter 2, are included in GEANT4. It also used the spatially dependent B-field as generated by using the finite element 3D electromagnetic simulation of a 16 m $\times$ 16 m iron layer (see Fig. 2.2).

As muons and hadrons are produced from the neutrino interactions, these are used for this study. They are generated using a Monte-Carlo event generator with an energy range from 2 GeV to 20 GeV. The events are generated at the centre of three modules with a cosine of zenith angles (θ) of 0.55, 0.65, 0.85 and 0.95. To avoid statistical uncertainty 10,000 events are generated for each cos θ and energy bin.

The propagation of various particles in different materials of the ICAL detector are calculated using GEANT4. The co-ordinate information corresponding to muon hits are extracted and *digitised*. In this program module, the layer, chamber and RPC strip (X and Y respectively) information is stored as event by event data. Including both detector efficiency and noise the package gives the co-ordinates (X, Y and Z) of registered hit. The track finder algorithm has been used to separate muon hits and hadron hits. The steps followed in the simulation are given below,

Monte Carlo $\longrightarrow$ GEANT4 $\longrightarrow$ Digitisation $\longrightarrow$ Analysis.

The study has been carried out for single muon and pion events considering strip widths of 1.6 cm, 2.2 cm, 2.875 cm and 4 cm. *To see the effect of strip width on physics studies, ratio plots are plotted with respect to strip width of 2.875 cm.*

7.4 Effect on muon reconstruction

The incident energy and direction of muons are reconstructed from the curvature of the track. The Kalman filter [89] algorithm has been used to estimate their physical parameters. In the analysis the longest tracks in the events having reduced chi-square less than equal to 10 after reconstruction are considered.

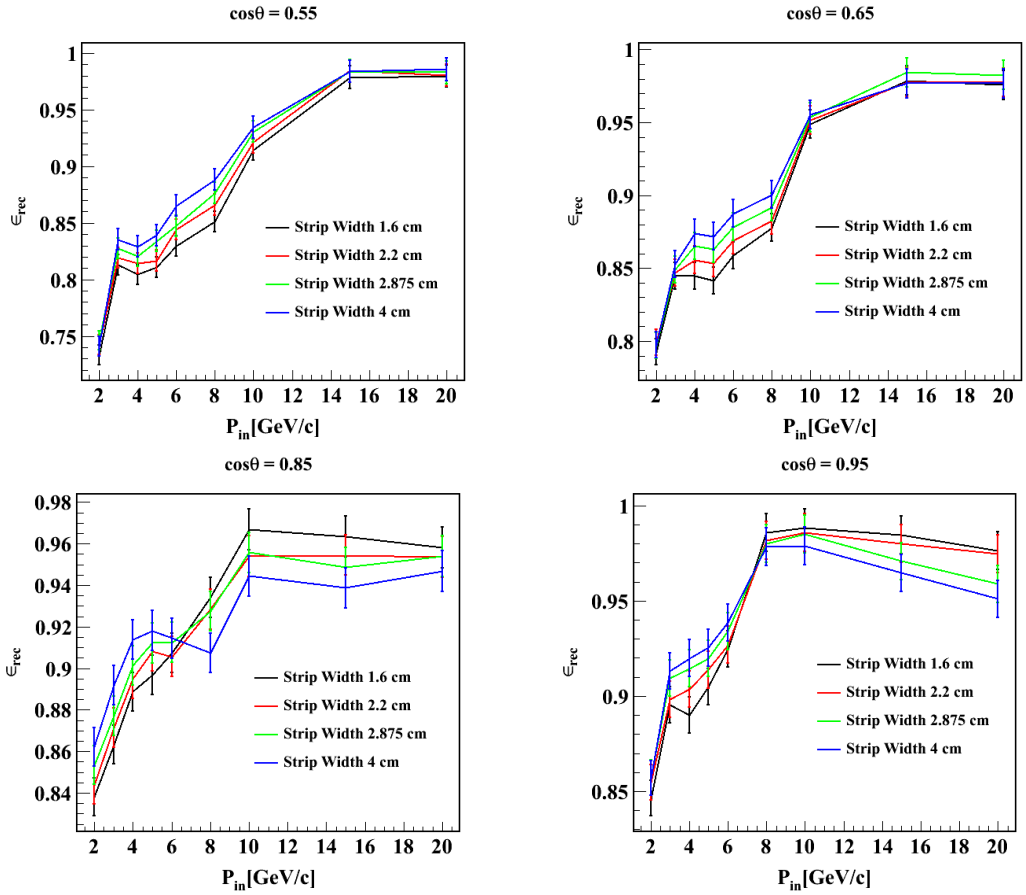

Figure 7.2: Reconstruction efficiency for different cos θ bins and for the 4 strip widths.

7.4.1 Momentum reconstruction efficiency (ϵ_{rec})

The momentum reconstruction efficiency is defined as the ratio of the number of reconstructed events within $\pm 5\sigma$ from the reconstructed distribution, N_{rec} (irrespective of charge), to the total number of generated events, $\mathrm{N_{total}}$. The results are shown in Fig. 7.2.

$$\epsilon_{rec} = \frac{N_{rec}}{\mathrm{N_{total}}}$$
$$\delta\epsilon_{rec} = \frac{\sqrt{N_{rec}}}{\mathrm{N_{total}}} \tag{7.3}$$

Figure 7.2 shows the muon momentum reconstruction efficiency as a function

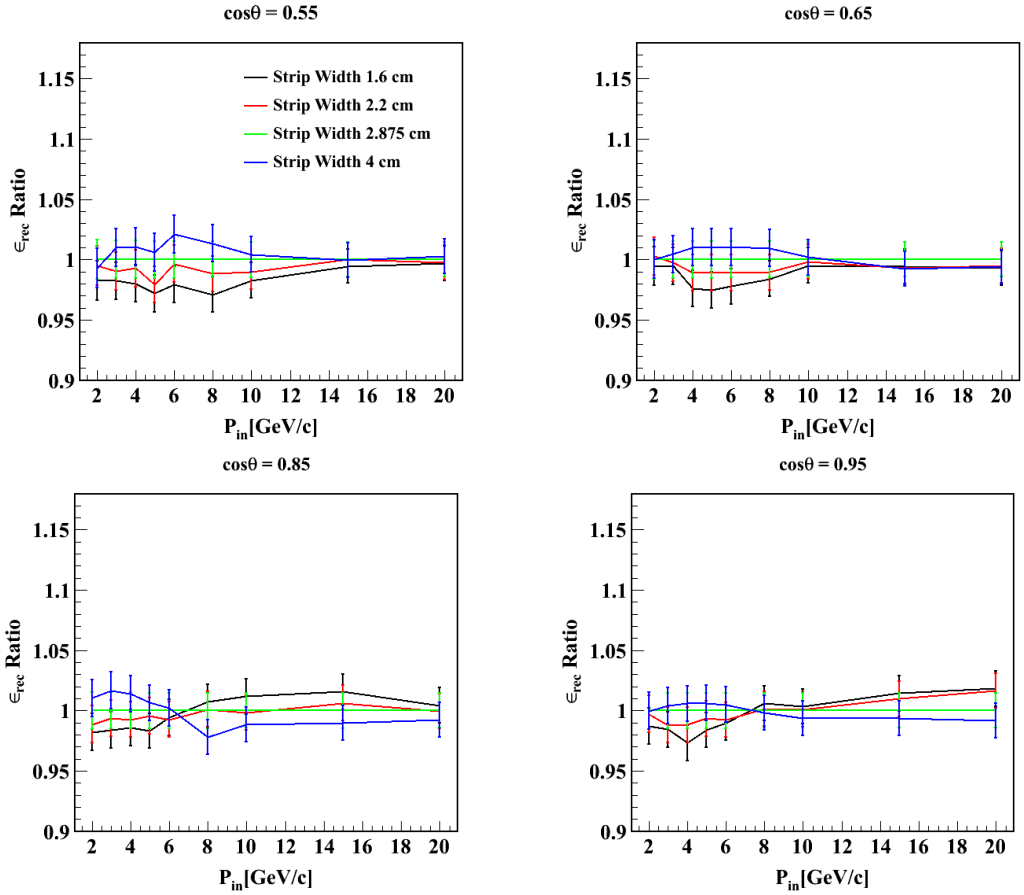

Figure 7.3: Reconstruction efficiency ratio for different cos θ bins and for the 4 strip widths.

of input momentum (P_{in}) for different cos θ bins using Eq. 7.3. Muons traverse through different numbers of layers each leading to a certain number of hits and these depend on the incident energy and angle. Muons incident at a steeper angle penetrate comparatively less number of layers than the vertical one resulting in fewer points in the track tending to worsen the reconstructed momentum. On the other hand the path length is more for a high energy muon, so the curvature, and hence momentum, reconstruction is better. Needless to say that the momentum reconstruction depends on the incident energy, direction, and the strength of the magnetic field in the detector. In general the momentum reconstruction efficiency is somewhat smaller than the track reconstruction efficiency, especially at larger angles.

So decreasing the strip width dimension may increase the momentum reconstruction efficiency at low energy and larger angle. But there is no sizable improvement in the efficiency as can be seen from Fig. 7.3.

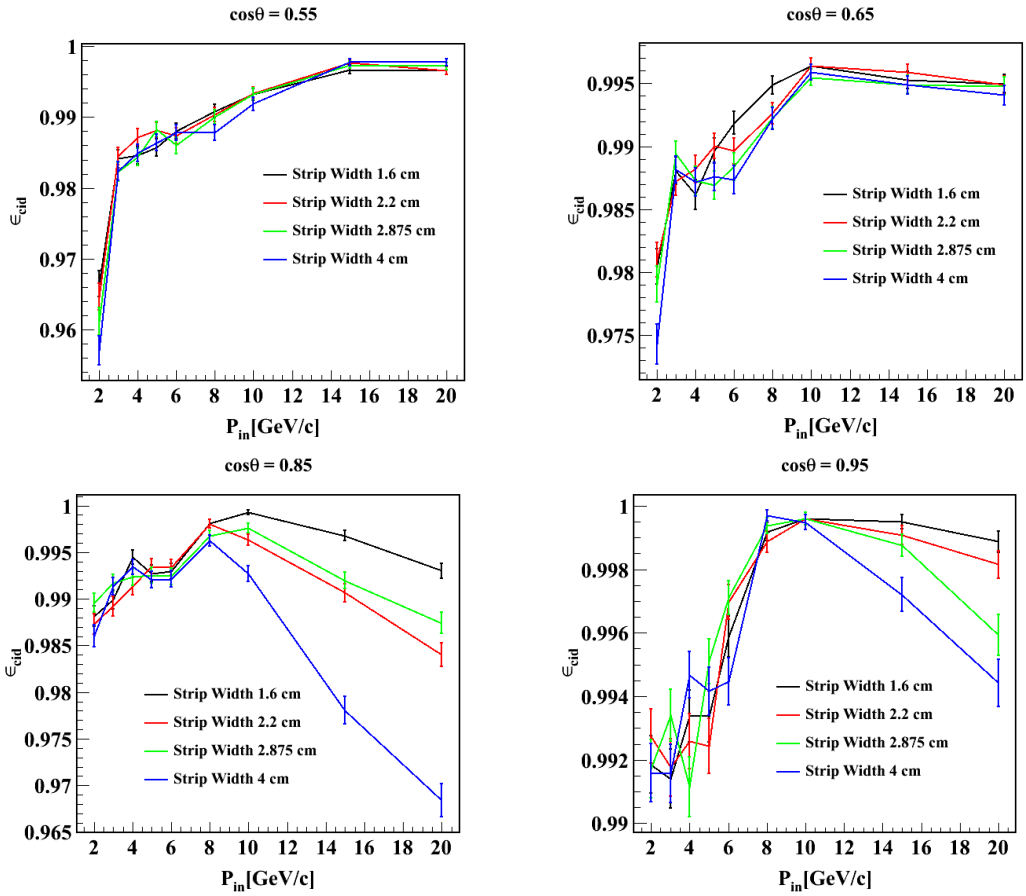

Figure 7.4: Charge identification efficiency for different cos θ bins and for the 4 strip widths.

7.4.2 Relative charge identification efficiency (ϵ_{cid})

The charge identification efficiency, ϵ_{cid}, of the ICAL detector is very important in order to distinguish between ν_μ from $\bar{\nu_\mu}$ events which are necessary for addressing the problem of neutrino mass hierarchy. The charge of the particle is determined from the direction of curvature of the track in the magnetic field. This information is then used to get the ϵ_{cid} from the ratio of events with correctly identified charge (N_{cid}) having momentum within $\pm 5\sigma$ of the P_{in} to the number of events whose

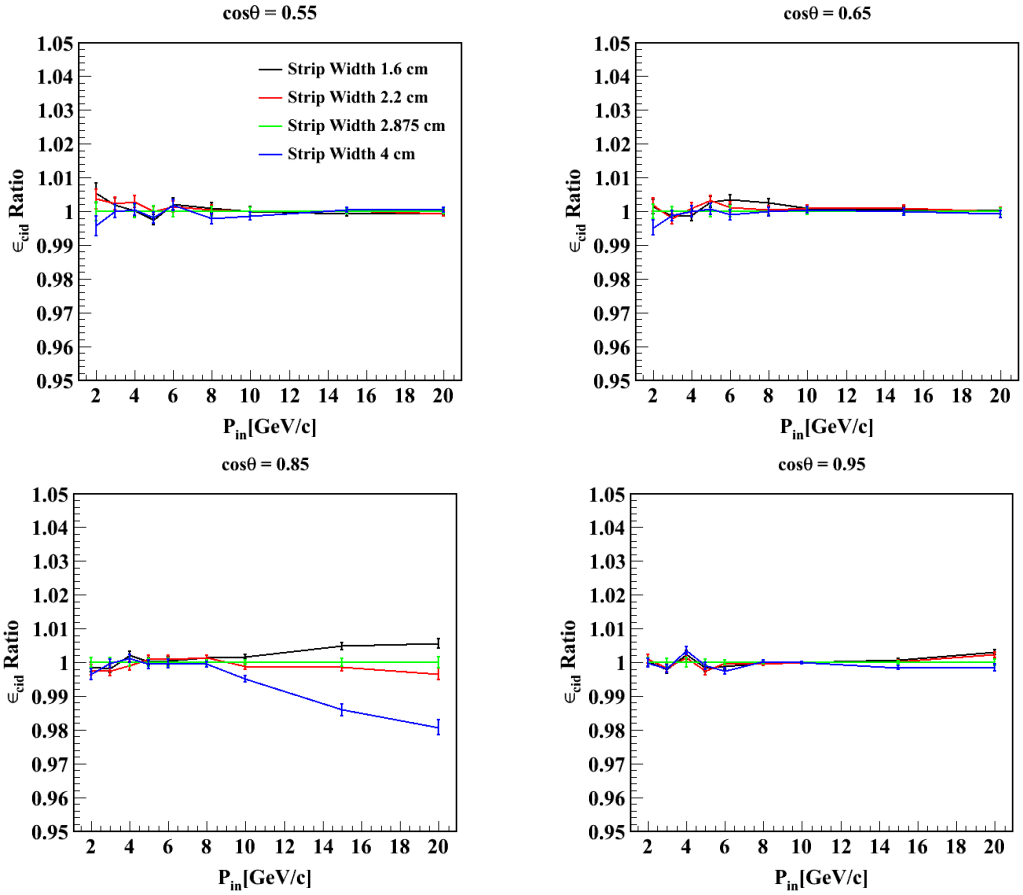

Figure 7.5: Charge identification efficiency ratio for different cos θ bins and for the 4 strip widths.

energy is well determined (N_{rec}). As both are correlated so the error in CID efficiency is obtained by Bernoulli statistics. The CID efficiency plot and the ratio plot are shown in Figs. 7.4 and 7.5.

$$\epsilon_{cid} = \frac{N_{cid}}{N_{rec}}$$

$$\delta\epsilon_{cid} = \frac{\sqrt{\epsilon_{cid}(1-\epsilon_{cid})}}{\sqrt{\epsilon_{rec}}} \tag{7.4}$$

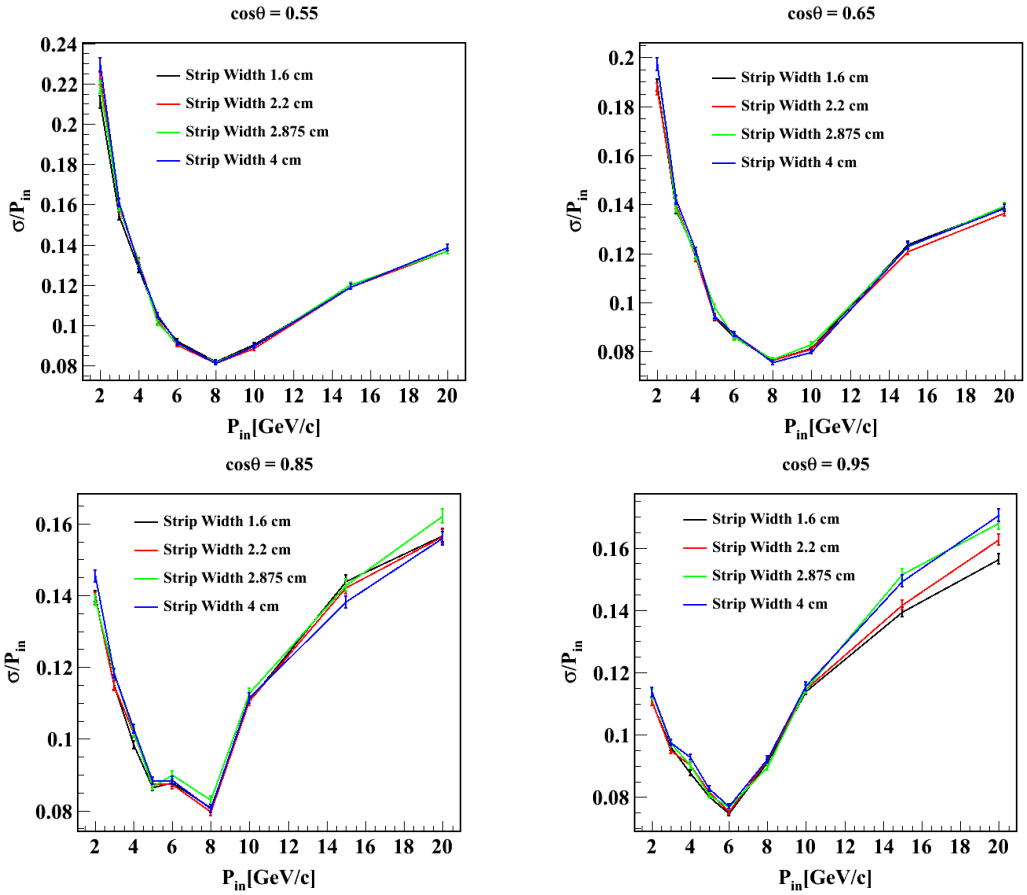

Figure 7.6: Momentum resolution for different cos θ bins and for the 4 strip widths.

7.4.3 Momentum resolution ($\frac{\sigma}{P}$)

The expression for momentum resolution is given as,

$$\frac{\sigma}{P} = \frac{a}{P} + bP. \tag{7.5}$$

At low energy the first term in the right hand side is the dominant one while with increase in energy the second term plays the role. So the momentum resolution is obtained by taking the ratio of sigma (σ) of fitted distribution and incident momentum. As the incident momentum is constant the error on resolution ($\delta(\frac{\sigma}{P})$) is obtained due to the error in fitted sigma ($\frac{\delta\sigma}{P}$). The corresponding plots are shown in Figs. 7.6 and 7.7.

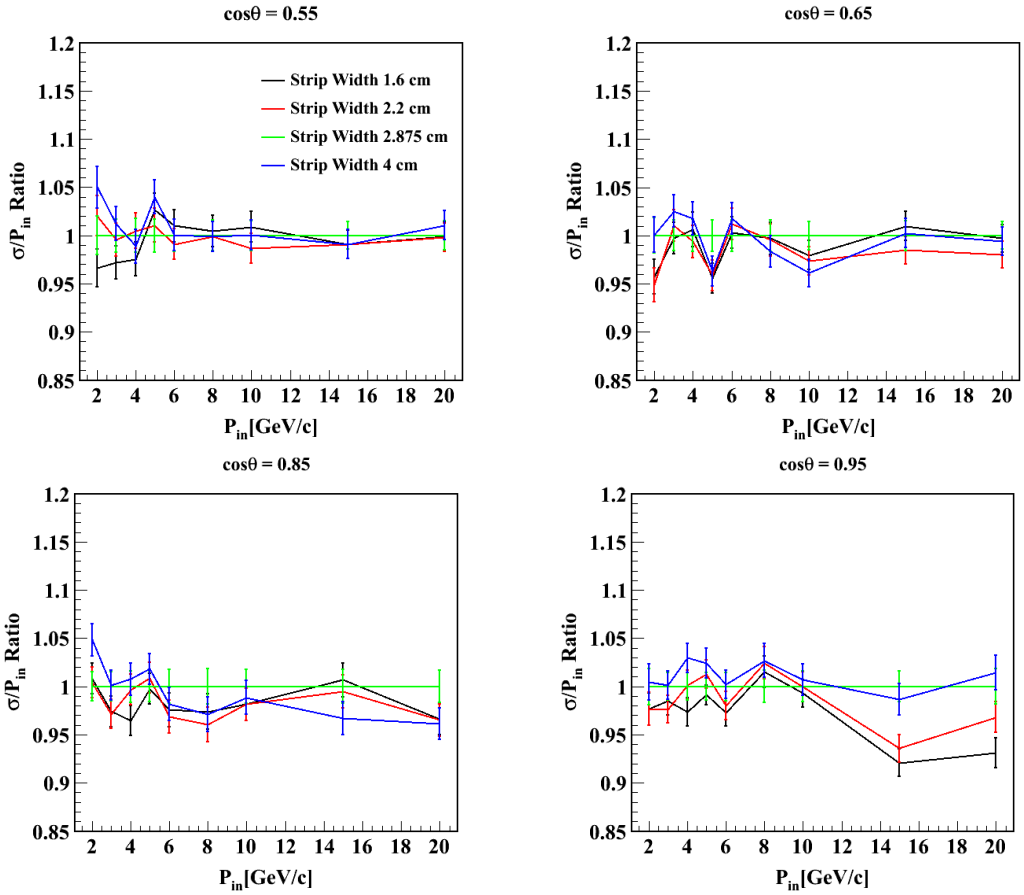

Figure 7.7: Momentum resolution ratio for different cos θ bins and for the 4 strip widths.

7.4.4 Shift in mean energy (Shift)

The mean of the reconstructed momentum (P_{rec}) distribution is approximately independent of both the polar and azimuthal angles. It is the difference between the incident momentum and the mean of the distribution of reconstructed momentum. Figure 7.8 shows the shift in the mean of reconstructed momentum, equal to the difference between the incident and mean of the reconstructed momentum, as a function of the input momentum. The shift can arise due to multiple scattering, etc., and is roughly linear beyond a few GeV/c.

$$Shift = P_{in} - P_{rec}$$

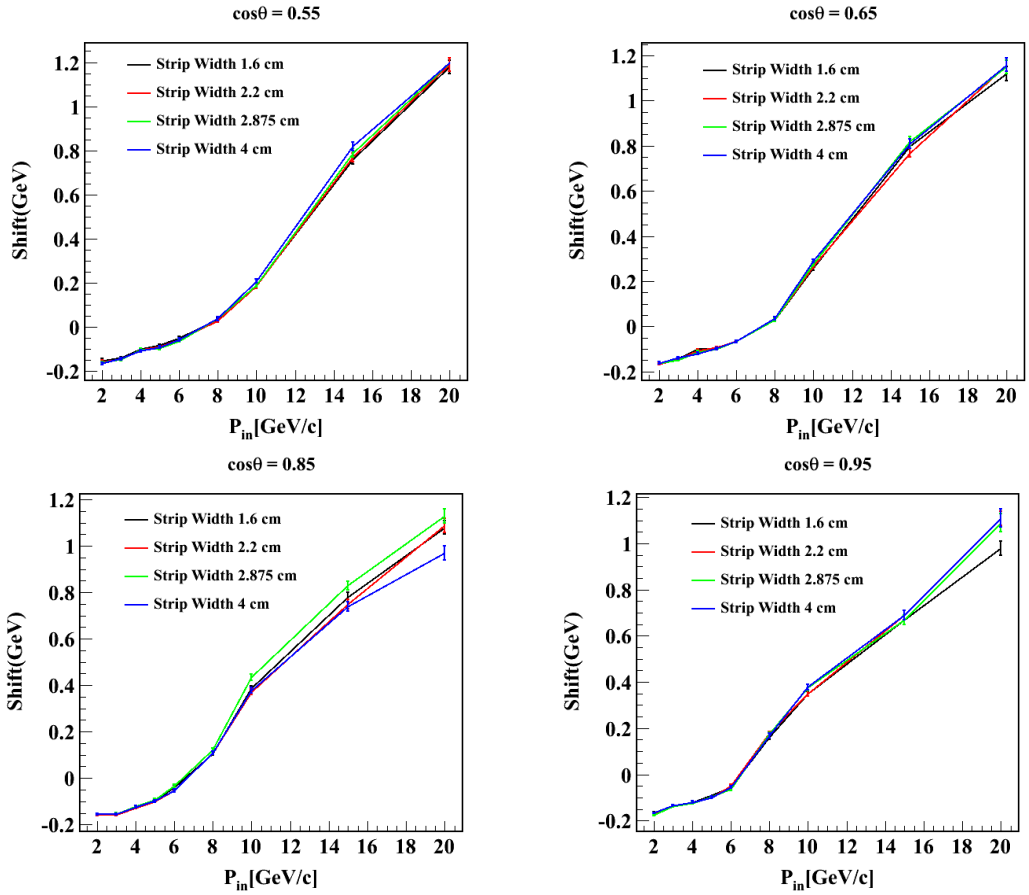

Figure 7.8: Mean shift for different cos θ bins and for the 4 strip widths.

$$\delta Shift = \delta P_{rec} \tag{7.6}$$

7.4.5 Zenith angle resolution

In presence of magnetic field, the direction of muon is estimated from the tangent to the track at the vertex. This is the width obtained by fitting the reconstructed zenith angle distribution with Gaussian probability distribution functions. The θ resolution is shown as a function of input momentum for different zenith angles in Fig. 7.9. The corresponding error is obtained in a similar way as obtained for error in momentum resolution ($\frac{\delta\sigma_{cos\ \theta_{rec}}}{cos\ \theta_{in}}$). The ratio plot is shown in Fig. 7.10.

The angle between the generated muon and reconstructed muon has been plot-

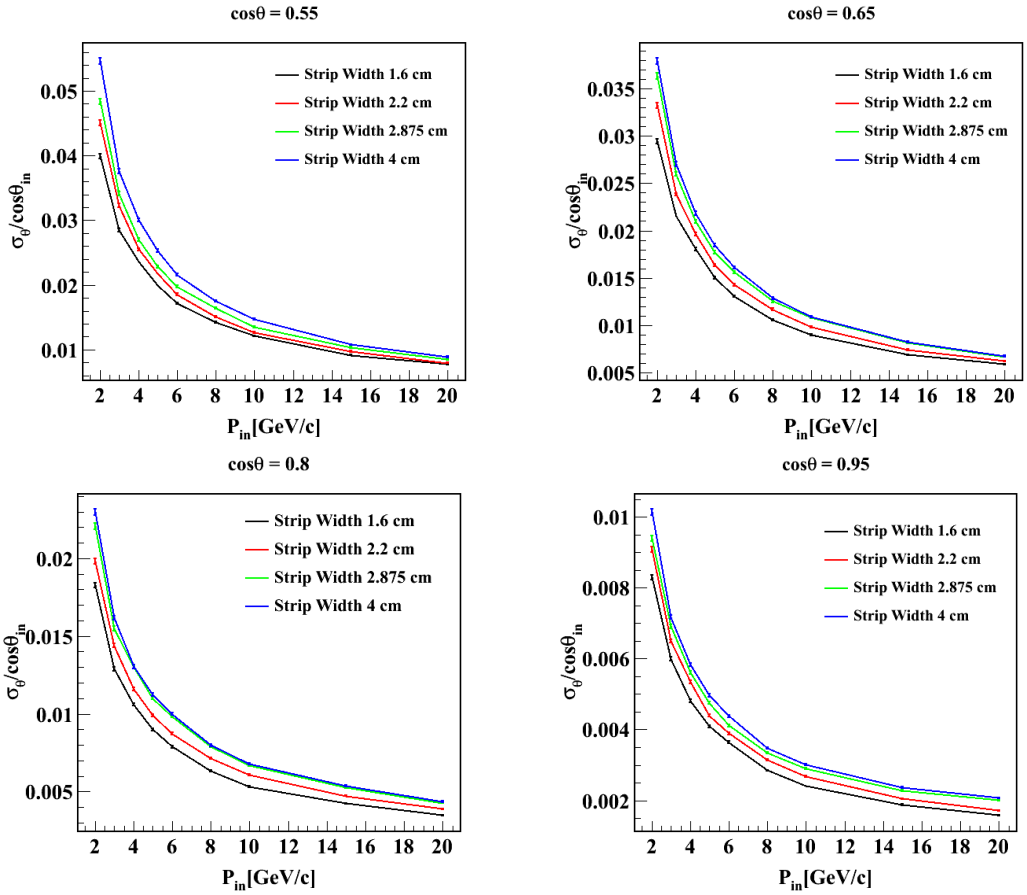

Figure 7.9: cos θ resolution for different cos θ bins and for the 4 strip widths.

ted in Fig. 7.11. It is not only θ but the combination of θ and ϕ.

$$cos\ \theta = sin\ \theta_{in} sin\ \theta_{rec} cos\ (\phi_{in} - \phi_{rec}) + cos\ \theta_{in} cos\ \theta_{rec} \tag{7.7}$$

7.5 Pion energy resolution

As a hadron interaction leads to a shower its energy can be determined indirectly, through the number of hits in the RPCs. The hits which are rejected as not being a part of the muon track are calibrated to the total energy of the hadron. The Vavilov [131] distribution function has been used for fitting.

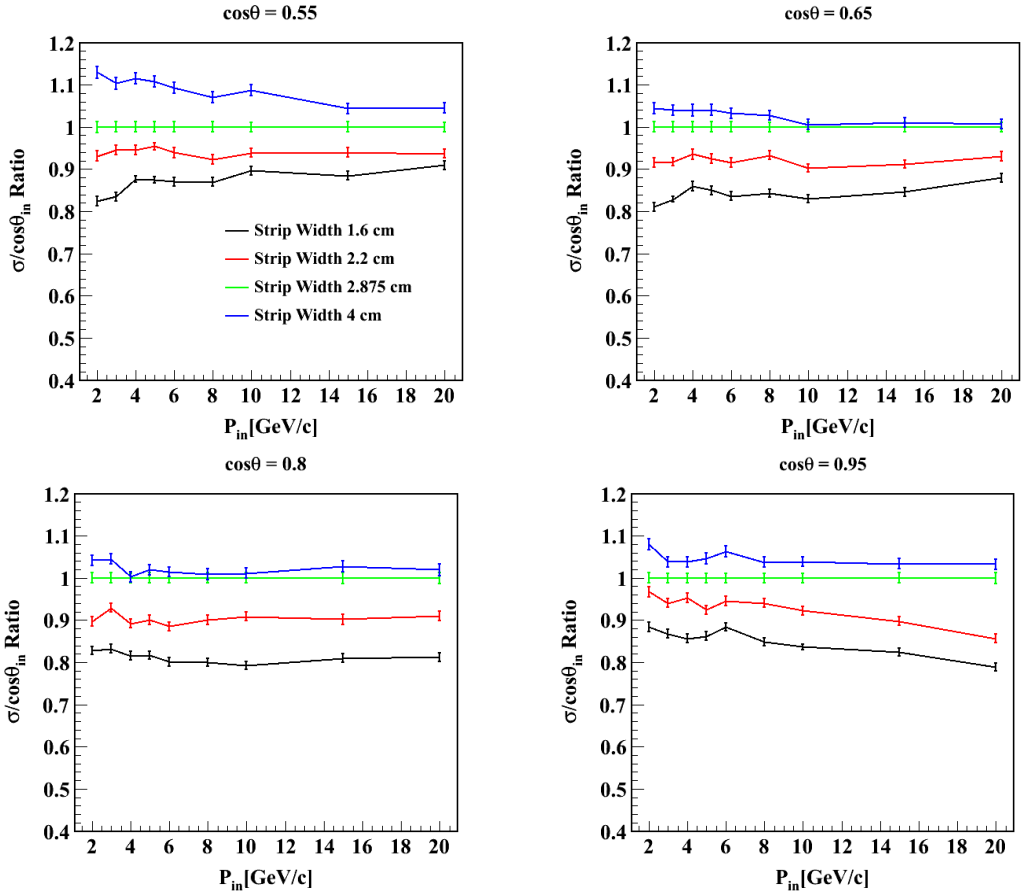

Figure 7.10: cos θ resolution ratio for different cos θ bins and for the 4 strip widths.

It is the ratio of sigma (σ) of fitted distribution to the mean of the distribution. The plots are shown in Fig. 7.12,7.13.

7.6 Conclusion

In principle decreasing the strip width should result in an improvement in the resolution for a fixed iron plate thickness. But due to the straggling in moderately thick absorbers the improvement is very small for strip widths between 1.6 cm and 4 cm. However the angle resolution improves suggest removal for the lower strip width. Hence for an iron plate thickness of 5.6 cm decreasing the strip width does not cause a significant improvement in momentum response.

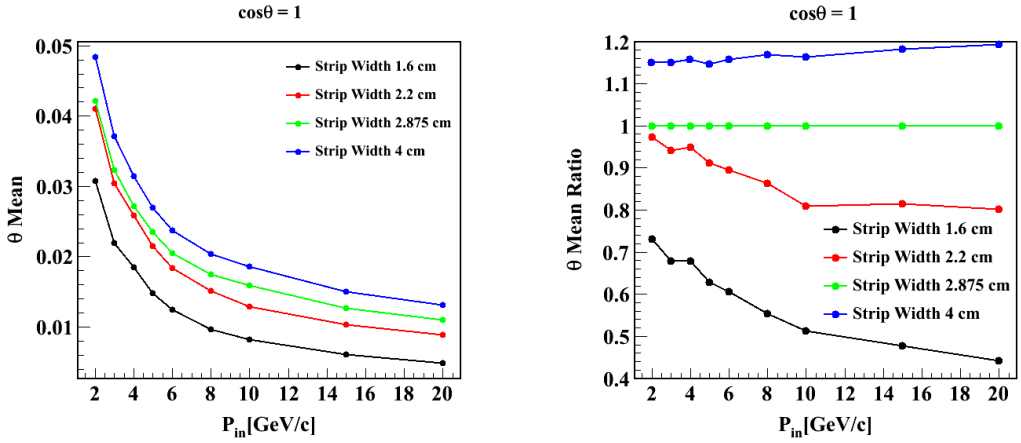

Figure 7.11: (a) Mean of θ distribution for cos $\theta = 1$, (b) Ratio plot for the 4 strip width.

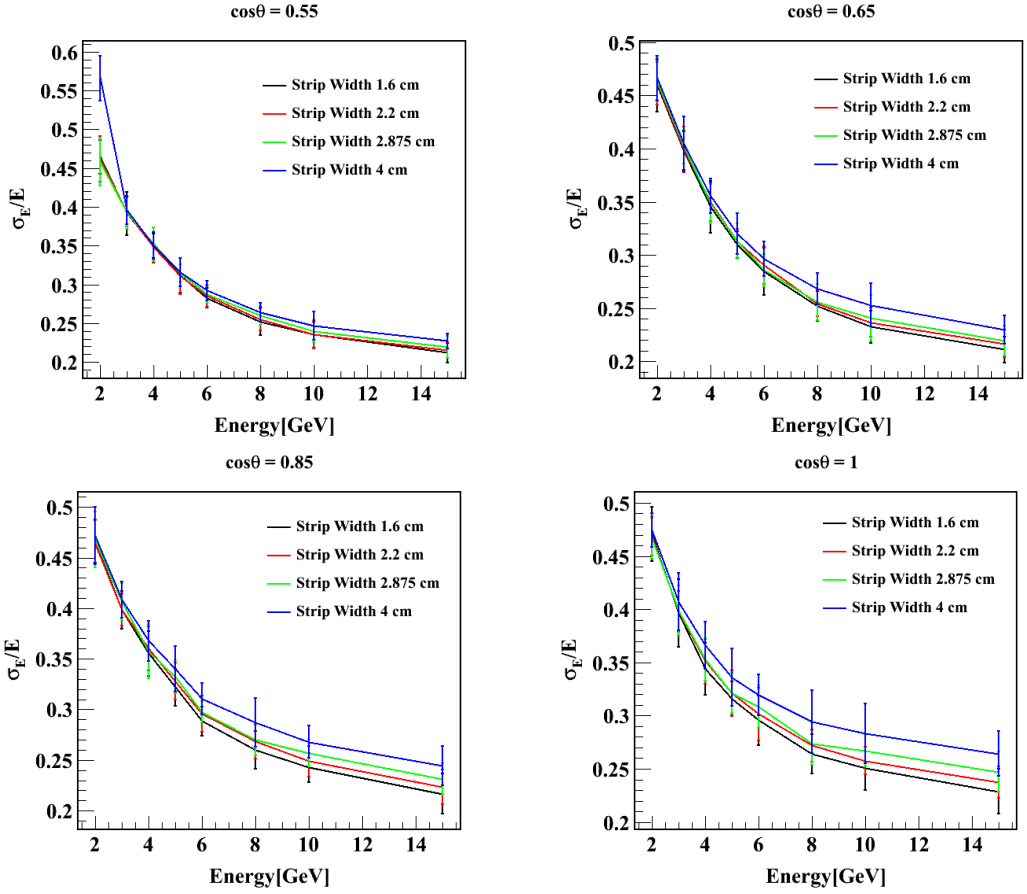

Figure 7.12: Pion energy resolution for different cos θ bins and for the 4 strip widths.

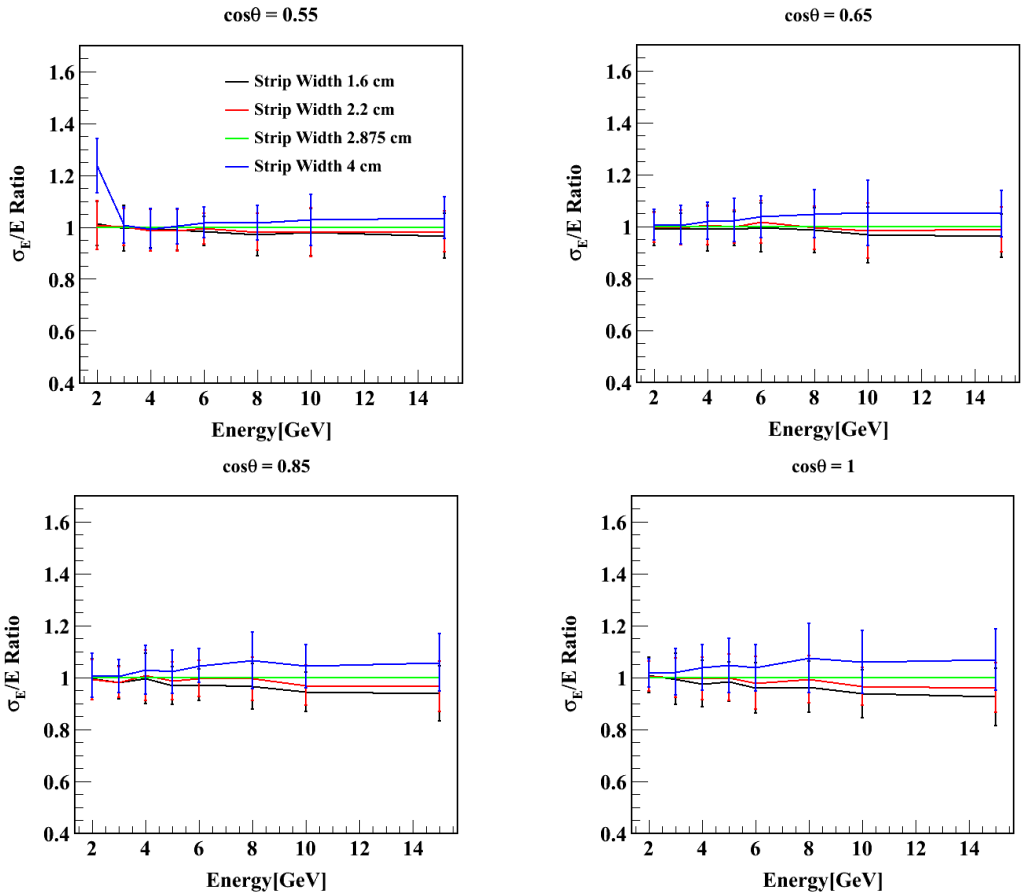

Figure 7.13: Pion energy resolution ratio for different cos θ bins and for the 4 strip widths.

8

Summary and outlook

The Iron CALorimeter (ICAL) detector at the India-based Neutrino Observatory (INO) is mainly designed for the determination of the mass hierarchy in neutrino sector and the precise measurements of neutrino oscillation parameters. Its large size and the characteristics of the active detector elements allow an exploration of physics beyond the Standard Model.

The thesis presents the first simulation study of some of the new physics capabilities of the ICAL detector. The study includes the response of ICAL to sub relativistic magnetic monopoles and muons produced from the decay of dark matter particles. In addition to this, the thesis also addresses the response of muons and hadrons as the main products of $\nu_\mu(\bar{\nu}_\mu)$ interactions in the detector and the data analysis of 1 m $\times$ 1 m twelve layers of RPC detectors at TIFR.

The active and passive elements of ICAL detector along with the required averaged magnetic field of 1.3 T are defined in GEANT4 simulation tool-kit. In order to detect all the decay products of the dark matter particles and to increase the overall fiducial volume some additional detectors are also defined in the detector geometry. Similarly to do simulation at the underground laboratory i.e. under rock cover, rock of mass density 2.89 g/cm^3 and overall height of $\sim$1 km all around is also defined in the GEANT4 framework above the ICAL cavern (housing ICAL and additional detectors). The simulation has included the possibility of particle propagation through the rock, where necessary, before entering to the detector.

A recent re-interpretation of Kolar events recorded by experiments at Kolar Gold Fields opened up a new possibility on the physics of non-luminous matter or dark matter. So the upcoming experiments at INO could give an opportunity for

the observation of such type of events and whether they arise from the decay of cold dark matter, if they are not found a bound on their lifetime could be placed. As the ICAL detector is best suited for measuring muons and reconstructing their momenta with a precision of $10 - 20\%$, dark matter decay to $\mu^+\mu^-$ channel is the one that we have used in the sensitivity work. By considering a local dark matter density of 0.39 GeV/cm^3 simulations were performed varying the mass of the dark matter particle, and hence their number density, between 1 GeV/c^2 and 50 GeV/c^2. Additional detectors were added in the ICAL cavern for increasing the efficiency of detecting the decay particles. Simulations of the augmented ICAL detector in the large cavern volume ($\sim 10^{11}$ cm^3) show that it is sensitive to DM particle decays for lifetimes of upto $\sim$2 Gyear (0.5 Gyear) for dark matter mass of 2 GeV/c^2 (20 GeV/c^2) and a 1 year running period. The enlarged volume of ICAL detector increased the expected number of Kolar events for the same period by two times than at KGF for a dark matter life time of 2 Gyear.

The reconstruction efficiency can be increased further by moderately improving the detector configuration. For the simulation a single layer of plastic scintillator detector for each plane has been used. Instead of one layer at least two layers with a minimum distance of 50 cm can be used to estimate the direction of the particle and to ascertain, whether it is generated inside the cavern or coming from outside. Since the cavern volume at ICAL-INO is $\sim$10 times that at KGF, even assuming similar detector efficiencies, the "anomalous" event rate is expected to be an order of magnitude higher. Scaling the number at KGF ($\sim$8 in 25 years) we get an expected number of $\sim$16 in 5 years.

The ICAL detector can detect sub-relativistic magnetic monopoles of mass ranging from 10^7 GeV to 10^{17} GeV with an efficiency of 90% by time of flight method and an accuracy of $5 - 10\%$ in the reconstruction of its speed β $(= v/c)$. The non observation of the MM by the ICAL can set an upper bound on the flux $\sim 1.6 \times 10^{-16}$ (cm^2 sr s)$^{-1}$ for 500 kton-years of exposure. The sensitivity is increased by factor of two by using the additional detectors proposed for the detection of dark matter particles. Due to a rock cover of $\sim$1 km, ICAL cannot put a useful limit for low mass monopoles ($M_{MM} < 10^7$ GeV) as these would be absorbed by the rock before reaching the detector.

The RPC detector give the X, Y and Z co-ordinates and the time, with respect to a reference, of a hit registered in the detector. The time information will helping

fix the upward or downward direction of the detected particle. So the directional ambiguity will be minimal the better the detector time resolution. The position dependent time resolution of RPC detectors have been studied using the cosmic ray muons collected by a stack of 1 m × 1 m RPCs at TIFR. The observed study shows a propagation length independent distribution. This study can also be carried for the 2 m × 2 m RPC, which will be used in the main ICAL module.

The correlated noise in the TIFR RPC stack due to the present DAQ electronics including the triggered logic has been examined. This noise may affect the energy and direction estimation of hadrons, low energy ν_μ CC, ν_e CC and NC events, as their characteristics are calibrated from only the hit information. The simulation study can be carried further by understanding the observed noise pattern and reducing it so as to enable an accurate measurement of the energy and direction.

The energy and direction of ν_μ and $\bar{\nu}_\mu$ is obtained by combining the momenta of muon and hadron. The resolution will increase with a more precise measurement of the hit point in the detector. So in principle improving the position resolution of the sensitive detector may help. So as a part of optimisation of ICAL detector parameters, the simulation studies has been carried for pitch width of dimensions 1.6 cm to 4 cm of RPC detector. The study has been carried out to see the influence of strip width on the momentum and direction resolution of muons and energy resolution of hadrons. Decreasing the strip width does not result in the improvement in the momentum resolution, due to the use of comparatively thicker ($\sim$5.6 cm) iron plates. But there is some improvement in the direction resolution. The study can be carried further by varying the iron plate thickness for the defined dimensions of strip width.

In conclusion, while ICAL′s main goal remains addressing the mass hierarchy of neutrinos by measuring atmospheric muon neutrinos it can also make competitive searches for dark matter particle decay and magnetic monopoles.

References

[1] S.L. Glashow, Nucl. Phys. **22**, 579 (1961).

[2] S. Weinberg, Phys. Rev. Lett. **19**, 1264 (1967);
S. Weinberg, Phys. Rev. Lett. **27**, 1688 (1971).

[3] F.J. Hasert et al., Nucl. Phys. **B73**, 1 (1974).

[4] P. Higgs, Phys. Rev. Lett. **13**, 508 (1964).

[5] F. Englert and R. Brout, Phys. Rev. Lett. **13**, 321 (1964).

[6] V. Khachatryan et al., Eur. Phys. J. **C75**, 212 (2015).

[7] G. Aad et al., Phys. Rev. **D90**, 052004 (2014).

[8] O. Dahl et al. (Particle Data Group), Chine. Phys. **C38**, 9 (2014).

[9] D.I. Kazakov, arXiv:hep-ph/0012288v2 (2001).

[10] E. Fermi, Z. Phys. **88**, 161 (1934).

[11] F. Reines and Jr.C.L. Cowan, Phys. Rev. **113**, 273 (1958).

[12] J.K. Bienlein et al., Phys. Lett. **13**, 80 (1964).

[13] M. Goldhaber et al., Phys. Rev. **109**, 1015 (1958).

[14] K. Hagiwara K et al., Phys. Rev. **D66**, 010001 (2002).

[15] R. Davis, Phys. Rev. Lett. **12**, 303 (1964).

[16] C.V. Achar et al., Phys. Lett. **18**, 196 (1965).

[17] F. Reines et al., Phys. Rev. Lett. **15**, 429 (1965).

[18] K. Hirata et al., Phys. Rev. Lett. **58**, 1490 (1965).

[19] T. Araki et al., Nature **436**, 499 (2005).

[20] N.K. Mondal, Pramana **79**, 1003 (2012).

[21] T. Thakore et al., JHEP. **1305**, 058 (2013).

[22] M.S. Athar et al., arXiv:1505.07380 (2015).

[23] A. Ghosh et al., JHEP. **1304**, 009 (2013).

[24] V. Singh et al., AIP Conf. Proc. **1405**, 334 (2011).

[25] V. Singh et al., Pramana **81**, 719 (2013).

[26] N. Dash et al., accepted for publication in Pramana - journal of physics; arXiv:1410.5182v1 (2014).

[27] N. Dash et al., Astropart. Phys. **70**, 33 (2015).

[28] C. Arpesella, Nucl. Instr. Meth. **A277**, 1 (1989).

[29] M. Ambrosio et al., Nucl. Instr. Meth. **A456**, 67 (2000).

[30] M. Sajjad Athar et al., Phys. Lett. **B718**, 1375 (2013).

[31] J.A. Formaggio et al., Rev. Mod. Phys. **84**, 1307 (2012).

[32] R. Gandhi and S. Panda, JCAP **0607**, 011 (2006).

[33] S. Panda and S. Sinegovsky, Int. J. Mod. Phys. **A23**, 2933 (2008).

[34] A. Chatterjee et al., JHEP. **1406**, 045 (2014).

[35] A. Chatterjee et al., arXiv:1409.8472 (2015).

[36] S.P. Behera et al., IEEE **51**, 2 (2015).

[37] A. Chatterjee et al., JINST **9**, P07001 (2014).

[38] R. Kanishka et al., JINST **10**, P03011 (2015).

[39] M.M. Devi et al., JINST **8**, P11003 (2013).

[40] L.S. Mohan et al., JINST **9**, T09003 (2014).

[41] A. Ajmi and S. Uma Sankar, JINST **10**, P04006 (2015).

[42] A. Ajmi and S. Uma Sankar, arXiv: 1505.07295 (2015).

[43] S. Pal et al., JCAP **07**, 033 (2012).

[44] V.M. Datar et al., Nucl. Instr. Meth. **A602**, 744 (2009).

[45] A. Joshi et al., Nucl. Instr. Meth. **A602**, 809 (2009).

[46] S.D. Kalmani et al., Nucl. Instr. Meth. **A602**, 845 (2009).

[47] M. Bhuyan et al., Nucl. Instr. Meth. **A661**, S64 (2012).

[48] M. Bhuyan et al., Nucl. Instr. Meth. **A661**, S73 (2012).

[49] M. Ricci (for the PAMELA Collaboration), J. Phys.: Conf. Ser. **375**, 052011 (2012).

[50] M. Aguilar et al., Phys. Rev. Lett. **110**, 141102 (2013).

[51] R. Bernabei et al., Eur. Phys. J. **C67**, 39 (2010).

[52] C.E. Aalseth et al., Phys. Rev. **D88**, 012002 (2013).

[53] G. Angloher et al., Astropart. Phys. **31**, 270 (2009).

[54] R. Agnese et al., Phys. Rev. Lett. **111**, 251301 (2013).

[55] M.R. Krishnaswamy et al., Pramana **5**, 59 (1975).

[56] M.R. Krishnaswamy et al., Phys. Lett. **B57**, 105(1975).

[57] M.R. Krishnaswamy et al., Proc. XXIII Int. Conf. on High Energy Physics, Berkeley (ed.) S Loken (World Scientific, 1986).

[58] M.V.N. Murthy and G. Rajasekaran, Pramana **82**, 609 (2014).

[59] H. Faissner et al., Phys. Lett. **B60**, 401 (1976).

[60] A.C. Benvenuti et al., Phys. Rev. Lett. **35**, 1486 (1975).

[61] V.S. Narasimham, Proc. Indian National Science Academy A **70**, 11 (2004).

[62] G. Rajasekaran and K.V.L. Sarma, Pramana **5**, 78 (1975).

[63] K.V.L. Sarma and L. Wolfenstein, Phys. Lett. **B61**, 77 (1976).

[64] A.S. Joshipura et al., Pramana **33**, 639 (1989).

[65] F. Zwicky, Helv. Phys. Acta. **6**, 110 (1933).

[66] S. Smith, Astrophys. J. **83**, 23 (1936).

[67] V.C. Rubin et al., Astrophys. J. **159**, 379 (1970).

[68] D. Clowe et al., Astrophys. J. **648**, L109 (2006).

[69] P.A.R. Ade et al., Astron. Astrophys. **571**, A1 (2014).

[70] R.D. Peccei and H. Quinn, Phys. Rev. Lett. **38**, 1440 (1977);
R.D. Peccei and H. Quinn, Phys. Rev. **D16**, 1791 (1977).

[71] H. Cheng et al., Phys. Rev. Lett. **89**, 211301 (2002).

[72] P. Sikivie, Phys. Rev. Lett. **51**, 1415 (1983).

[73] P. Sikivie, Phys. Rev. **D32**, 2988 (1985).

[74] C. Hagmann et al., Nucl. Instr. Meth. **A444**, 569 (1999).

[75] C. Hagmann et al., Phys. Rev. Lett. **80**, 2043 (1998).

[76] S.J. Asztalos et al., Phys. Rev. Lett. **104**, 041301 (2010).

[77] P.F. Smith and J.D. Lewin, Phys. Reports **187**, 203 (1990).

[78] P.F. Smith, Nuovo. Cimento. A **83**, 263 (1984).

[79] G. Angloher et al., Eur. Phys. J. **C72**, 197 (2012).

[80] R. Bernabei et al., Eur. Phys. J. **C67**, 39 (2010).

[81] D. Licoln, Phys. Tech. **51**, 134 (2013).

[82] M. Aguilar et al., Phys. Rev. Lett. **110**, 141102 (2013).

[83] O. Adriani et al., Phys. Rev. Lett. **111**, 081102 (2013).

[84] O. Adriani et al., Phys. Rev. Lett. **105**, 121101 (2010).

[85] A.A. Abdo et al., Phys. Rev. Lett. **104**, 101101 (2010).

[86] G. Kane and S. Watson, Mod. Phys. Lett. **A23**, 2103 (2008).

[87] O. Adriani et al., Astropart. Phys. **34**, 1 (2010).

[88] http://geant4.web.cern.ch/geant4/

[89] K. Bhattacharya et al., CPC **185**, 3259 (2014).

[90] L. Covi et al., JCAP **1004**, 017 (2010).

[91] R. Abbasi et al., Phys. Rev. **D84**, 022004 (2011).

[92] P.A.M. Dirac, Proc. Roy. Soc. A **133**, 60 (1931);
P.A.M. Dirac, Phys. Rev. **74**, 817 (1948).

[93] M.N. Saha, Ind. J. Phys. **10**, 145 (1936)

[94] L.J. Schwinger, Phys. Rev. **D12**, 3105 (1975).

[95] K.R. Gienes et al., Phys. Rev. **B436**, 55 (1998).

[96] V.A. Rubakov, Nucl. Phys. **B203**, 311 (1982).

[97] T. Banks et al., Phys. Lett. **B212**, 45 (1988).

[98] G. Giacomelli and L. Patrizi, arXiv:hep-ex/0302011.

[99] G. 't Hooft, Nucl. Phys. **B79**, 276 (1974).

[100] A.M. Polyakov, JETP Lett. **20**, 194 (1974).

[101] E.N. Parker, Astrophys. J. **160**, 383 (1970).

[102] M.S. Turner et al., Phys. Rev. **D26**, 1296 (1982).

[103] J. Preskill, Ann. Rev. Nucl. Part. Sci. **34**, 461 (1984).

[104] B. Cabrera, Phys. Rev. Lett. **48**, 1378 (1982).

[105] S. Bermon et al., Phys. Rev. Lett. **64**, 839 (1990).

[106] S.P. Ahlen, Phys. Rev. **D17**, 229 (1978).

[107] Y. Kazama et al., Phys. Rev. **D15**, 2287 (1977).

[108] H.H. Andersen and J.F. Ziegler, Hydrogen Stopping Powers and Ranges in All Elements (Pergamon, New York) (1977).

[109] S.P. Ahlen and K. Kinoshita, Phys. Rev. **D26**, 2347 (1982).

[110] J. Derkaoui et al., Astropart. Phys. **10**, 339 (1999).

[111] S.P. Ahlen and G. Tarle, Phys. Rev. **D27**, 688 (1983).

[112] G.F. Drell et al., Nucl. Phys. **B209**, 45 (1982).

[113] M. Ambrosio et al., Eur. Phys. J. **C25**, 511 (2002).

[114] S. Balestra et al., Eur. Phys. J. **C55**, 57 (2008).

[115] J.L. Thron et al., Phys. Rev. **D46**, 4846 (1992).

[116] G. Aad et al., Phys. Rev. Lett. **109**, 261803 (2012).

[117] A. Abulencia et al., Phys. Rev. Lett. **96**, 201801 (2006).

[118] G.R. Kalbfleisch et al., Phys. Rev. Lett. **85**, 5292 (2000).

[119] C.P. Dokos and T.N. Tomaras, Phys. Rev. **D21**, 2940 (1980).

[120] C.G. Callan, Phys. Rev. **D26**, 2058 (1982).

[121] R. Abbasi et al., Phys. Rev. **D87**, 022001 (2013).

[122] M.G. Aartsen et al., arXiv:1402.3460v2 (2014).

[123] S. Adrian-Martinez et al., Astropart. Phys. **35**, 634 (2012).

[124] V. Aynutdinov et al., Astropart. Phys. **29**, 366 (2008).

[125] T. Kajita et al., J. Phys. Soc. Jap. **54**, 4065 (1985).

[126] J. Derkaoui et al., Astropart. Phys. **9**, 173 (1998).

[127] J. Incandela et al., Phys. Rev. Lett. **53**, 2067 (1984).

[128] M.E. Huber et al., Phys. Rev. Lett. **64**, 835 (1990).

[129] B. Satyanarayana, "Design and Characterisation Studies of Resistive Plate Chambers", Ph.D. Thesis (IIT Bombay), 2009.

[130] O. Amoda, "Design Of Readout System for an Resistive Plate Chamber", Report on work done under Summer Internships in Science and Technology (SIST) program at FNAL (August 6, 2002).

[131] W.R. Leo, "Techniques for Nuclear and Particle Physics Experiments - A How-to Approach", 2nd Edition, Springer Verlag (Berlin Heidelberg 1994).